Qualification of the Two-Dimensional Transport Code PARAGON2

Page Intentionally Left Blank

WCAP-18443-NP
Revision 0

Qualification of the Two-Dimensional Transport Code PARAGON2

Mohamed Ouisloumen*
PWR Core Methods

Michael E. Gavalek*
Core Engineering & Software Development

Ho Q. Lam*
PWR Core Methods

October 2019

Verifier: Arielle L. Konig for Michael J. Hone*
New Reactor Technology

Jeffery A. Brown*
Core Engineering & Software Development

Approved: Zachary B. McDaniel*
PWR Core Methods, Manager

*Electronically approved records are authenticated in the electronic document management system.

Page Intentionally Left Blank

Acknowledgement

Page Left Intentionally Blank

TABLE OF CONTENTS

LIST OF TABLES

$$\begin{array}{c} \\ \\ \\ \end{array}$$ a,c

LIST OF FIGURES

[   ]^{a,c}

a,c

a,c

a,c

a,c

LIST OF ACRONYMS, SYMBOLS, AND TERMS

Acronym/Term	Description
3D, 2D, 1D	Three-, Two-, One-dimensional
ANC	Advanced Nodal Code
ARI	All Rods In
ARO	All Rods Out
B&W	Babcock & Wilcox
BOC, MOC, EOC	Beginning, Middle, and End of Cycle
CE	Combustion Engineering
CEA	Control Element Assembly
CI	Confidence Interval
CRAM	Chebyshev Rational Approximation Method
CRIEPI	Central Research Institute of Electric Power Industry (Japan)
CZP	Cold Zero Power
DCR	Doppler Coefficients of Reactivity
DOE	Department of Energy
DTC, DPC	Doppler Temperature-, Power- Coefficient
ENDF/B-VII	Evaluated Nuclear Data File (B-VII database version)
eV, keV, MeV	Electron Volt, kilo-, mega-
HFP	Hot Full Power
HZP	Hot Zero Power
IFBA	Integral Fuel Burnable Absorber
ITC	Isothermal Temperature Coefficient
JEFF	Joint Evaluated Fission and Fusion Nuclear Data Library
JENDL	Japanese Evaluated Nuclear Data Library
KWU	Kraftwerk Union
LWR	Light Water Reactor
MCNP	Monte Carlo N Particle Transport Code
MDC	Moderator Density Coefficient
MOX	Mixed Oxide Fuel (fuel with mixed UO_2/PuO_2)
MTC	Moderator Temperature Coefficient
MTU, tU	Metric-, Tonne Uranium
MW	Megawatts

a,c

a,c

Acronym/Term	Description
NCA	Toshiba Nuclear Critical Assembly
NRC	Nuclear Regulatory Commission
PIE	Post-Irradiation Examination
PWR	Pressurized Water Reactor
RCCA	Rod Cluster Control Assembly
RCF	Reactor Critical Facility
RI	Resonance Integral
RMS	Root-Mean Square
RPI	Rensselaer Polytechnic Institute
	[ ]^{a,c}
RSM	Resonance Scattering Model
SFCOMPO	Spent Fuel Isoptopic Composition
SPERT	Special Power Excursion Reactor Test
TMI	Three Mile Island
TPBAR	Tritium Producing Burnable Absorber Rod
TRX	Thermal Reactor Cross-sections Evaluation Experiments
UFEML	Ultra-Fine Energy Mesh Library
USAEC	United States Atomic Energy Commission
VENUS (SCK-CEN)	Vulcain Experimental Nuclear Study (CEN-SCK, Mol, Belguim)
W	Westinghouse Electric Company LLC.
WABA	Wet Annular Burnable Absorber
WSR	Worst Stuck Rod, Highest reactivity control rod cluster
	[ ]^{a,c}
PHOENIX-P, PARAGON, PARAGON2	two-dimensional multi-group neutron transport code

1 INTRODUCTION

The purpose of this report is to provide documentation of the qualification of PARAGON2, a new Westinghouse neutron transport lattice code. It is also requested that the NRC provide generic approval of PARAGON2 for use with Westinghouse's nuclear design code system or as a standalone code. The code will be used primarily to calculate nuclear input data for three-dimensional core simulators. Based on the qualification of PARAGON2 as documented herein, PARAGON2 can be used as a standalone or as a direct replacement for all the previously licensed Westinghouse PWR lattice codes, such as PHOENIX-P and PARAGON. Thus, other topical reports that reference the Westinghouse nuclear design code system will remain applicable with PARAGON2.

A major nuclear design code system in use at Westinghouse since 1988 consists of two primary codes, PHOENIX-P and ANC. PHOENIX-P is the neutron transport lattice code currently used to provide nuclear input data for ANC. The qualification and license approval of the use of PHOENIX-P for PWR core design calculations is provided in Ref. [31]. In 2004, the PARAGON neutron transport lattice code was introduced as a replacement for PHOENIX-P to provide nuclear input lattice data for ANC. The qualification and license approval of the use of PARAGON for PWR core design calculations is provided in Ref. [41].

PARAGON2 is a significantly improved version of PARAGON intended as a replacement for PHOENIX-P and PARAGON, and its primary use will be to provide the same types of input data that PARAGON generates for use in three-dimensional core simulator codes. This includes macroscopic cross-sections, microscopic cross-sections for feedback adjustments to the macroscopic cross-sections, pin factors for pin power reconstruction calculations, and discontinuity factors for a nodal method solution.

PARAGON2 is based on collision probability – interface current cell coupling methods. PARAGON2 provides the same flexibility in modeling that was available in PARAGON including exact cell geometry representation, multiple rings and regions within the fuel pin and the moderator cell geometry, and variable cell pitch. The solution method permits flexibility in choosing the quality of the calculation through both increasing the number of regions modeled within the cell and the number of angular current directions tracked at the cell interfaces. Section 2 will provide further details on PARAGON2 theory and features.

The qualification of a nuclear design code is a large undertaking since it must address the qualification of the methodology used in the code, the implementation of that methodology, and its application within a nuclear design system. For this reason, Westinghouse has historically used a systematic qualification process, which starts with the qualification of the basic methodology used in the code and proceeds through logical steps to the qualification of the code as used with the entire system. This process was used when qualifying PARAGON in Ref. [41]. This same process is followed for the qualification of PARAGON2 in this report.

Consistent with the qualification process described above, the qualification of PARAGON2 will consist of three parts: 1) comparisons to critical experiments and isotopic measurements, 2) comparisons of assembly calculations with Monte Carlo method calculations (MCNP and SERPENT2), and 3) comparisons against measured plant data. The first two parts will qualify the methodology used in PARAGON2 and its implementation. The third part will qualify the use of PARAGON2 data for core design and nuclear safety applications. Where appropriate, comparisons will also be made to PARAGON results.

The current PARAGON2 cross-section library is a 6064-group library. The PARAGON2 qualification library has been improved through the addition of more explicit fission products and fission product chains.

This report is organized in the Sections as described below.

Section 2 presents an overview of the PARAGON2 theory and its implementation. The nuclear data library used for this qualification is also described in this section.

Section 3 presents the results of PARAGON2 calculations for many standard critical experiments. These include integral experiments as well as MOX and Uranium oxide critical experiments. Section 3 also presents isotopic comparisons between PARAGON2 and measurement for several PIE experiments, such as the Yankee and Saxton isotopic measurements and the PIE data from several plants obtained from the spent fuel benchmarks database SFCOMPO 2.0.

Section 4 presents reactivity and power distribution comparisons between PARAGON2 and Monte Carlo (SERPENT2) calculations for single assembly problems. Various assembly designs similar to those currently in use in PWR cores are included in these SERPENT2/PARAGON2 comparisons. [

]a,c

Section 5 presents the results of using PARAGON2 input data with a three-dimensional core simulator model (in this case ANC) and compares the calculations to actual plant measurements. The parameters compared are boron letdown curves, BOC HZP critical boron, BOC ITC, and BOC rod worths. Comparisons of the results of using PARAGON2 input data with a three-dimensional core simulator model (ANC) against measured core power distributions are also shown for several cycles. Section 5 also presents comparisons of PARAGON2/ANC model results against those of PARAGON/ANC for core calculations for which there are no plant measurements (e.g. shutdown margin, ejected rod, etc.).

Section 6 presents overview of all the results and provides conclusions on the applicability of PARAGON2 as a standalone transport code and as a nuclear data source for a core simulator in a complete nuclear design code system for core design, safety and operational calculations.

Section 7 addresses the licensing application of PARAGON2 for use as a standalone transport code and as a nuclear data source for core simulators.

2   PARAGON2 METHODOLOGY

2.1   INTRODUCTION

PARAGON2 is a two-dimensional multi-group neutron (and gamma) transport code. It is an improvement over the Westinghouse licensed lattice codes PHOENIX-P (Ref. [31]) and PARAGON (Ref. [41]). The difference between PARAGON and PHOENIX-P is described in Ref. [41]. The main difference between PARAGON2 and PARAGON resides in the use of an Ultra-Fine Energy Mesh cross-section Library (UFEML) and the Resonance Scattering Model (RSM) in solving the transport equation. Because of the ability to accurately predict the cross-section depressions about the resonances using the energy fine mesh adopted in UFEML, the resonance self-shielding calculation, traditionally needed in lattice codes, is eliminated in PARAGON2. [

]^{a,c}. The UFEML and the RSM will be described in this section followed by the theory of the solvers of each PARAGON2 module.

2.2   PARAGON2 CROSS-SECTION LIBRARY

2.2.1   Ultra-Fine Energy Mesh Cross-section Library

The group structure that PARAGON2 uses for its cross-sections library is based on 6064 energy grids for the neutron transport calculations, covering the energy range from 20 MeV to 1.0E-05 eV. For the photon transport calculations, it employs a 97 energy group structure covering the energy range of 50 MeV to 1 keV. The data in this library is based on the latest basic evaluated nuclear data files released by Brookhaven National Laboratory (ENDF/B-VII, Ref. [2]). The neutron energy group boundaries have been studied and carefully selected to best describe the epithermal and thermal energy resonances and the cross-section behaviors of major isotopes that will be needed in the reactor core simulations. This library was benchmarked against an even finer group structure (in addition to the continuous energy Monte Carlo solutions) and was demonstrated to provide an accurate depiction [37].

A modified version of the computer code NJOY [22] was used to generate the new PARAGON2 cross-section library that will be designated here as the Ultra-Fine Energy Mesh cross-sections Library (UFEML). In this new version of NJOY the anisotropic resonance scattering model described in Ref. [45] was implemented.

The Ultra-Fine Energy Mesh Library (UFEML) is entirely based on ENDF/B-VII, except for a few isotopes that use the JEFF data. These few isotopes from JEFF were adopted because they were giving [

]^{a,c}. Practically, UFEML will have the neutron data for all the isotopes present in these evaluations ENDF/B-VII, JEFF or others. The cross-sections in this library are tabulated only as a function of temperature [

]^{a,c}. Independently, [

]^{a,c}. All the isotopes in UFEML have the Resonance Scattering Model (RSM) accounted for in the scattering matrices following the method described in Ref. [45], except for hydrogen in water and carbon in graphite for which the S(α,β) scattering law is used. The photon production cross-sections are provided in the 97 energy groups and for all the nuclides for which gamma production data is available in ENDF/B-VII or other equivalent nuclear data libraries. It is important to mention that the photon generation from neutron nuclear (or atomic) reactions uses the same 6064 neutron

energy group structure. Since the majority of the gamma data is not sensitive to the temperature (for the expected applications of PARAGON2), the tabulation is only done for the cold temperature (300 K). Internally, however, the code accounts for the temperature dependence in the gamma production via (n, γ) reactions. For a particular isotopic temperature, a linear interpolation in $\sqrt{T}$ is then used by PARAGON2 to extract the desired cross-section data from the UFEML table.

Each isotope in UFEML has two scattering matrix moments P_0 and P_1 and these matrices are sparse by nature. The limitation to these two scattering moments can be addressed with the implementation of a new flux solver that can use higher order anisotropic scattering (like Method of Characteristics). The P_0 scattering matrices contain diagonal corrections for anisotopic scattering.

It is important to note that the cross-sections in UFEML are processed from the basic evaluated data files without any adjustments. [

]^{a,c}. With the old coarse energy mesh methodology, an artificial reduction of U-238 absorption was necessary for predictions closer to the plants operation data as described in Ref. [14]. These empirical adjustments are eliminated in PARAGON2. Many facts contributed to this enhancement. The most important are the fine energy mesh that adequately treats the resonance calculation phenomenon and the new resonance scattering model.

The adoption of the ultra-fine energy mesh structure permits the elimination of the resonance self-shielding calculation since this method is only needed for coarse energy mesh structure. In PARAGON2 the resonance calculation module was eliminated.

2.2.2 Resonance Scattering Model

An important component of PARAGON2 is the Resonance Scattering Model. This section is dedicated to describe briefly the theory and physics behind the implementation of the Resonance Scattering Model. The development and complete theory is presented in Ref. [45].

The scattering source term of the neutron transport equation describes how neutrons collide with the isotopes of the media (fuel assembly) and consequently provides how the energy and direction of the neutrons are affected after the collision. In this model, only the elastic scattering nuclear reactions are of interest. Traditionally, this term is referred to as the transfer scattering kernel (or double differential scattering kernel) and is expressed as a product of the scattering cross-section and the transfer probability density. The cross-sections (including scattering) used in the transport equation are usually Doppler-broadened to account for the motion of atoms in the media (crystalline structure effect) in the course of the neutron-nucleus reactions. The transfer kernel is treated differently depending on the energy range and the type of isotope. For light isotopes, such as hydrogen or graphite, the solid-state molecular structure is taken into account at the thermal energy range (practically below 4 eV) using the well-known $S(\alpha, \beta)$ scattering matrices. In the epithermal energy range, the elastic scattering reaction is treated assuming that the energy of the neutrons is sufficiently high to justify the approximation of the target atom being at rest. In this case the transfer probability density is simply proportional to $1 / E$, where E is the energy of the neutron before the collision. This simple formula is the result of the preservation of energy and momentum in the two-body kinematics theory of classical mechanics. For heavy and intermediate mass isotopes, the exact same approach is used for epithermal energies. For the thermal energy range, an isotropic Maxwellian velocity distribution is commonly used to describe the agitation of the atoms in the media as a free gas model. In this case, the transfer density is much simpler than that of the light isotopes. This way of computing the

transfer kernel was adopted in all deterministic and stochastic based transport codes currently used in the nuclear industry, with the further simplification of neglecting the effect of lattice thermal vibrations on the energy transfer probability distribution component of the scattering kernel. This latter assumption of neglecting the effect of atoms thermal vibration in the crystalline structure was proven not to be accurate in Ref. [43], especially for resonant isotopes in the epithermal energy domain. The formulation of the Doppler-broadened transfer kernel derived in Ref. [43] and henceforth dubbed as the Resonance Scattering Model (RSM) shows: 1) that the transfer probability density is far from behaving as $1 / E$, 2) that the energy dependence outcome of the neutron scattering process is strongly dependent on the presence of scattering resonances in certain isotopes, and 3) a strong effect of the medium temperature on the scattering event outcome, as expected.

The formulation of the scattering kernel in Ref. [43] was limited solely to isotropic scattering in the neutron-nucleus center-of-mass system. In this work, the theory is generalized to cover anisotropic scattering.

2.2.2.1   Anisotropic Resonance Scattering Kernel

The differential microscopic elastic scattering cross-section at a temperature T is given by (Ref. [43]):

$$\sigma_s^T(E \rightarrow E', \mu_{lab}) = \sum_{n \geq 0} \frac{2n+1}{2} \sigma_{sn}^T(E \rightarrow E') P_n(\mu_{lab}). \quad (1)$$

The usual notations and definitions are adopted here (see Ref. [43]). Hence, $P_n(\mu_{lab})$ is the nth order Legendre polynomial, μ_{lab} is the cosine of the angle between initial and final neutron velocities corresponding to incident and outgoing energies E and E' in the laboratory frame.

If the crystalline effect is neglected, the transfer scattering moments are given by

$$\sigma_{sn}^T(E \rightarrow E') = \frac{\sigma_{sn}^T(E) \mathcal{H}(E - E') \mathcal{H}(E - \alpha E')}{(1 - \alpha)E}. \quad (2)$$

Where, $\sigma_{sn}^T(E)$ is the Doppler-broadened scattering cross-section moment at temperature T and energy E, $\alpha = \left(\frac{A-1}{A+1}\right)^2$ where A is the atomic ratio, and $\mathcal{H}(x)$ is the Heaviside distribution (step function). This model will be designated as the asymptotic model.

If the atoms motions are accounted for in the neutron-nucleus scattering nuclear reaction, then the transfer scattering moments formulations are more complex and are given by

$$\sigma_{sn}^T(E \rightarrow E') = \frac{\beta^{5/2}}{4E} e^{E/kT} \int_0^\infty t \sigma_s^{tab}\left(\frac{\beta kT}{A} t^2\right) e^{-t^2/A} \psi_n(t) dt \quad (3)$$

Where $\beta = (A+1)/A$, k is the Boltzmann constant and $\sigma_s^{tab}(E)$ is the convolved scattering cross-section at $0\,K$ that is subjected to the convolution process. In the above equation, $\psi_n(t)$ is given by:

$$\psi_n(t) = \mathcal{H}(t_- - t)\mathcal{H}(t - t_+)\acute{G}_n(\varepsilon_{max} - t, t + \varepsilon_{min}) + \mathcal{H}(t - t_+)\acute{G}_n(t - \varepsilon_{min}, t + \varepsilon_{min}), \quad (4)$$

where $t_\pm = \frac{1}{2}(\varepsilon_{max} \pm \varepsilon_{min})$, $\varepsilon_{min} = \sqrt{(A+1)E_{min}/kT}$, $\varepsilon_{max} = \sqrt{(A+1)E_{max}/kT}$ with $E_{min} = \min(E, E')$ and $E_{max} = \max(E, E')$. Also, $\acute{G}_n(x_-, x_+)$ is defined here as

$$G_n(x_-, \, x_+) = \pi^{-3/2} \int_{x_-}^{x_+} e^{-x^2} \, dx \int_0^{2\pi} P_n(\mu_{lab}) f\left(\frac{\beta kT}{A} t^2, \mu_{CM}\right) d\Phi \quad (5)$$

In the above equations, the cosines of the scattering angle in the center-of-mass and laboratory frames are used. They are given, respectively, by

$$\mu_{CM} = \frac{D_- + B \cos\phi}{4x^2 t^2} \; and \; \mu_{lab} = \frac{D_+ + B \cos\phi}{4x^2 \varepsilon_{min} \varepsilon_{max}}$$

with $D_\pm = (\varepsilon_{max}^2 \pm x^2 - t^2)(\varepsilon_{min}^2 \pm x^2 - t^2)$ and

$$B^2 = [(t+x)^2 - \varepsilon_{max}^2][(t+x)^2 - \varepsilon_{min}^2][\varepsilon_{max}^2 - (t-x)^2][\varepsilon_{min}^2 - (t-x)^2]$$

In Eq. (5) the angular distribution $f(E, \mu)$ was introduced, which gives the correlation between the energy of the incident neutron and the emission angle after the scattering process. It is a normalized probability distribution where $f(E, \mu)d\mu$ is the probability that a neutron of incident energy E will be scattered into the interval $d\mu$ about an angle the cosine of which is μ. This property originates from the representation of the anisotropy in scattering in the center-of-mass for the cross-section in Eq. (3) as

$$\sigma_s^{tab}(E, \mu) = \frac{1}{2\pi} \sigma_s^{tab}(E) f(E, \mu)$$

For isotropic scattering in the center-of-mass, $f(E, \mu)$ is equivalent to the $P(\mu_{CM})$ of Ref. [43] and then $f(E, \mu) \equiv P(\mu_{CM}) = 1$.

In the present work, the angular distribution $f(E, \mu)$ is obtained from "File 4" of the basic evaluated nuclear data files as available in either ENDF/B-VII or JENDL libraries [56]. Depending on the isotope under consideration, these data may be given in one of three forms, and in either center-of-mass or laboratory coordinate systems. In the first form, the distributions are given by tabulating the normalized probability distribution $f(E, \mu)$ as a function of the incident energy. In the second form, the angular distribution is represented as a Legendre polynomial series as

$$f(E, \mu) = \sum_l^{N_l} \frac{2l+1}{2} a_l(E) P_l(\mu)$$

In this case, the Legendre polynomial expansion coefficients $a_l(E)$ are tabulated as a function of incident energy. The expansion order N_l is also given in the file as incident energy dependent. The third form is a combination of the two previous forms; thus, the data for an isotope could be the tabulation for one part of the energy domain (usually high energies) and the Legendre expansion for the remaining part. The type of data depends on the evaluated library used. The details of the implementation of this theory can be found in Ref. [45].

2.2.2.2 Multi-group Formulation and NJOY implementation

The complexity of Eq. (3) renders it difficult to implement analytically or semi-analytically and thus imposes extra care both in the coding and in the numerical formulation. In the implementation of the model embodied by this equation, it is not known a priori if the evaluated angular distribution $f(E, \mu)$ is available

as an expansion in Legendre polynomials or in tabulated form. This lack of prior knowledge, forces the use of numerical integration for all the integrals in this equation.

In the implementations known so far (see references in Ref. [45]), there is no accounting for anisotropy in scattering in the center-of-mass frame, i.e. $f(E, \mu) = 1$, and this makes it possible to compute the inner integrals on the x and ϕ variables in Eq. (5) analytically, especially for the isotropic (zeroth) moment [43]. It is also possible to compute the integral over the t variable analytically by choosing a linear piecewise representation for the cross-section $\sigma_s^{\text{tab}}(E)$. These assumptions are good only for the zeroth - and first order scattering transfer moments; for higher orders, the formulation becomes cumbersome, and using numerical schemes becomes unavoidable.

The multi-group formulation adds two integrals to the process of evaluating Eq. (1). The two integrals are over the initial and final energy groups. The multi-group formalism is usually used in lattice physics codes with relatively broad energy groups (practically between about 70 and 540 groups) along with a pre-requisite and prior resonance self-shielding treatment. The resonance calculation always includes a method to account for the resonance interference both in energy (between various isotopes within a local mixture) and space (between isotopes in different pellet rings and/or different locations in the assembly). Instead of this approach, the formulation of Eq. (1) was implemented using an ultra-fine energy mesh with 6064 energy groups which reproduce the continuous energy Monte Carlo results [36]. This approach was chosen to treat a mixture of resonant isotopes better, avoiding altogether the inaccuracy that may occur in the resonance self-shielding theory. This allows, as shown later, a very-high-fidelity representation of the effect of the new resonance scattering model introduced in this document and thus a much finer analysis of its impact and consequences. The formulation of the multi-group scheme follows.

Suppose that the energy domain is discretized according to

$$[0MeV, 20MeV] = \bigcup_g [E_g, E_{g+1}].$$

The scattering moments from an initial group g to a final group g' are given by

$$\sigma_{sn}^T(g \rightarrow g') = \int_{E_g}^{E_{g+1}} dE \int_{E_{g'}}^{E_{g'+1}} dE' \, \sigma_{sn}^T(E \rightarrow E') \,,$$

and the total Doppler-broadened scattering moments are given by

$$\sigma_{sn}^T(g) = \sum_{g'} \sigma_{sn}^T(g \rightarrow g') \,.$$

After the change of variable $\frac{\beta kT}{A} t^2 \rightarrow t$ and expanding $\sigma_{sn}^T(E \rightarrow E')$ in the above equation, there follows

$$\sigma_{sn}^T(g \rightarrow g') \quad = \frac{A\beta^{3/2}}{4kT\pi^{3/2}} \int_{E_g}^{E_{g+1}} dE \int_{E_{g'}}^{E_{g'+1}} dE' \int_0^\infty dt \int_0^\infty dx \int_{-1}^1 \frac{1}{\sqrt{1-\xi^2}} d\xi \, \mathcal{F}(E, E', t, x, \xi) \mathcal{H}(t$$
$$- t_+)\{\mathcal{H}(t_- - t)\mathcal{H}(x_- - x)\mathcal{H}(x - x_+) + \mathcal{H}(x'_- - x)\mathcal{H}(x - x'_+)\} \,, \quad (6)$$

Where,

$$\theta = \sqrt{\frac{A+1}{kT}} \, , \gamma = \sqrt{\frac{A}{\beta kT}} \, , x_- = \theta\sqrt{E_{max}} - \gamma\sqrt{t} \, , x_+ = \theta\sqrt{E_{min}} + \gamma\sqrt{t} \, ,$$

$$x'_\pm = \gamma\sqrt{t} \pm \theta\sqrt{E_{min}} \, ,$$

And,

$$\mathcal{F}(E, E', t, x, \xi) = \sigma_s^{tab}(t) \frac{e^{\frac{E}{kT} - \frac{t}{\beta kT} - x^2}}{E} P_n(\mu_{lab}) f(t, \mu_{CM}) \, .$$

Equation (6) is valid for upscattering ($g' \leq g$) and downscattering ($g' \geq g$). The approach taken in numerically computing all the integrals in this expression is outlined in Ref. [45]. In addition, Ref. [45] contains a more detailed discussion on the equations and variables listed above.

A new FORTRAN module, RSM, that implements the model presented above has been added to the NJOY code system [22]. This module is used to create an UFEML, based on the 6064-energy-group structure previously mentioned [37]. All the cross-sections in UFEML are tabulated only as a function of temperature since with this type of energy mesh the conventional resonance treatment is not needed. In this model, [

]^{a,c}. All the isotopes in UFEML have the resonance scattering accounted for in the scattering matrices following the method presented in this document, except two: hydrogen (in H_2O) and carbon in graphite, which use the asymptotic model (i.e. $1/E$ in the epithermal range and $S(\alpha, \beta)$ in the thermal range). For consistent comparison and for quantification of the impact of the new resonance scattering model, an equivalent library based on the asymptotic model for all the isotopes was generated. These two libraries are based on the ENDF/B-VII and JEFF evaluated nuclear data files. These libraries are used to perform the analyses presented in the following sections. The analyses were performed using the lattice physics transport code PARAGON2.

2.2.2.3 Continuous-Energy Transfer Kernel

The first verification of the algorithm implemented within the RSM module aimed at reproducing the isotropic continuous energy transfer kernel $\sigma_{s0}^T(E \to E')$ of Eq. (3) as reported in Ref. [43]. This can be achieved by using an energy mesh with very thin groups, such that

$$\lim_{\delta_g \to 0, \delta_{g'} \to 0} \sigma_{sn}^T(g \to g') = \sigma_{sn}^T(\bar{E} \to \bar{E'}) \, ,$$

where $\delta_g = E_g - E_{g+1}$ and $\delta_{g'} = E_{g'} - E_{g'+1}$ and where $\bar{E}$ and $\bar{E'}$ are the mid points of energy groups g and g', respectively.

To be consistent with previously published results, Figure 2-1 through Figure 2-3 present the energy transfer probability defined by

$$p_0^T(\bar{E} \rightarrow \overline{E'}) = \frac{\sigma_{s0}^T(\bar{E} \rightarrow \overline{E'})}{\sigma_{s0}^T(\bar{E})},$$

where,

$$\sigma_{s0}^T(\bar{E}) = \sum_{g'} \sigma_{s0}^T(g \rightarrow g').$$

Note the comparison in Figure 2-1 through Figure 2-3 is to the scattering cross-section at 0 K, which is represented as the black line.
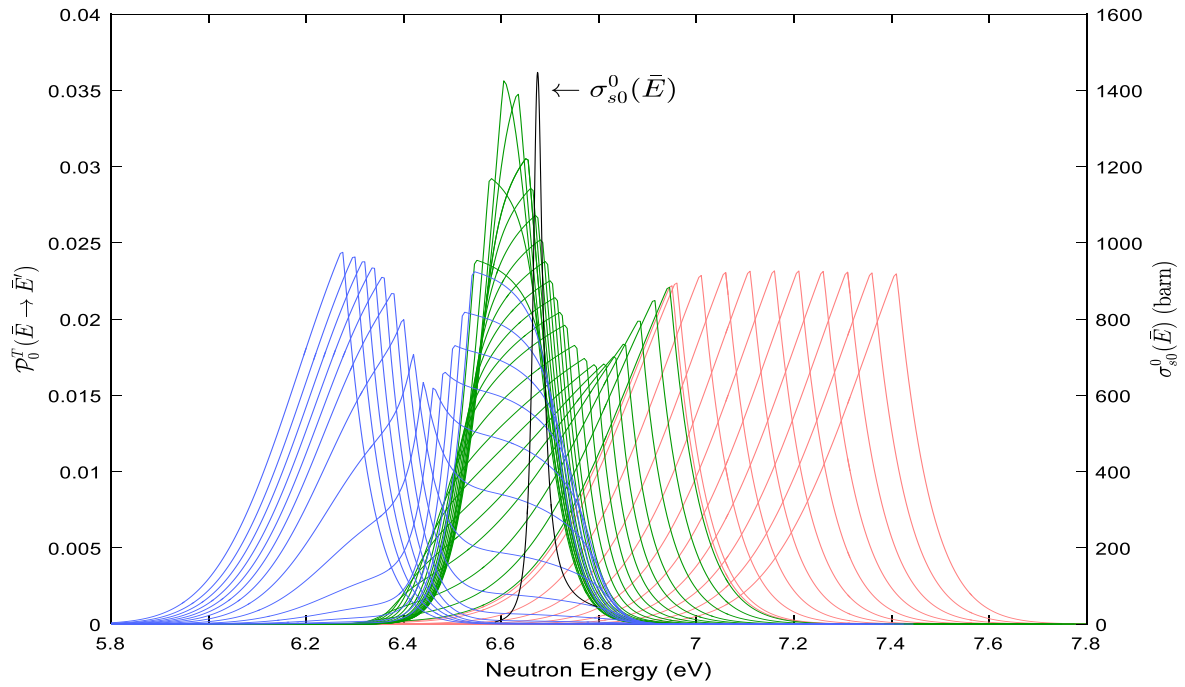
Figure 2-1: Continuous-energy transfer kernel for various initial neutron energies around the first resonance of U-238 at 1100 K
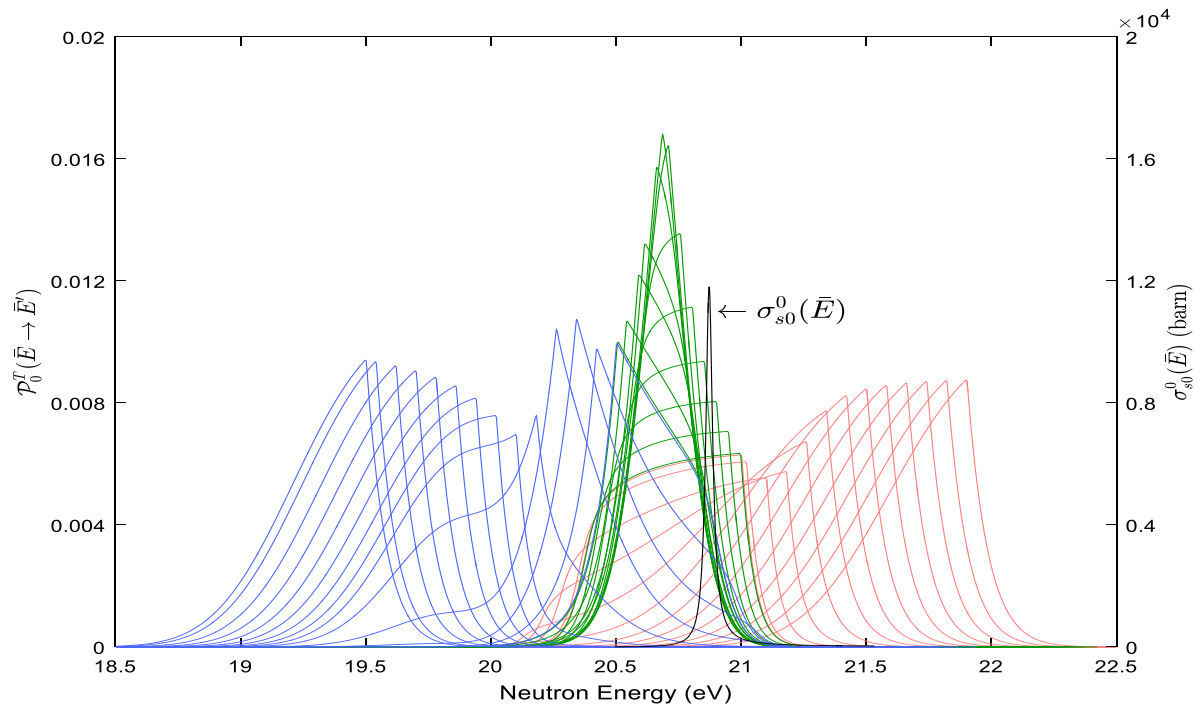
Figure 2-2: Continuous-Energy transfer kernel for various initial neutron energies around the second resonance U-238 at 1100 K
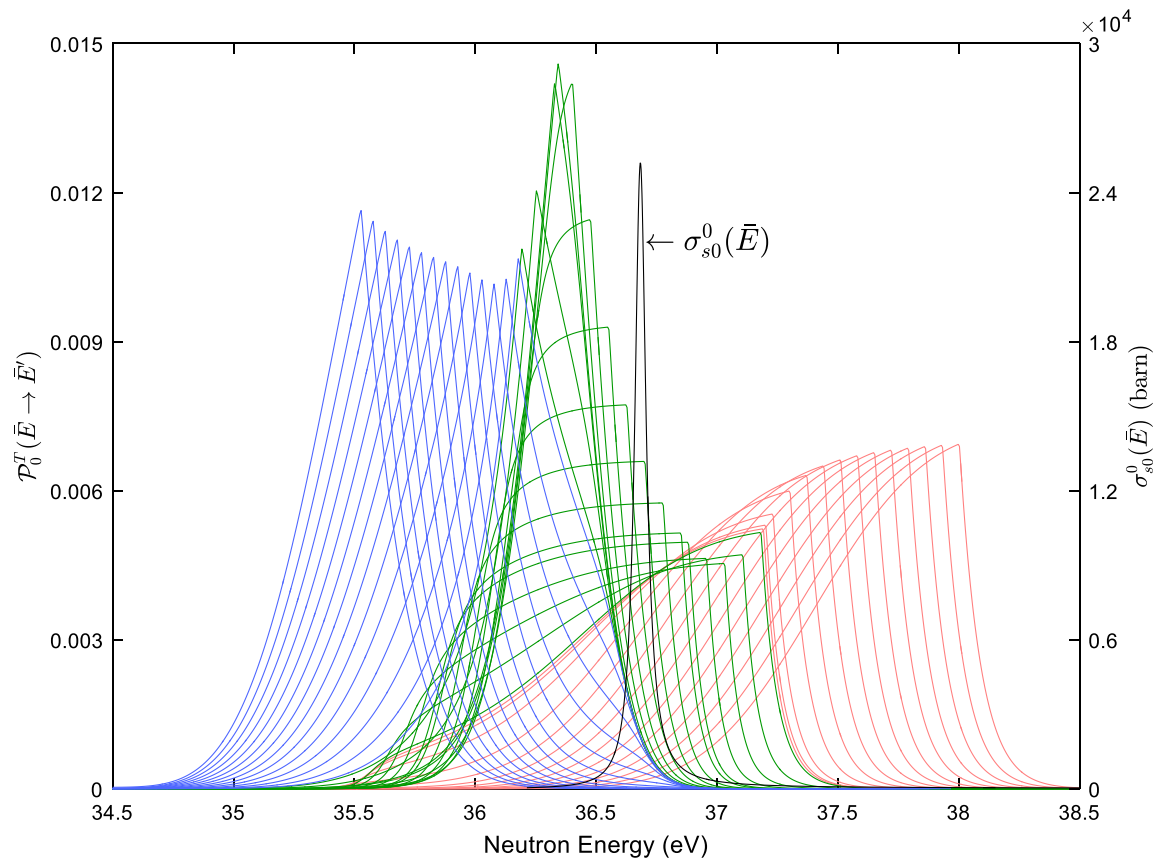
Figure 2-3: Continuous-energy transfer kernel for various initial neutron energies around the third resonance of U-238 at 1100 K.

Figure 2-1 through Figure 2-3 display the transfer probability for several starting neutron energies around the first three important resonances of U-238. Each figure also shows how the shape of this probability changes around the resonance as previously discussed in Ref. [43]. These figures clearly reproduce the results in Ref. [43]. The effect of the scattering anisotropy and the shape of the multi-group kernel are discussed in detail in Ref. [45]. The use of color is to illustrate the impact of the resonance on the upscattering phenomenon (for example, the green colors are for the initial neutron energies that are very close to the peak of the resonance scattering cross-sections).

2.2.2.4   Impact of the RSM on Neutronics Parameters

2.2.2.4.1   Doppler Benchmarks

The effect of the use of the new RSM approach on reactivity is evaluated via its application to the analysis of selected cases of the Mosteller's Doppler reactivity benchmarks [29]. This is accomplished using the lattice code PARAGON2 and comparing results obtained utilizing both RSM and asymptotic (ASYMP) UFEML cross-section libraries. The results are reported in Table 2-1. The Hot Zero Power (HZP) and the Hot Full Power (HFP) cases correspond to fuel temperatures of 600 and 900 K, respectively. The material compositions, pin cell dimensions and other detailed benchmark descriptions are given in Ref. [29]. The PARAGON2 code, with its associated UFEML library, will be qualified against a Monte Carlo solution in subsequent sections. Here, the focus is on comparing the PARAGON2 results obtained with and without the resonance scattering model discussed in Section 2.2.2. As per expectations, the RSM effect depends on the temperature and on the actual isotopic composition of the material (including enrichment levels). The effect becomes stronger as the temperature increases and tends to lower the reactivity. In the last column of Table 2-1, the Doppler Coefficients of Reactivity (DCR) are compared. Within the table, the DCR is denoted by ρ_x, with the subscript "x = 0" standing for RSM and "x = a" standing for asymptotic. As defined in Ref. [29], $\rho_x = \frac{\delta_k}{\delta_T}$, where $\delta_k = \frac{1}{k_{eff}^{HZP}} - \frac{1}{k_{eff}^{HFP}}$ and $\delta_T = 300\ K$ (the difference between the two temperatures at which the multiplication factor is evaluated). The difference in DCR between the RSM and asymptotic models is in the range of 7% to 9%. For a typical reactor core, this corresponds to a ~ 100 pcm difference in reactivity, which is relatively large since in the design and safety analysis practice the accuracy on $\Delta\rho$ Doppler defect is estimated at 200 pcm. If it is assumed that the DCR is analogous to the Doppler Temperature Coefficient (DTC) that is part of the important Isothermal Temperature Coefficient (ITC), then the difference seen in the DCR seems to be significant. This difference in DCR translates to ~0.7 to ~1.3 pcm/°F, which is almost half of the ± 2 pcm/°F tolerance that is desired in measurement comparisons on the ITC (note, the ITC is sum of DTC and the moderator temperature coefficient (MTC)).

The results obtained for UO_2 in this study are consistent with those of Ref. [18] but slightly lower. There are many reasons to explain why the present results are different from those reported in this or other references. The reasons include the following:

1. RSM scattering matrices (in the present implementation) account for the anisotropy in the center-of-mass frame.

2. The scattering matrices incorporate the RSM-based P_1 anisotropic corrections (consistent with the libraries used for core design applications).

3. All isotopes (except H-1) are treated using the RSM model (including cladding material).

4. The Monte Carlo solution used in Ref. [18] restricts the application of the resonance scattering formalism to only a limited portion of the energy domain.

This claim is amply supported by a simple verification. For this verification, all the cases in this benchmark were modeled again, but with a cross-section library in which only the U-238 isotope is treated using the RSM model while all other isotopes are treated using the asymptotic scattering model. With these new runs, the 9% to 10% range differences are reproduced for UO_2 fuel, matching the results that were reported in

Ref. [18]. Results for the mixed-oxide (MOX) cases were mixed: some of the cases showed an increase while others decreased. Furthermore, the difference range was **[   ]**[a,c].

Table 2-1: PARAGON2 Results for Pin Cell Doppler Benchmark Using UFEML Cross-section Library

[a,b,c]

$$\left[\right]$$

It is important to note that the contribution of heavy isotopes to the scattering process is dominated by U-238 due to its many resonances and to its high concentration in ordinary reactor fuel. However, turning off the RSM contribution of non-heavy isotopes in the previous runs shows that the RSM contribution of the less heavy isotopes in the DTC calculation is not negligible.

2.2.2.4.2   Effect of Fuel Temperature

To quantify the temperature effect on the resonance scattering, the fuel temperature is varied from 600 to 2500 K and compared the reactivity difference between the asymptotic and RSM models; i.e., $k_{eff}^{ASYMP} - k_{eff}^{RSM}$. The cladding and moderator are kept at the same 600 K temperature throughout the computational test. Figure 2-4 shows the results for both the 5 wt% UO$_2$ and the 8 wt% reactor-recycle MOX pin cells of the Mosteller benchmark. As expected, the difference between the two models increases with temperature and could exceed 500 pcm at high temperatures. The model temperatures of the nonfuel materials for these transient situations are not realistic but are used to allow us to single out the differences that arise with changes in fuel temperature. In this work, this effect was also studied on three models of typical 17x17 PWR-type fuel assembly, assuming the same fuel temperature variations. One of these assemblies contains an IFBA, the second incorporates a gadolinia absorber, and the third is a zoned MOX assembly. All three are standard fuel types. The results are shown in Figure 2-5, in which the same trend is observed as for a single pin cell in Figure 2-4. The magnitude of the difference in this case is slightly less

than that found for the pin cell case, yet it remains significant. A priori, a large difference was expected in the case of MOX fuel because of the heterogeneity of its composition, but the results show almost the same effect as for the UO$_2$ fuel. However, a closer look at the compositions reveals that the major contributor to the temperature- and resonance-related changes in the effective multiplication factor is U-238, which is present with the largest number density for all these mixtures, including MOX.

In this analysis, a flat temperature was used within the fuel pellet. In reality, this temperature is not spatially constant but exhibits a profile. To evaluate the impact of this assumption, the pellet was subdivided into ten equal-volume zones and the typical UO$_2$ temperature profile given in Table 2-2 was used. In the computational runs the temperature distribution was normalized in such a way that its average is equal to the flat value used in the study just discussed above, i.e., values from 600 to 2500 K. The results are reported in Figure 2-4, in which it can be seen that for the reactivity prediction, the pellet temperature profile has practically no effect and the results are very close to the flat temperature results. [45]

Table 2-2: UO$_2$ Temperature Profile for Ten Equal-Volume Rings in the Pellet

Ring Number*	Fuel Temperature (K)
1	1070.30
2	1029.80
3	990.35
4	951.88
5	914.40
6	877.90
7	842.36
8	807.75
9	774.04
10	741.23

The numbering is from center to periphery, and this case is normalized to the average of 900 K.
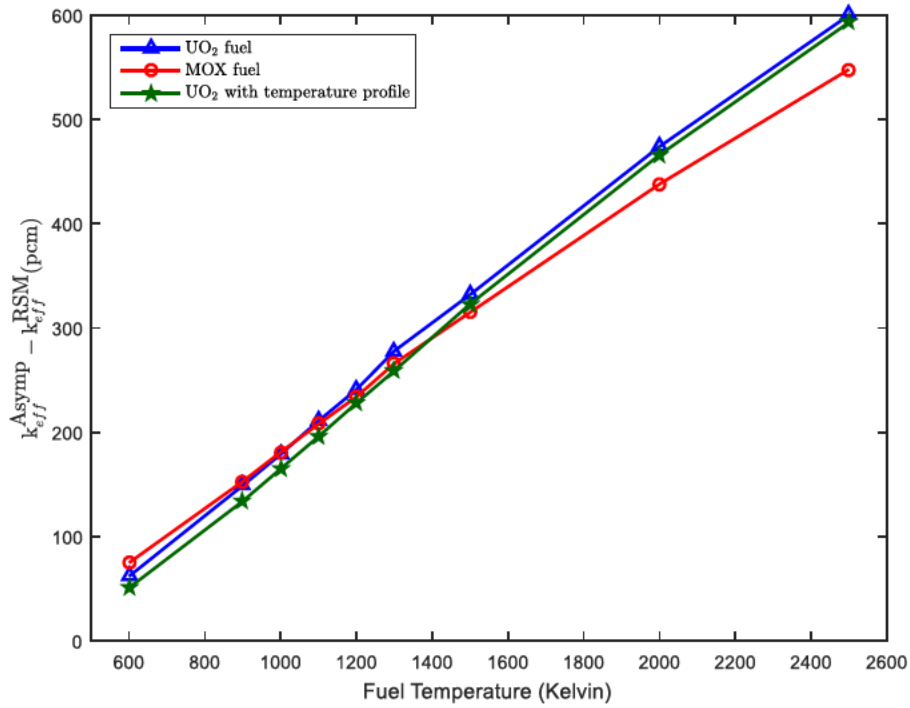
Figure 2-4: Fuel Temperature Effect – Pin Cell Cases
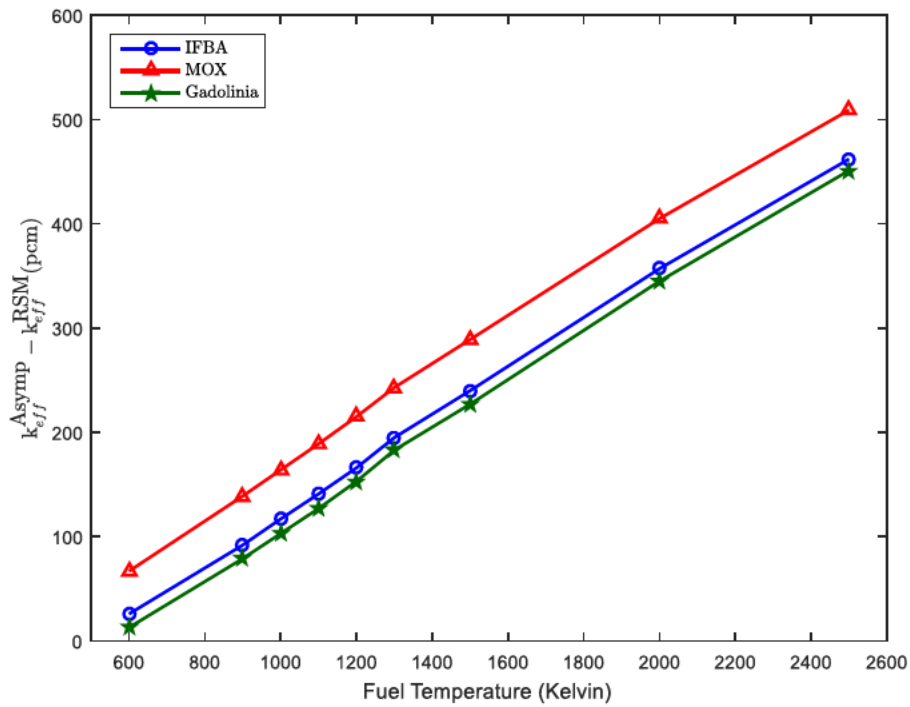
Figure 2-5: Fuel Temperature Effect – Assembly Cases

2.2.2.4.3   Impact on the Multi-group Fluxes

The effect of the RSM on the multi-group fluxes is assessed using the cases with a fuel temperature of 1200 K. Two models are investigated, one with a single fuel region, the other with ten equal-volume regions within the fuel pellet but still with a flat temperature profile. The relative difference between the asymptotic and the RSM results is computed for all of the 6064 UFEML energy groups. The results are plotted in Figure 2-6 for both the 8 wt% reactor-recycle MOX and the 5 wt% UO_2 pin cells. For the majority of the energy groups the difference is relatively small, but for some groups, near the resonances, very large differences arise. For the single region model, and around the 36 eV resonance of U-238 (third resonance), the group-wise difference can exceed 50% for the MOX and UO_2 fuels. When the pellet is discretized into multiple regions, the difference is even larger and can go beyond 100% in some middle rings, again at the same energy groups around the third resonance of U-238. Though not shown in any of the figures, the same effect of large differences was obtained when a temperature profile is used in the pin cell modeling. As expected, Figure 2-6 shows significant deviations in the resonance range. It also shows that the deviations are not all in the same direction (i.e., there are positive and negative differences), which explains the moderate magnitude of the differences obtained for the k_{eff} eigenvalues. Indeed, had all the deviations been in the same direction, the difference in reactivity would have been larger. Another important fact seen in Figure 2-6 is the disparities at high energy, which are attributed to the anisotropy model in the RSM module (see Ref. [45] for more explanation).

The gadolinia pin cell results in Figure 2-6 pertain to one of the pins in the case of the assembly that contains gadolinium. This pin was modeled with ten equal-volume rings and a constant temperature of 1200 K. For the high energy and the resonance ranges, the same trend is observed in the flux differences, in both magnitude and direction. However, in the thermal range, in contrast to the pure fuel pin results, large differences are observed for pins of this type. Another remarkable characteristic of this gadolinia case is that the difference is almost constant across the rings, while for pure fuel, the differences tend to be low at the periphery and high from the mid-thickness to the center of the pin. This is probably an artifact of the transport property of the thermal versus epithermal neutrons as they migrate from one region to another in a way that depends on their respective mean free paths.

In Ref. [45], more cases are studied including new fuel concepts and the impact of RSM on the depleted fuel. The above results show a large impact of the RSM on micro-energy groups fluxes because the resonance scattering cross-section amplifies the upscattering phenomenon. However, the impact on the global parameters such as reactivity or total reaction rate is not as large as the differences seen at a micro level because of compensatory effects.
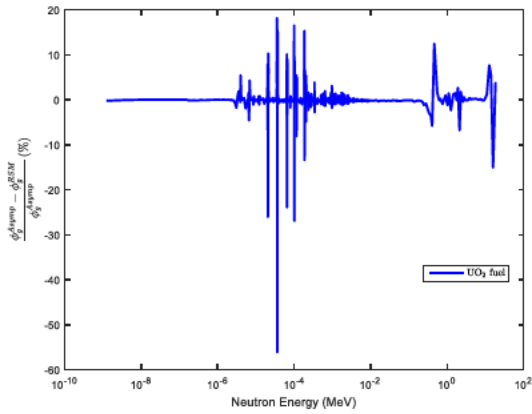
(a) UO₂ pin cell with one fuel region
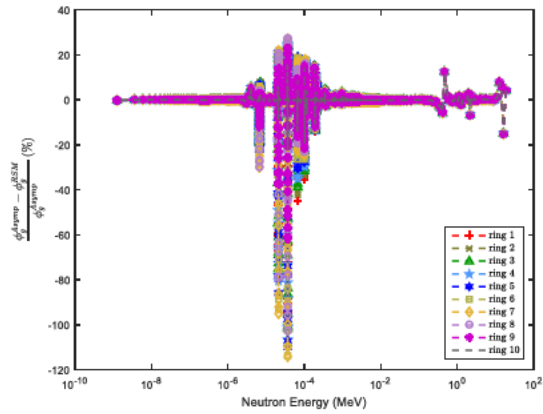
(b) UO₂ pin cell with ten regions in the fuel
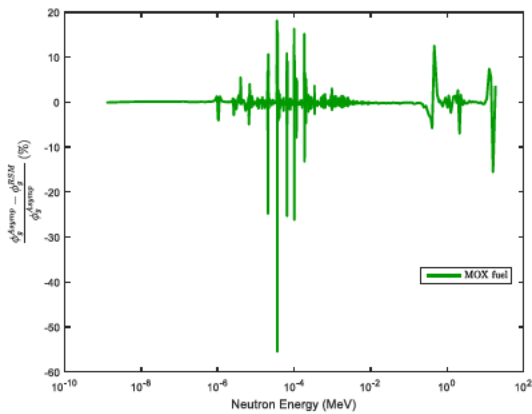
(c) MOX pin cell with one fuel region
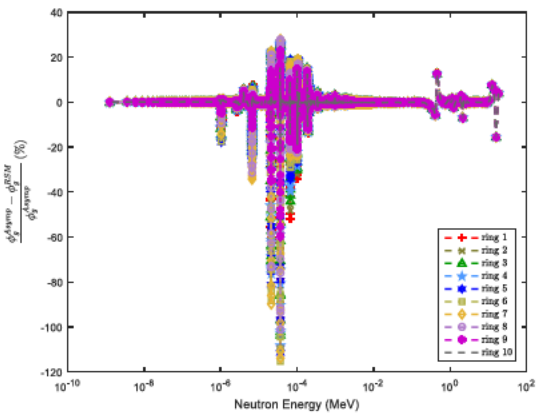
(d) MOX pin cell with ten regions in the fuel
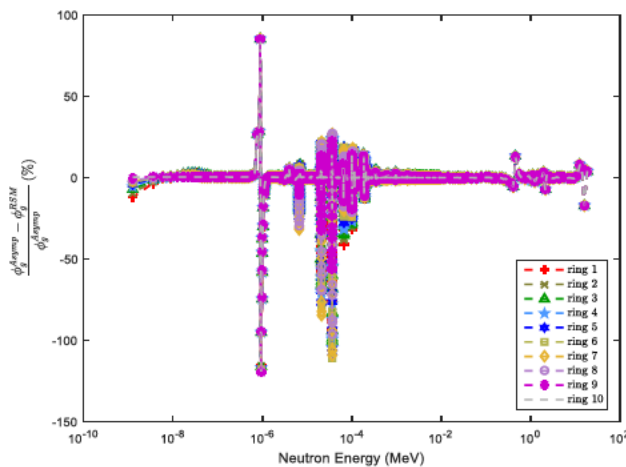
(e) Flux differences in a pin cell with gadolinia

Figure 2-6: Comparison of Asymptotic and RSM multi-group fluxes
(Energies shown on the x-axis are the middle point of the UFEML group structure)

2.3   PARAGON2 THEORY – AN OVERVIEW

This section is to provide a brief overview into the PARAGON2 modules. PARAGON2 uses the same flux solver, depletion solver and leakage correction model as PARAGON. These modules are described in Ref. [41], but for the sake of completeness, the description of these modules are repeated in this section.

2.3.1   Theory of PARAGON2 Modules

2.3.1.1   Flux Calculation Module

The neutron (or gamma) flux, obtained from the solution of the transport equation, is a function of three variables: energy, space and angle. For the energy variable, PARAGON2 uses the multi-group method where the flux is integrated over the energy groups. For the spatial variable, the assembly is subdivided into a number of sub-domains or cells and the integral transport equation is solved in the cells using the collision probability method. The cells of the assembly are coupled using the interface current technique (Ref. [40]). At the interface, the solid angle is discretized into a set of cones (Refs. [39] and [40]) where the surface fluxes are assumed to be constant over each angular cone. PARAGON2 has been written in a general way so that the cell coupling order is limited only by the computer memory. The collision probability method is based on the flat-flux assumption, which will require subdividing the cells into smaller zones. Thus, for each cell in the assembly, the system of equations to be solved is given by the discretized one energy-group transport equation:

$$\begin{cases} \overrightarrow{\phi^g} = \mathbb{P}_{vs}^g \overrightarrow{J_-^g} + \mathbb{P}_{vv}^g \overrightarrow{S^g} \\ \overrightarrow{J_+^g} = \mathbb{P}_{ss}^g \overrightarrow{J_-^g} + \mathbb{P}_{sv}^g \overrightarrow{S^g} \\ \overrightarrow{J_-^g} = \mathbb{B}^g \overrightarrow{J_+^g} \end{cases}$$

Where for an energy group g (neutron or photon):

- $\overrightarrow{\phi^g}$ is the volume flux for the spatial grid,
- $\overrightarrow{J_\pm^g}$ are the angular moments of the currents at cells interfaces,
- $\mathbb{P}_{sv}^g, \mathbb{P}_{ss}^g, \mathbb{P}_{vv}^g$ and $\mathbb{P}_{vs}^g$ are the escape, transmission, first flight, and surface to volume collision probabilities,
- $\mathbb{B}^g$ is the albedo boundary condition matrix at the external surfaces and
- $\overrightarrow{S^g}$ is the spatial vector source.

The solution of the above algebraic system of equations over the entire assembly is obtained by the response heterogeneous matrix method, which uses current-flux iterations (Refs. [40] and [55]). The details describing this module can be found in Refs. [39], [40], and [41].

2.3.1.2   Homogenization Module

The next step in PARAGON2 calculation after the flux solution is the leakage correction. The purpose of this module is to compute the multi-group diffusion coefficients and the multi-group critical flux (spectrum) for the entire homogenized assembly (or parts of the assembly, like baffle/reflector regions). The same B_1 theory used in PARAGON is also used in PARAGON2. The critical flux is obtained by solving the

fundamental mode of the transport equation. This theory is described in Ref. [41] and will not be repeated here.

For each energy group, the micro-region fluxes are corrected by the ratio of the fundamental mode fluxes and the assembly averaged fluxes to get the final micro-region critical fluxes.

The second model of PARAGON (Ref. [41]) to compute the critical flux has also been maintained in PARAGON2. In this model, the neutron source is modified by adding an artificial absorption cross-section $D_g B^2$ in each micro-region of the assembly. In this case, the diffusion coefficients are first computed by using the previous model. In case of fuel assemblies, the two models are comparable. The second model is mainly used in the case of critical experiments for which a measured buckling (B^2) is usually available.

2.3.1.3   Depletion Module

The assembly composition changes following neutron irradiation are obtained by calculating the isotopic depletion and buildup in the heterogeneous geometry, using an effective one-group collapsed flux and cross-sections. PARAGON2 uses the same solver and method as PARAGON (Ref. [41]), including the predictor-corrector technique.

The code detects automatically the regions to be depleted, but the user has the option to hold any region in the assembly as non-depletable. For the boron depletion, the user has a choice of depleting it according to a letdown curve that is provided through the input or exponentially (i.e. depletion chain). Note that gamma heating is taken into account in the evaluation of the flux level during the burnup depletion using the same approach as in PARAGON.

The development of PARAGON2 took advantage of the new evaluated data of the elements in ENDF/B-VII (actinides, fission products, burnable absorber materials, etc.) to improve the core depletion predictions. [

]**a,c**

An additional change introduced in PARAGON2 is the energy dependent fission product yields. An effective yield is generated inside PARAGON2 to perform the depletion using isotopic energy-dependent yields directly obtained from the ENDF/B-VII basic nuclear data. For PWR applications, this has little effect compared to the old method that is based on an average yield (i.e. energy independent). Another important change is [   ]**a,c**

These newly adopted depletion chains were benchmarked with even more detailed chains [

]**a,c**. Since PARAGON2 is using a large number of energy groups and the assembly modeling can employ a detailed representation of the fuel pins (multi-rings), the usage of the optimal depletion chains was paramount to achieve acceptable running times. Any more complex or detailed depletion chains would not contribute to the accuracy of the results.

2.3.1.4   Other Modeling Capabilities

PARAGON2 maintained other important modeling capabilities for core design applications with changes in fuel temperature as described in the following section.

2.3.1.4.1 Photon Transport Calculation

PARAGON2 uses the same theory and module of PARAGON for the coupled Neutron-Photon transport calculation [35]. The photon transport calculation is carried out using 97 energy groups coupled with the gamma production from neutron captures computed using 6064 neutron energy groups. The gamma source includes prompt fission gamma and gamma rays from other neutron reactions such as capture, inelastic scattering, (n,α), etc. if the necessary data are available in the basic evaluation nuclear data file (ENDF/B-VII or others). [   ]ᵃ,ᶜ

PARAGON2 computes [

]ᵃ,ᶜ. The gamma heats are generated in the user defined detailed geometry.

2.3.1.4.2 Temperature Model

Through the input, PARAGON is provided with [
]ᵃ,ᶜ. The user can provide [

]ᵃ,ᶜ.
Different sets of these tables form different "media" that are later assigned to different zones of different cells in the assembly model. Same table can also be used by PARAGON2. However, since PARAGON2
[

]ᵃ,ᶜ. The two approaches are equivalent
and can be used in design.

2.3.1.4.3 Doppler Branch Calculation

As was approved by the NRC for use in the PARAGON code (Ref. [41]), a doppler branch calculation capability has been built into PARAGON2. This capability permits fuel temperature variations to be modeled while keeping all other parameters constant. Results of these calculations are used to generate changes [   ]ᵃ,ᶜ, which
are passed to the core models to capture Doppler effects. [

]ᵃ,ᶜ.

2.3.1.4.4 Thermal Expansion

A model to expand the radii of the cylindrical region has been implemented in PARAGON2. [

]ᵃ,ᶜ The code uses this
capability mainly in the case of the Doppler branch calculation. It also has a flag to turn it on in any calculation step.

2.3.1.4.5 Interface Module

PARAGON2 has the flexibility of printing many types of micro- and macro-based physics parameters. Hence, the user can request to edit the fluxes, partial currents, surface fluxes, different reaction rates, isotopic distribution etc. The editing could be done for micro-regions, for an average over a cell, for an average over a group of cells, and/or for any number of energy groups (i.e. the code can collapse to any number of groups for editing).

PARAGON2 uses files to store the data needed for core calculations. Those files are processed by other codes used for core modeling and analysis.

2.3.1.4.6   Reflector Modeling

PARAGON2 generates the reflector constants using a [

]**a,c**

Page Intentionally Left Blank

3   CRITICAL EXPERIMENTS AND ISOTOPICS MEASUREMENTS

3.1   CRITICAL EXPERIMENTS

3.1.1   Integral Experiments

The purpose of the designated integral critical experiments is to assess the PARAGON2 predictions of fine neutronics parameters such as resonance integrals, radial profile distribution of reactions rates, and radial distribution of the isotopic concentrations for burned fuel and permit the use of PARAGON2 in such calculations. The prediction of reactivity as a function of uranium enrichment and geometrical data will also be assessed using these types of experiments. As appropriate, PARAGON2 with cross-section libraries using either the resonance scattering model or asymptotic model will be used in these analyses to contrast the differences of these two physics models.

3.1.1.1   Hellstrand's Experiments – U-238 Resonance Integrals

Description of the experiments

The Hellstrand's experiments for measuring U-238 resonance integral (RI) were performed in a Swedish heavy water reactor. Fuel rods of uranium metal or uranium oxide were placed in a cadmium-covered oven and irradiated in the central channel of the reactor. Additional details on these experiments are described in Refs. [11]-[13]. The main neutron reaction is neutron capture in U-238 that transmutes into Np-239. The activity of Np-239 is proportional to the neutron capture of U-238. The samples of the original experiments include uranium metal and oxide (UO_2). The capture rate measured by the experiment is primarily in the resonance energy range. The RI, which is the U-238 capture rate, needs to be normalized for comparison among different sample temperatures. The measured epithermal flux outside the sample was used to normalize the RI to the unit epithermal flux. The detailed information of the reactor core is not important in evaluating the resonance integrals, because the idea of the experiment was to create a 1/E spectrum outside of the sample. The amplitude of the flux that relates to the core configuration is not important because RI is normalized to the unit 1/E epithermal flux.

PARAGON2 Modeling description

In Ref. [21], a simplified model that mimics the 1/E flux surrounding the fuel sample was developed. This same model is also adopted in this study. Thus, a 2D 3x3 array of assembly blocks (with 7x7 pins per assembly) are modeled in PARAGON2. The center block contains the fuel cell sample and the other cells of this block are moderator cells (without fuel). The flux in this moderator of this central region is used for normalization of the reaction rate as suggested in Ref. [21]. Both uranium metal and oxide samples are modeled using heavy water as the moderator. As suggested in Refs. [11]-[13] and [21], the energy domain for the epithermal capture U-238 reaction rates is chosen to be between 0.39 eV and 110 keV.

Results

The temperature coefficients were simulated for the sample radius of 0.4 cm for both uranium oxide and metal. Fuel temperatures were varied from 300 to 1500 K. The following formulas from Ref. [13] were used to compute the Hellstrand experimental resonance integral values:

$$\text{Oxide:} \quad RI = RI_0\left[1 + 0.00824\left(\sqrt{T} - \sqrt{T_0}\right)\right]$$
$$\text{Metal:} \quad RI = RI_0\left[1 + 0.00642\left(\sqrt{T} - \sqrt{T_0}\right)\right]$$

Where, RI is the U-238 resonance integral for fuel temperature T and RI_0 is the corresponding value for the temperature $T_0 = 300$ K.

Figure 3-1 and Figure 3-2 show the U-238 predicted PARAGON2 resonance integrals compared to the Hellstrand experimental values. PARAGON2 results using the RSM demonstrate good agreement with the experiments. Using RSM, PARAGON2 coefficient values are **[**

][a,c]. As expected, the asymptotic results show deviation from the experiment as the fuel temperature increases. The good agreements, of PARAGON2 with experiment, show the importance of the resonance scattering model and the fine energy mesh in predicting the temperature coefficients and Doppler Effect.

The uranium metal results show larger deviations compared to the oxide case. This discrepancy is most likely attributed to the inaccuracy of the measurement as explained in Ref. [12].

Refs. [11]-[13] contain also the absolute U-238 resonance integral correlated to the $\sqrt{S/M}$, where S/M is the surface to mass ratio of the fuel pellet in cm^2/g. The experimental correlations are given by the following formulas:

$$\text{Oxide:} \quad RI(\text{barns}) = 4.15 + 26.6\sqrt{S/M}$$
$$\text{Metal:} \quad RI(\text{barns}) = 2.95 + 25.8\sqrt{S/M}$$

Note that the equation for the metal case has been obtained from Ref. [12]. This formulation is a correction of the one published in Ref. [11] and it has been obtained after conduction of new more precise experiments.

PARAGON2 with RSM was used to model different fuel rod sizes. The experiment fuel temperature is assumed to be 300 K. Figure 3-3 and Figure 3-4 show the comparison of PARAGON2 results against the experiments for both oxide and metal fuels. Good agreement between experimental values and PARAGON2 predicted values is seen in these figures. **[**

][a,c]

This analysis provides a proof that PARAGON2 does predict accurately the resonance integral for all fuel rod sizes and for heavy fuel density (such as metal fuel).

a,b,c

Figure 3-1: Temperature Coefficient of the U-238 Resonance Integral – Uranium Oxide

a,b,c

Figure 3-2: Temperature Coefficient of the U-238 Resonance Integral – Uranium Metal

[   ] a,b,c

Figure 3-3: Resonance Integral – Uranium Oxide

[   ] a,b,c

Figure 3-4: Resonance Integral – Uranium Metal

3.1.1.2 Radial U-238 Resonance Capture Distribution

Description of the experiment

The relative U-238 resonance neutron capture per atom was measured for cylindrical, 0.387 in. diameter rods of uranium metal, UO_2 (density 10.5 g/cm^3) and U-Zr alloy (74.9 wt% U, 25.1 wt% Zr) placed in a water hole in the TRX critical facility. In all cases, the uranium was enriched to 1.3 wt% U-235. The density of U-238 atoms in each alloy was the same as in the UO_2 fuel. The measurement techniques are similar to the ones used in Hellstrand's experiments including measurement for the radial distribution of the U-238 resonance capture. The experiments and results are described in Ref. [51].

PARAGON2 modeling description

The references available for this experiment have little information for purpose of developing a detailed model. Therefore, a single pin cell was modeled in PARAGON2. Since the geometry of the TRX experiment is hexagonal, and PARAGON2 cannot model this geometry, the square cell modeled is developed by preserving the fuel to moderator ratio. Small volume rings are used at the measurement points to simulate the foils used in the experiments.

Results

Figure 3-5, Figure 3-6, and Figure 3-7 provide the comparison between the measured relative U-238 capture resonance reaction rates for UO_2, uranium metal and U-Zr fuel pellets. These figures show good PARAGON2 predictions of the radial reaction rates distributions for all fuel types. The consistency of the results, across all fuel types, confirms the accuracy of PARAGON2 UFEML to predict detailed micro reaction rates. [

]^{a,c}

a,b,c

Figure 3-5: U-238 Spatial Distribution of the Resonance Capture in UO₂ Pellet

a,b,c

Figure 3-6: U-238 Spatial Distribution of the Resonance Capture in U-metal Pellet

a,b,c
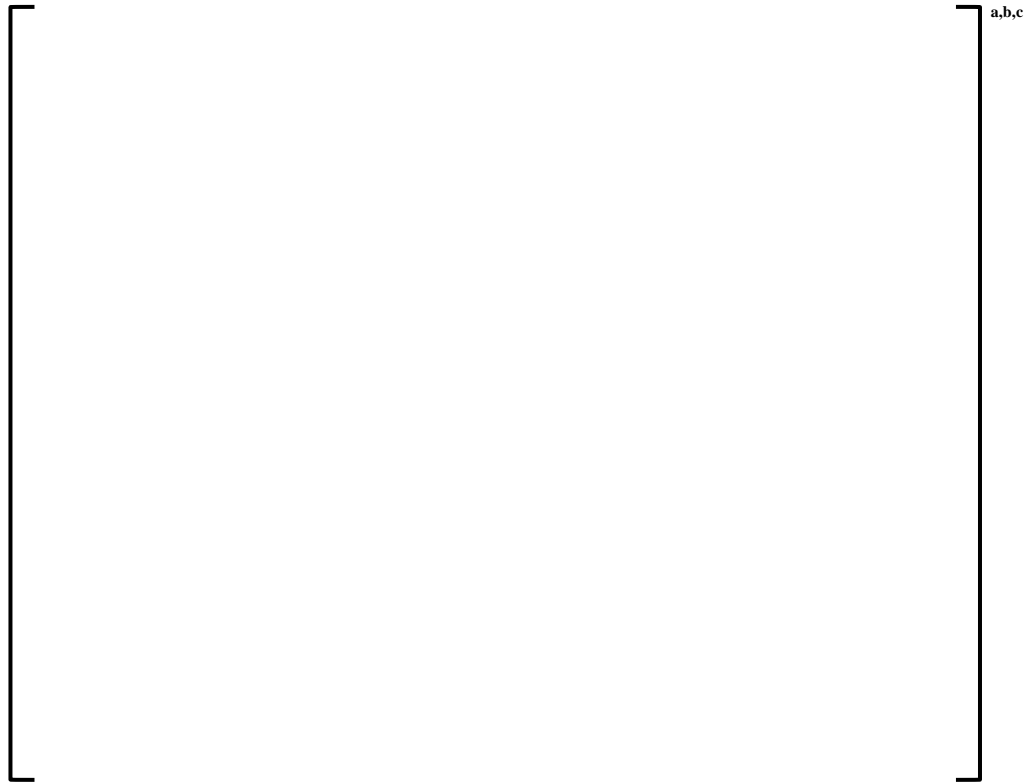
Figure 3-7: U-238 Spatial Distribution of the Resonance Capture in U-Zr Alloy

3.1.1.3   CRIEPI-Experiment: Isotopics and Burnup Radial Distributions

Post Irradiation Examinations Description

To assess PARAGON2 predictions of the radial distributions of the burnup and actinides concentrations (uranium and plutonium isotopes) within the pellet, the PIE experiments, described in Refs. [23] and [49], were considered. The discharge average burnup of the UO_2 sample in this experiment is ~74.5 GWd/t and the burnup of the peripheral region was estimated at about 150 GWd/t.

The same pin cell model used in Ref. [23] is used here to compute the radial distribution of the burnup and isotopic concentrations. However, **[   ]**[a,c] within the pellet, is used to better simulate the profile variations of different parameters. The pin cell was depleted up to the discharge burnup. **[   ]**[a,c]

Results

In Figure 3-8, the spatial burnup distribution obtained with PARAGON2 is compared to PIE measurements reported in Ref. [49]. PARAGON2 predicts accurately the measured burnup including the peak at the pellet periphery. Figure 3-9 and Figure 3-10 show the uranium (U) and the plutonium (Pu) spatial concentrations, respectively, within the pellet. The uranium concentration decreases rapidly in the peripheral region. In response to the decrease in the uranium, the plutonium concentration increases rapidly in the peripheral region. PARAGON2 does predict accurately the profile variations of these actinides.

a,b,c

Figure 3-8: UO₂ Pellet Radial Burnup Distribution

a,b,c

Figure 3-9: Radial Uranium Concentration Distribution in UO₂ Pellet

a,b,c

Figure 3-10: Radial Plutonium Concentration Distribution in UO$_2$ Pellet

3.1.1.4   Strawbridge-Barry Critical Experiments

Description of the experiments

The Strawbridge and Barry critical experiment contains 101 uniform, light water lattices. These experiments contain 40 uranium oxide and 61 uranium metal cold clean experiments (Ref. [54]). These critical experiments have historically been included in Westinghouse code qualifications since they cover a wide range of lattice parameters and therefore provide a severe test for the lattice code to predict reactivities accurately over a broad range of conditions.

Since the Strawbridge-Barry critical experiments are uniform lattices for which experimental bucklings have been reported, these experiments have been treated as single pin cells in PARAGON2. The ranges of lattice parameters covered by these experiments are:

Enrichment (w/o U-235) :   1.04 to 4.069
Boron concentration (ppm):   0 to 3392
Water to uranium ratio: 1.0 to 11.96
Pellet diameter (cm):   0.44 to 2.35
Lattice pitch (cm):   0.95 to 4.95
Clad material: none, aluminum, stainless steel
Lattice type: square, hexagonal
Fuel density (g/cm3):   7.5 to 18.9

Since the current version of PARAGON2 does not model hexagonal fuel, the hexagonal pin cells were replaced by equivalent square pin cells that preserve area of the moderator.

Results

A summary of the results is shown in Table 3-1. This table shows reactivity predictions for various groupings of the experiments. The comparison is done between experimental data (k_{eff} values) and Monte Carlo results (MCNP k_{inf} values). Of interest is the result for all UO$_2$ experiments. The mean k_{eff} for these forty experiments is [   ]^{a,c}. The mean k_{eff} for all experiments was [   ]^{a,c}. As for the comparison with Monte Carlo, the two codes give almost the same results with a mean delta k_{inf} of [
          ]^{a,c}. Figure 3-11 through Figure 3-14 show the PARAGON2 results as a function of water to uranium ratio, enrichment, pellet diameter, experimental buckling, and soluble boron concentration (seven criticals had soluble boron). The results in these figures show excellent performance for PARAGON2 over the entire range of each parameter with no significant bias or trends for any lattice parameter. The comparisons to MCNP (Ref. [58]) show that PARAGON2 is equivalent to continuous energy Monte Carlo solution for all fuel types.

Table 3-1: Strawbridge-Barry Critical Experiment Data vs. PARAGON2 Predictions

a,b,c

a,b,c

Figure 3-11: Strawbridge-Barry Critical Experiment: PARAGON2 Prediction vs. Lattice Water to Uranium Ratio

a,b,c

Figure 3-12: Strawbridge-Barry Critical Experiments: PARAGON2 Prediction vs. Fuel Enrichment

a,b,c

Figure 3-13: Strawbridge-Barry Critical Experiments: PARAGON2 Prediction vs. Pellet Diameter

a,b,c

Figure 3-14: Strawbridge-Barry Critical Experiments: PARAGON2 Prediction vs. Experimental Buckling

3.1.2   Critical Experiments

3.1.2.1   Babcock & Wilcox Spatial Criticals

A large physics verification program sponsored by USAEC and B&W was conducted at B&W's Lynchburg Research Center during the 1970's. These criticals provide reactivity and power distribution measurements for typical PWR lattices at cold conditions for various configurations of fuel rods, guide thimbles, and several different burnable absorbers [28] and [30].

Since PARAGON2 can handle large problems, these criticals were modeled directly in PARAGON2. For each critical, the PARAGON2 k_{inf} was compared to the k_{inf} calculated by the Monte Carlo code MCNP for the same configuration. Both codes use the same basic cross-section library based on ENDF/B-VII for all calculations in this report. In addition, the axial buckling provided in the references was used with the PARAGON2 reactivity result to calculate k_{eff}. Details for each configuration are provided in the references.

Table 3-2 presents the PARAGON2 and MCNP results for B&W Core XI for loadings 1 through 9. Core XI contained low enriched uranium clad in aluminum in a 15x15 lattice. For each of the nine loadings, Table 3-2 shows the number of fuel rods, water rods and Pyrex burnable absorbers, the MCNP calculated k_{inf} and standard deviation, the PARAGON2 calculated k_{inf}, and the PARAGON2 k_{eff} calculated using the axial buckling. The mean PARAGON2 k_{inf} for the nine configurations was [

]^{a,c}, which is within [   ]^{a,c} of the mean MCNP k_{inf} of [

]^{a,c}. The mean PARAGON2 k_{eff} was [   ]^{a,c} . Power distributions for three of these criticals are shown in Figure 3-15 (loading 2), Figure 3-16 (loading 6), and Figure 3-17 (loading 9). The results shown in these figures demonstrate that the predicted PARAGON2 power distribution agrees very well with measurement with the average difference being about [   ]^{a,c}.

Table 3-3, Table 3-4, Table 3-5, and Table 3-6 present PARAGON2 results for B&W cores with gadolinia rods and with and without control rods. Table 3-3 shows results for cores with the number of gadolinia rods, varying from 0 to 36 in 15x15 lattices of 2.46 wt% enriched fuel. Table 3-4 shows results from the same cores in the presence of B_4C control rods. Table 3-5 shows results from cores with varying number of gadolinia rods (0 to 36) with and without control rods in 15x15 lattices of 4.02 wt% enriched fuel. Table 3-6 simulates a CE 16x16 lattice with 2x2 water rods with 4.02 wt% enriched fuel and from 0 to 32 gadolinia rods. As in the B&W Pyrex experiments shown in Table 3-2, MCNP was run for all configurations for k_{inf} comparisons to PARAGON2. The maximum difference between the mean MCNP and PARAGON2 k_{inf} values for these tables is [   ]^{a,c}. The mean PARAGON2 k_{eff} varies from critical by [

]^{a,c}. The standard deviations are all below [   ]^{a,c}.

Comparisons of measured and PARAGON2 predicted power distributions for three of these experiments are provided in Figure 3-18 (Core 5, 28 gadolinia rods), Figure 3-19 (Core 12, no gadolinia rods), and Figure 3-20 (Core 14, 28 gadolinia rods). As with the Pyrex cores, the power distributions of these cores were very well predicted by PARAGON2 with the mean measured to predicted rod power difference being [   ]^{a,c} for all three-core configurations.

The reactivity results for all twenty-nine B&W critical experiments were very good with a mean k_{eff} of [   ]^{a,c}. The average difference between the measured and PARAGON2 power distribution for the six experiments shown in Figure 3-15 through Figure 3-20 was [   ]^{a,c}.

Table 3-2: Results for B&W Core XI with Pyrex Rods

[   ]^{a,b,c}

Table 3-3: Results for B&W Cores with 2.46 wt% U-235 and Gadolinia Rods

[   ]^{a,b,c}

Table 3-4: Results from B&W Cores with 2.46 wt% U-235, Gadolinia Rods, and Control Rods

a,b,c

Table 3-5: Results from B&W Cores with 4.02 wt% U-235, Gadolinia Rods, and Control Rods

a,b,c

Table 3-6: Results from B&W Cores with 4.02 wt% U-235, CE 16x16 Lattice with 2x2 Water Rods

a,b,c

Figure 3-15: B&W Critical Experiments: Core XI, Loading 2 Center Assembly Rod Power Distribution

Figure 3-16: B&W Critical Experiments: Core XI, Loading 6 Center Assembly Rod Power Distribution

Figure 3-17: B&W Critical Experiments: Core XI, Loading 9 Center Assembly Rod Power Distribution

Figure 3-18: B&W Critical Experiments: Core 5, 28 Gadolinia Rods Center Assembly Rod Power Distribution
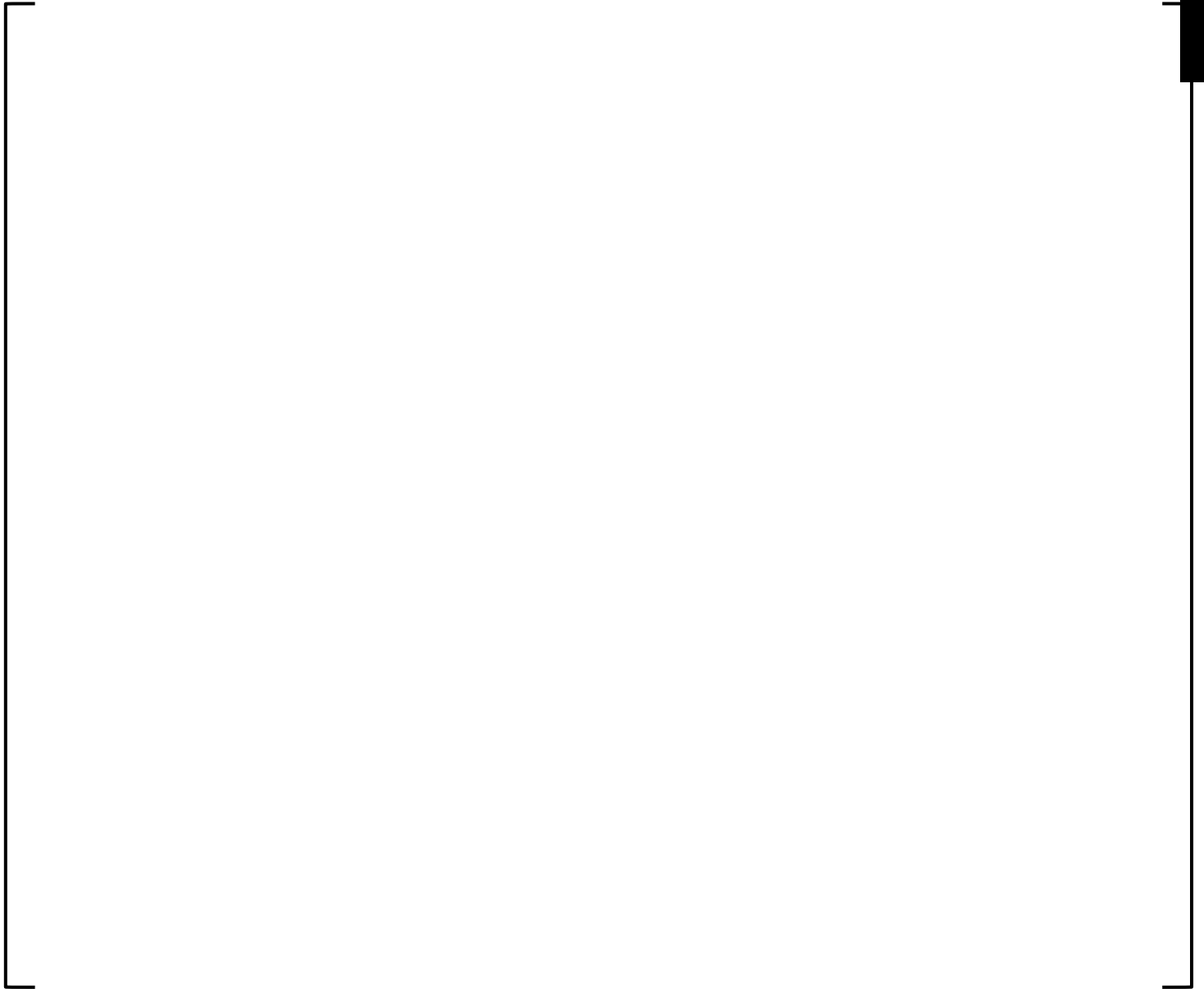
Figure 3-19: B&W Critical Experiments: Core 12, No Gadolinia Rods Center Assembly Rod Power Distribution

Figure 3-20: B&W Critical Experiments: Core 14, 28 Gadolinia Rods Center Assembly Rod Power Distribution

3.1.2.2 KRITZ High-Temperature Critical Experiments

The KRITZ high-temperature critical experiments series (Ref. [47]) provide critical benchmark data for uranium-fueled, water moderated lattices at high temperatures. These experiments were run at temperatures up to 519 K covering temperatures close to the range used in light water reactor cores. The details of the experiments are provided in Ref. [47]. Twelve KRITZ experiments were modeled in PARAGON2. The modeled experiments included two lattice configurations (39x39 and 46x46) over a temperature range from 314.4 to 519.0 K with boron concentrations from essentially zero to 175 ppm. The axial bucklings provided in the reference were used to calculate k_{eff}. Table 3-7 summarizes the results of the PARAGON2 calculations for these critical experiments. For each experiment, the table shows the lattice configuration, the soluble boron concentration, the water temperature, the axial buckling used to determine k_{eff}, and the PARAGON2 calculated k_{eff}. The mean k_{eff} for all twelve experiments was **[**

][a,c]. The very small standard deviation shows that PARAGON2 predicts very consistently across the large temperature range of these experiments within the accepted deviations. MCNP was run for all configurations for k_{inf} comparisons to PARAGON2. The average difference between the mean MCNP and PARAGON2 k_{inf} values for these critical experiments is **[** **]**[a,c].

Table 3-7: PARAGON2 Results for KRITZ Experiments

[a,b,c]

3.1.2.3   MOX Critical Experiments

3.1.2.3.1   KRITZ-2 Experiment

The KRITZ data also contains an experiment with MOX fuel: KRITZ-2:19. The objective of the KRITZ-2:19 experiment was to attain criticality of a rectangular array of mixed oxide Zircaloy-2-clad fuel rods in light water by regulating the concentration of boron in the water and by adjusting the water level. Criticality was achieved at isothermal conditions at room temperature (294.3 K) (cold experiment) and at elevated temperature (509.1 K) (hot experiment). The configuration of these experiments is an array of 25x24 rods with a pitch of 1.81 cm. The fuel used was composed of 0.16 wt% U-235 uranium enriched and 1.5 wt% PuO_2 of total plutonium. The plutonium composition vector and other details of these experiments are obtained from Refs. [52] and [53].

The cold and hot experiments were modeled in PARAGON2 using the full radial 2D experimental configurations. An equivalent 2D MCNP model was also developed for reactivity comparison. The absolute differences in k_{inf} between the two codes are **[   ]**[a,c] for respectively cold and hot experiments. Figure 3-21 shows fission reaction rates comparison between the measurement and PARAGON2 predictions for both hot and cold cases. The standard deviations of these differences are **[   ]**[a,c] for cold and hot experiments, respectively. These differences are within the maximum 2σ errors of the experiments (1σ is estimated to be **[   ]**[a,c]). The large differences in Figure 3-21 are obtained at peripheral pins where the power is low. **[**

][a,c]

[a,b,c]
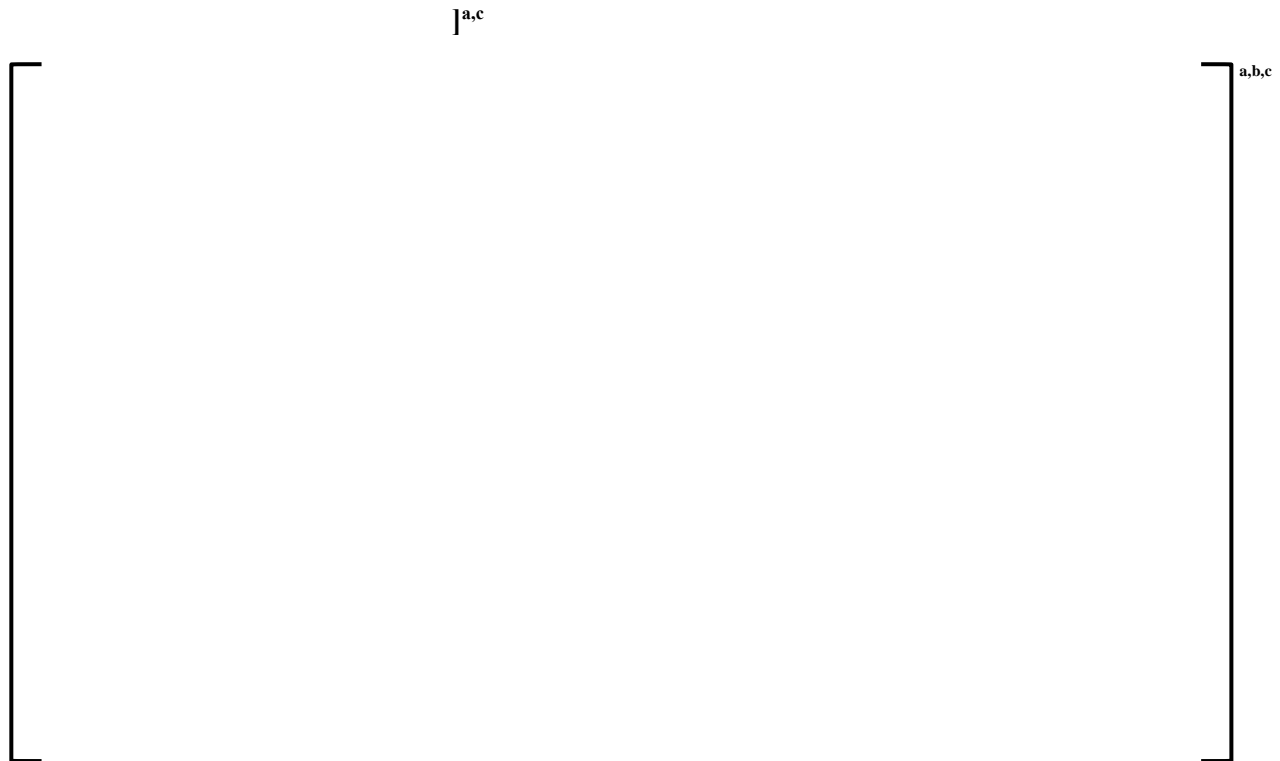
Figure 3-21: KRITZ 2:19 Critical Experiment: Relative Fission Rate Differences of Measurement and PARAGON2

3.1.2.3.2 VENUS-2 Critical Experiment

The VENUS critical facility is a PWR mock-up "zero power" critical reactor located at SCK-CEN in Belgium (Ref. [25]). The central part of the VENUS-2 MOX core consists of UO_2 fuel pins with MOX fuel pins loaded on the periphery of the core. The VENUS-2 core consists of twelve "15x15" subassemblies with a pitch of 1.26 cm and a full core height of 50 cm. Each of the four central assemblies contains 3.3 wt% U-235 enriched UO_2 fuel pins and 10 Pyrex pins. The 8 peripheral assemblies contain both UO_2 and MOX fuel, with the 7 internal rows containing 4.0 wt% U-235 enriched UO_2 and the 8 external pins containing MOX fuel (UO_2-PuO_2) enriched with 2.0 wt% in U-235 and 2.7 wt% in high-grade plutonium with the major plutonium isotopes. The VENUS-2 experimental data contain fission rates for 121 of the 325 fuel rods in 1/8th of the core. These 121 pins consist of 41 pins with 3.3 wt% UO_2, 35 pins with 4.0 wt%, and 45 pins with 2.0/2.7 wt% MOX.

VENUS-2 two-dimensional full core was modeled directly in PARAGON2. The PARAGON2 k_{inf} was compared to the k_{inf} calculated by the Monte Carlo code MCNP for the same configuration. In addition, the axial buckling provided in the references was used with the PARAGON2 reactivity result to calculate k_{eff}. Details of the experiment are provided in Ref. [25].

The PARAGON2 k_{eff} obtained is [   ]^{a,c}, which is in a good agreement with the experiment. PARAGON2 k_{inf} is close to MCNP value. The difference in k_{inf} between MCNP and PARAGON2 is [   ]^{a,c}. [

]^{a,c}

Figure 3-22 shows the pin fission reaction rates distribution in 1/8th of the core. Table 3-8 summarizes the relative differences between measured (M) and PARAGON2 (P) computed fission reaction rates, (M/P-1) (%), for the full core and different fuel assembly types. Table 3-8 shows also the comparison for the whole core and for the measured locations (pins) only. The non-measured values (204 pins) in the whole core were obtained by interpolations (Ref. [25]). The uncertainty of the measured data is [   ]^{a,c} in UO_2 and [   ]^{a,c} in MOX pins. The standard deviation for individual fuel assembly types is small and within a maximum of [   ]^{a,c} (especially if only measured locations are considered). The standard deviation for the whole core is slightly larger and the maximum absolute error is within [   ]^{a,c} (or [   ]^{a,c} for measured pins only). The standard deviations of all the differences are within 1σ or 2σ of the measurement uncertainties. [   ]^{a,c}

In Table 3-8, the averages of the differences for individual assemblies show an over-prediction of MOX rods (periphery) and an under-prediction in the UO_2 rods (a slight tilt). This trend is also clearly visible in Figure 3-22, where M-P is using global normalization. This same trend in predictions is also observed in the aggregate simulation results obtained by different codes and libraries presented in Ref. [25]. Overall PARAGON2 results are very similar to other deterministic and Monte Carlo codes results described in Refs. [1] and [25] especially the codes using same cross-sections library ENDF/B-VII. The average deviation in Table 3-8 corresponds to the average deviation about the mean.

Table 3-8: VENUS-2 Experiment: Results of Fission Reaction Rates between Measurement and PARAGON2
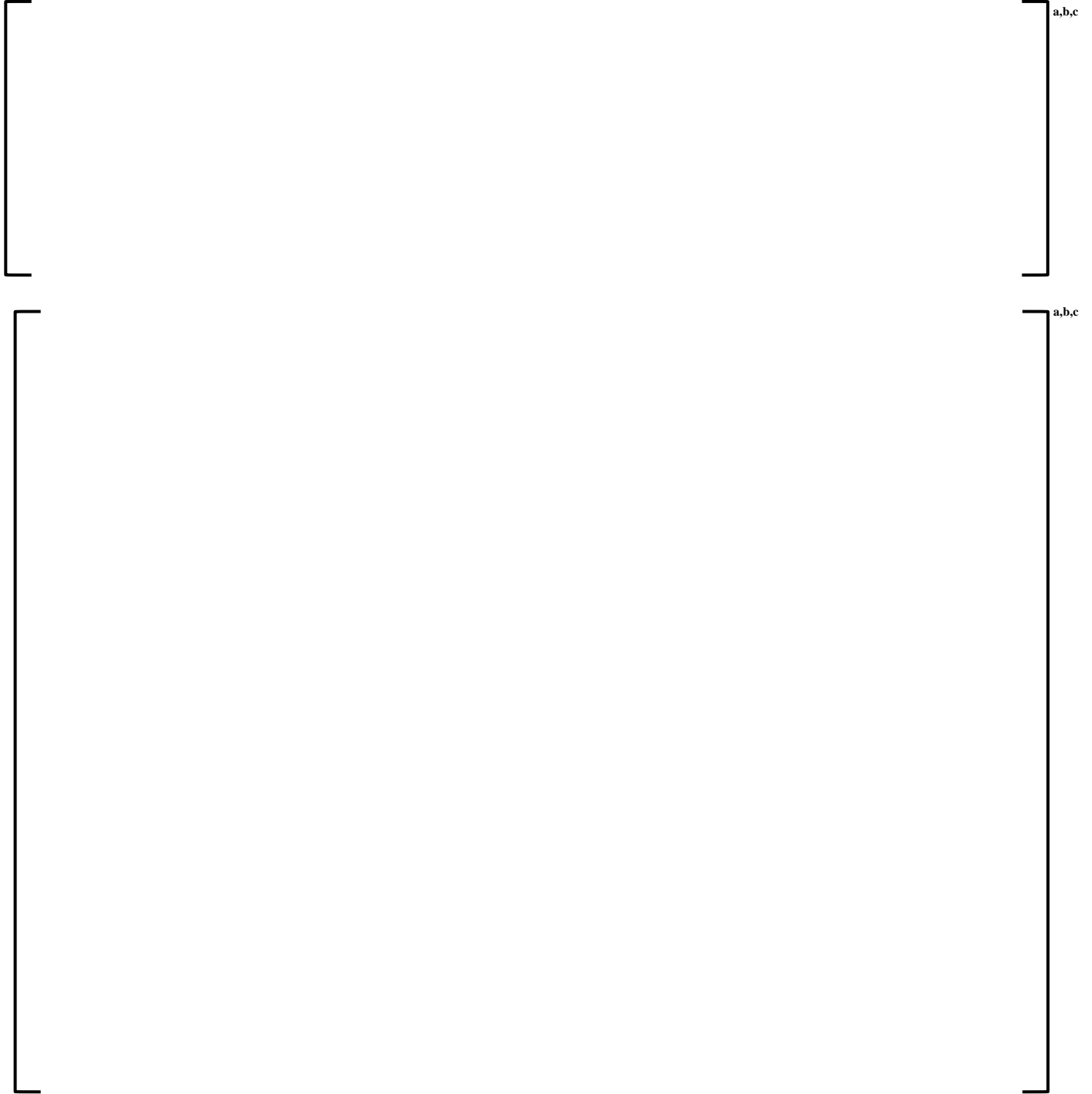
a,b,c

a,b,c

Figure 3-22: VENUS-2 Experiment: Fission Reaction Rate Difference between Measurement and PARAGON2

3.1.2.4   NCA Critical Experiments

Toshiba NCA [3] is a tank type light water moderated nuclear facility that is operated at room temperature and at atmospheric pressure. Water is normally filled in the core tank at the room temperature. The level of the water is adjusted to achieve the criticality of the core. There are two main regions in the core of the tank: a driver region which is normally built with fuel rods with 2 wt% enrichment and a test region (where measurement is done) which is configured according to the experiments needs. The details of the facility are given in Ref. [3].

Five configurations (Core-1 to Core-5) were designed to mimic current commercial cores in operation. For all the experiments, the rods are arranged in a square geometry with a pitch of 1.52 cm. All the fuel pellets used have a radius of 0.50 cm. The cladding for the fuel rods is made of Aluminum with an external radius of 0.59 cm and a thickness of 0.08 cm. The uranium enrichment used in these experiments ranges between 2 wt% and 4.9 wt%. Tungsten rods and gadolinium burnable absorber rods were also used. Core-4 and Core-5 simulates the hot full power PWR operating conditions by using 1000 ppm of boron and polystyrene blocks. Figure 3-23 shows, in details, the layout of different cores. Full descriptions of these experiments are provided in Refs. [42] and [57].

It is important to note that the fission rates have been measured multiple times to reduce the measurement uncertainties. It was found that the (delta) standard deviation of the repeatability of the measurements is [   ]^{a,c}, which is taken as the uncertainty on the measured fission rate values. In addition, for reactivity measurement (critical mass), the repeatability of water height is within $\sim\pm4$mm. Therefore, the uncertainty is roughly estimated to be within [   ]^{a,c}.

All five experiments were modeled using PARAGON2 and MCNP codes. Both 3D and 2D MCNP models were considered. The 3D results were used to confirm the accuracy of the cross-section data and as a benchmark of the experiment. These results are described in Refs. [42] and [57]. In Table 3-9, PARAGON2 predictions are compared to the equivalent 2D MCNP. Ref. [42] describes in detail these simulations. The results show good reactivity agreement between continuous energy Monte Carlo and PARAGON2. All the tungsten rodded cases (Core-1, Core-2, and Core-3) seem to be well predicted. [

]^{a,c}

For pin power distribution, the comparison of PARAGON2 fission rates predictions to the experimental data is displayed case-by-case in Figure 3-24. For all the cores, all the differences are below two-standard deviations of the experimental errors (2σ). [
                    ]^{a,c} The Root Mean Square (RMS) of the differences ranges from [   ]^{a,c} (Core-1) to [   ]^{a,c} (Core-3) indicating an overall good fission rates prediction of PARAGON2 calculations. Detailed statistical comparisons are reported in Ref. [42], where it was concluded that all the statistical tests indicate that overall PARAGON2 results are very similar to measured data. It is important to point out that the location of the maximum power is well predicted by PARAGON2 in all cases.

Table 3-9: NCA Experiments: Reactivity Differences between 2D MCNP and PARAGON2

a,b,c
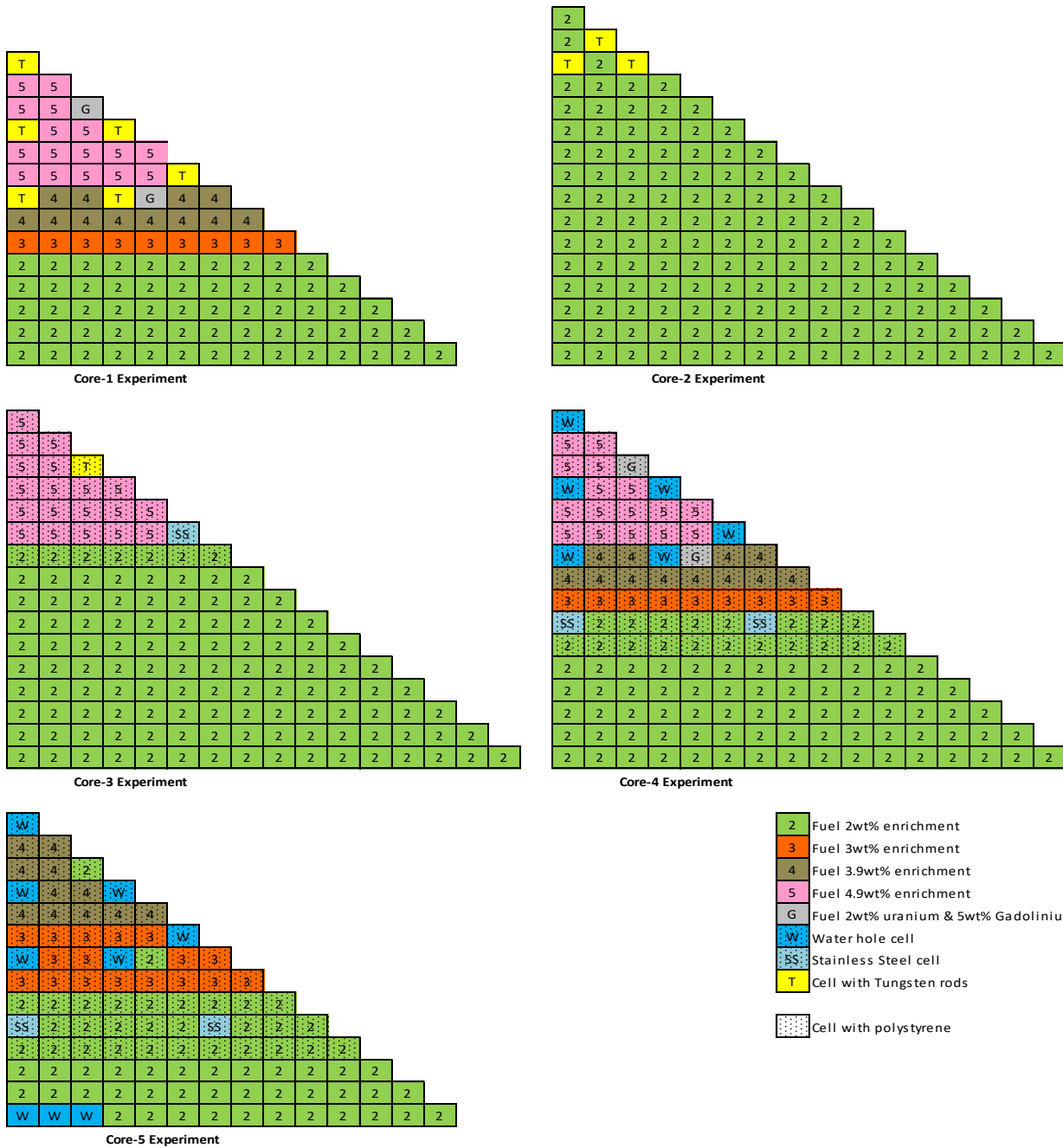
Figure 3-23: NCA Experiments: Core Configurations

Figure 3-24: NCA Experiments: Comparison of Measured vs. PARAGON2 Predicted Pin Fission Rates

3.1.2.5   Critical Experiments with Erbia-Urania Fuel

In 1991, CE performed a series of critical experiments at the RPI RCF in order to measure and compare predicted values of different parameters, including local power distributions of importance herein for lattice configurations similar to a standard 16x16 CE fuel design, but with Erbia-Urania fuel. At the center of the experimental cores was a 16x16 array of CE fuel, surrounded by a fixed driver region of SPERT (Special Power Excursion Reactor Test) fuel and by a large water reflector. While the driver geometry remained fixed, the number of Erbia pins in the central 16x16 array was varied to accommodate a range of erbium loadings, where the cores are identified by the number of Erbia pins and the total number of all pins: 00/468, 20/468, 44/468, 56/468. The CE fuel was of pitch 1.29 cm and consisted of UO_2 fuel rods enriched to 3.65 wt% and UO_2-Er_2O_3 fuel rods of 1.5 wt% Erbia which slightly displaced some of the urania. The SPERT fuel was of pitch 1.71 cm and consisted of UO_2 enriched to 4.8 wt% and clad in 304 stainless steel (SS). Refs. [10] and [26] provide further detail on the experimental configurations.

The four experiments were modeled as a full 2D quarter core in PARAGON2. The central region with CE fuel is represented exactly as described in Ref. [26], **[**

]^{a,c}

An equivalent 2D MCNP model was created to benchmark PARAGON2 reactivity. The maximum absolute difference in k_{inf} between MCNP and PARAGON2 results is **[   ]^{a,c}** (obtained for 44/468 case). This difference is within the delta range seen in other critical experiments (Monte Carlo runs have 1σ standard deviation of **[   ]^{a,c}**).

The main purpose of this benchmark is to compare the PARAGON2 predicted pin power distribution against the measurements. Figure 3-25 through Figure 3-28 show the measured minus predicted differences in percent relative to prediction [(Measured – Predicted)/Predicted] for all four configurations. The root mean square for all these cores varies between **[   ]^{a,c}** and is within the measurements uncertainty. The absolute maximum differences vary between **[   ]^{a,c}**. The largest difference is seen in case 20/468 and it occurs at the center of the core. Similar differences and trends were also obtained with the licensed code used in Ref. [26], including for the case 20/468.

The differences obtained for measured pin power distribution and for reactivity comparison against Monte Carlo show that PARAGON2 can accurately predict the fuel with Erbium burnable absorbers.

a,b,c

Figure 3-25: CE-RPI Experiments: Power Distribution Comparison for Core 00/468

a,b,c

Figure 3-26: CE-RPI Experiments: Power Distribution Comparison for Core 20/468

a,b,c

Figure 3-27: CE-RPI Experiments: Power Distribution Comparison for Core 44/468

a,b,c

Figure 3-28: CE-RPI Experiments: Power Distribution Comparison for Core 56/468

a,c

a,c

a,b,c

3.2   ISOTOPICS DATA

The depletion capability of PARAGON2 will be assessed in this section by modeling several PIE benchmarks. Benchmarks were selected based on several criteria:

1. Coverage of a wide range of burnup,
2. coverage of multiple fuel lattice and reactor designs,
3. coverage of a wide range of enrichment,
4. samples with more detailed experimental data (not only a single or few isotopes), and
5. available input data for ease of modeling.

PIE benchmarks chosen for this work contain isotopic concentration data for samples from small segments of fuel rods in assemblies from past operation at the Gösgen-1, TMI-1, Calvert Cliffs-1, Turkey Point-3, and Vandellos-2 plants. These rods are at various enrichments, measured burnup, are from various fuel lattice designs and have undergone different exposure conditions (burnable absorbers, etc.). Table 3-10 summarizes the features of the selected benchmarks.

Table 3-10: Summary of Sample Characteristics

Plant	Sample	U-235 Enrichment (wt%)	Discharge Burnup (GWD/MTU)	Lattice Type
Gösgen-1	GU1	3.500	59.66	15x15
TMI-1	A1	4.010	45.90	15x15
	B1		55.00	
	C2D1		53.50	
	C2D2		52.70	
Calvert Cliffs	CC	3.038	37.12	14x14
	LL		27.35	
	P		44.34	
Turkey Point	4	2.556	30.50	15x15
Vandellos	E58-88	4.500	43.50	17x17
	E58-263		63.01	
	E58-773		74.57	

Most input for this work comes from the Spent Fuel Isotopic Composition (SFCOMPO 2.0) relational database used to facilitate the search and visualization of experimental assay data of spent nuclear fuel (Refs. [8] and [27]). Each of the samples taken contains different levels of detail regarding operational characteristics for the assembly containing the chosen fuel rods. Therefore, modeling of each sample is described and derivation of the needed input parameters discussed are on a plant by plant basis and the assembly/assemblies and sample data are described likewise.

Within the data for an individual sample, multiple experimental dates are present such that different isotopes are evaluated on different days. Multiple decay calculations are then performed at different decay times and isotopics extracted from the associated decay calculation corresponding with the proper decay time for each isotope determined.

The modeling of each benchmark was set up to approximate the core operating history for each isotopic data set.

The detailed descriptions of the selected benchmarks are openly available in SFCOMPO 2.0 database and will not be repeated in this report (available online at the time of writing this report).

3.2.1   Gösgen-1 Modeling

The Gösgen nuclear power plant is a single unit PWR power plant of KWU design located in Switzerland. SFCOMPO 2.0 contains sample PIE data for rods exposed in three different assemblies. The assemblies were modeled as 3-Loop 15x15 design types.

Assembly 1240 contains one sample (Rod 14H13, Sample GU1) exposed in Cycles 12, 13, 14 and 15. Isotopic content is available for a significant number of isotopes, and as a result, a model is set up for this sample. Note, however, that fuel rods around the sample were replaced in Cycles 14 and 15. This was not incorporated into the modeling and therefore the modeling could be improved. The axial height on the fuel rod of sample GU1 is 960.5 mm from the fuel bottom (of the active length). The planar pin arrangement of this assembly design is shown in Figure 3-32.

First, the fuel and moderator temperatures of the core (and sample height) are modeled as close as possible using the data available in SFCOMPO 2.0 database. Loading is derived from the given density, fuel pellet outer diameter and the total number of fuel rods in the core. The value is derived assuming all fuel is 3.5 wt% U-235 (the sample enrichment).

Relative power was derived from the given sample and core burnup for each cycle. Data is available for total sample burnup and cycle burnup whose ratio provides the relative power, which would give conditions similar to what the sample experienced.
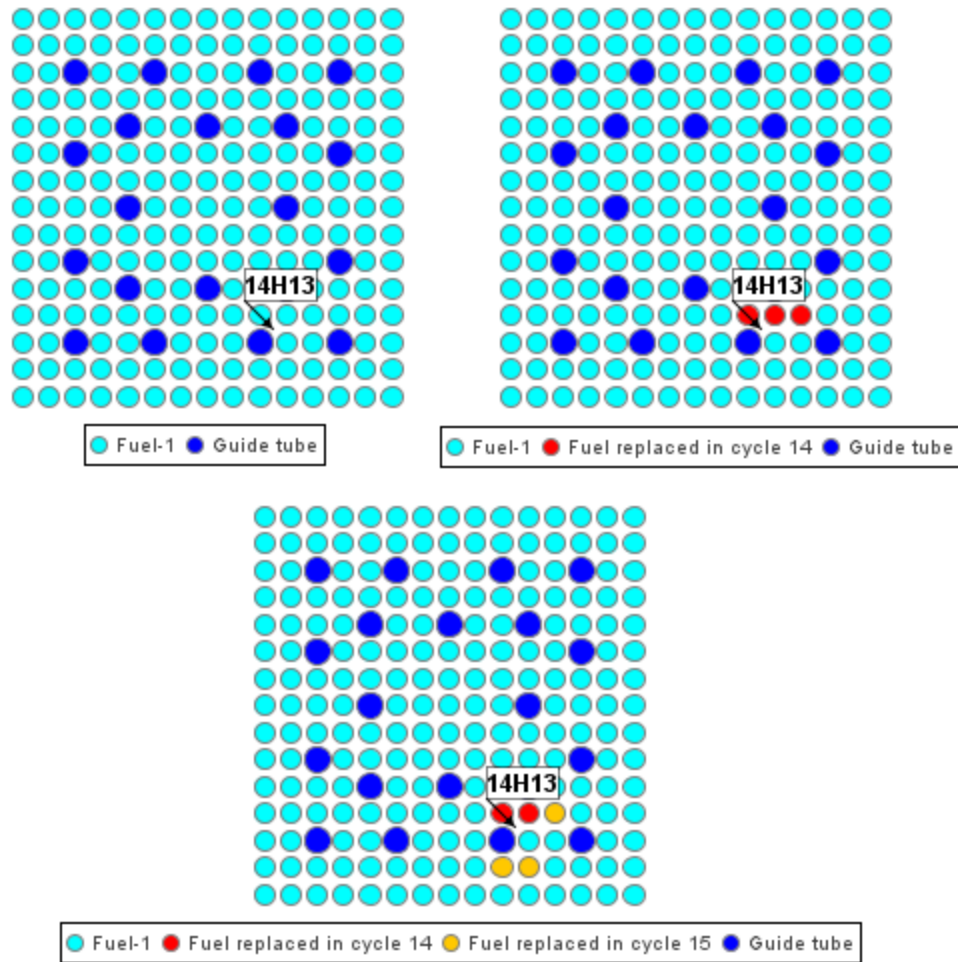
Figure 3-32: Planar Pin Arrangements for Assembly 1240 for Cycles 12-13 (upper left), Cycle 14 (upper right), and Cycle 15 (bottom)

3.2.2   TMI-1 Modeling

The Three Mile Island (TMI) Nuclear Generating Station is currently a single unit station. It is a B&W design with the general characteristics given in SFCOMPO 2.0 database. SFCOMPO 2.0 (Refs. [8] and [27]) contains sample PIE data for rods exposed in two different assemblies.

Assembly NJ05YU contains data for two rods with many samples. Rod D5 contains Sample A1, B1, and B2. Note that sample B2 is on the level of a spacer grid and it was shown in Ref. [7] that due to the details of the spacer grid not being available, modeling in this area suffers in accuracy. As a result, models for samples A1 and B1 are developed.

Additionally, data for 13 samples along Rod H6 are available, however, at this time, only two were chosen for modeling. These two, samples C2D1 and C2D2, contain full sample specific power in Watts/g(initial U). Assembly burnup information is not available. Other samples contain the sample burnup that can be used as a scaling factor from the derived burnups for samples C2D1 or C2D2 specific power data. The pin arrangement of assembly NJ05YU is given in Figure 3-33. The axial height locations of the samples, from the rod bottoms (active length) are 2,670 mm and 3,421 mm for samples A1 and B1

respectively of Rod D5, and 1,972 mm and 2,332 mm for samples C2D1 and C2D2 respectively for Rod H6.

To generate a more accurate representation of the B&W lattice, the model input used in the code system was similar to the lattice used in Gösgen. Figure input is required for both cycles, first to insert Burnable Poison Rods (BPRs) and then to pull them out for Cycle 10 and retain the proper lattice. Core loading is calculated as with the Gösgen models and is very close (**[   ]ᵃ,ᶜ**) to the SFCOMPO 2.0 listed 82.5 MTU. This is used then to derive a core Watts/g assuming full power operation. Step burnups were derived from the given specific power as a function of elapsed time.

Moderator temperature was set by converting moderator density given in SFCOMPO 2.0 to moderator temperature at constant pressure.
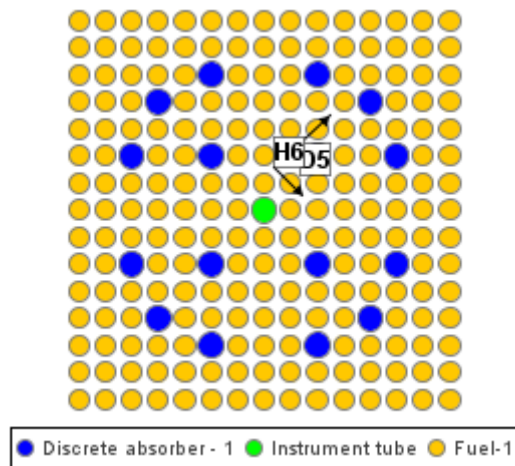
Figure 3-33: Planar Pin Arrangement for Assembly NJ05YU from Cycles 9 and 10

3.2.3   Calvert Cliffs-1 Modeling

The Calvert Cliffs Nuclear Power Plant is a 2-unit plant. Unit 1, from which PIE data is available, is a 2-loop CE design with the general characteristics given in SFCOMPO 2.0 database. SFCOMPO 2.0 (Refs. [8] and [27]) contains sample PIE data for rods exposed in three different assemblies.

Assembly D047 contains one rod (Rod MKP 109) with multiple samples available with PIE data. This is a single enrichment zone assembly. Only three samples contain data for multiple isotopes. As a result, models for these three samples (CC, LL, and P) are developed. The planar pin arrangement for this assembly and rod location can be seen in Figure 3-34.

Sample axial heights from the rod bottom are 123.2 mm, 270.3 mm, and 1,637 mm, respectively for samples LL, CC, and P of Assembly D047.

Moderator temperature input was determined by assuming a linear heat rise from the given inlet and outlet temperatures since local conditions are desired (meaning moderator temperature should correspond to the sample temperature). Loading was input as 82.5 MTU from SFCOMPO 2.0. The only power data available is for the entire rods that underwent PIE examination.

Rod burnup was determined from the given kW/m as a function of elapsed days (histogram). This was done using the core height, fuel density and loading for a rod, and determining rod burnup from this data. A rod burnup histogram is obtained. The final rod burnup is then compared to the sample burnup, and the ratio used to adjust the rod burnup to scale the burnup for each sample. Then, soluble boron is given as a pointwise function of elapsed days. The elapsed days do not always coincide with the power histogram data and data was linearly interpolated to define all points on the boron letdown curve as a function of burnup.
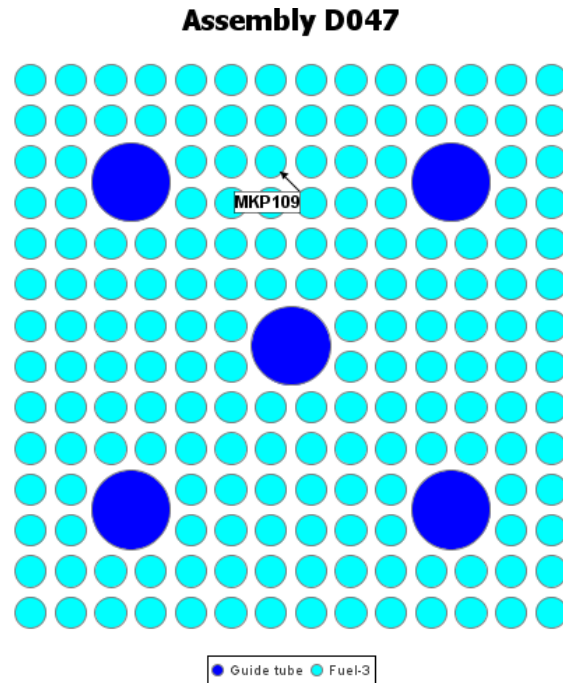
Assembly D047

Figure 3-34: Planar Pin Arrangement of Assembly D047 for Cycles 2, 3, 4, and 5

3.2.4 Turkey Point-3 Modeling

The Turkey Point Unit 3 nuclear power plant is a PWR power plant of Westinghouse design located in the United States with general characteristics given in SFCOMPO 2.0 database. SFCOMPO 2.0 contains sample PIE data for rods exposed in three different assemblies. All samples have the same enrichment with varying burnups. Only one sample was chosen for analysis in this report.

Assembly D01 contains one sample (Rod G10, Sample 4) exposed in Cycles 2, 3, and 4. The axial height on the fuel rod of sample 4 is 65.5 in. The planar pin arrangement of this assembly design is shown in Figure 3-35.

Since Turkey Point is a standard Westinghouse plant, the default input data were used (15x15 3-Loop plant). Updates to the default were made as necessary to match SFCOMPO 2.0 database.

Soluble boron data is given as a constant 450 ppm for each cycle. Relative power was calculated by comparing the reactor and sample power. The reactor thermal power was provided by SFCOMPO as 2,192 MW. The uranium loading was calculated manually and this was used to calculate the assembly power in MW/MTU. This could then be compared to the sample power given by SFCOMPO. The sample's

cycle burnups were not provided and were calculated by multiplying the cycles elapsed days by the sample power.
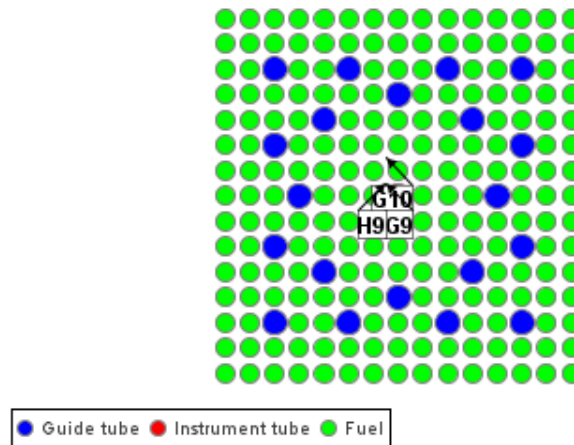
Figure 3-35: Planar Pin Arrangement for Assembly D01

3.2.5   Vandellos Modeling

The Vandellos Unit 2 nuclear power plant is a PWR power plant of Westinghouse design located in Spain with general characteristics given in SFCOMPO 2.0 database. SFCOMPO 2.0 contains sample PIE data for rods exposed in three different assemblies.

Rod WZR0058 contains samples exposed in Cycles 7-11 with varying burnups. Three were chosen E58-88, E58-263, and E58-773 that are at axial positions of 88 mm, 263 mm, and 773 mm from the bottom of the fuel stack, respectively. Isotopic content is available for a significant number of isotopes, and as a result, a model is set up for these samples. Rod WZR0058 was located in Assembly EC45 for Cycles 7-10 and then moved to EF05 for Cycle 11. Assembly EC45 was made up of entirely 4.5 wt% fuel, while all but three rods were 4.24 wt% in Cycle 11. The planar pin arrangements of these assemblies are shown in Figure 3-36 and Figure 3-37. The sample was modeled as if it stayed in EC45 for all cycles. The samples spent most of its time in EC45. Additionally, when moved to EF05 although this assembly has a lower enrichment, it also had a lower assembly burnup. Therefore, this is an acceptable approximation for the purposes of this report. More information can be found in Ref. [6].

Input data for modeling was chosen as a 3-loop, Category 2 plant, which will use the Westinghouse 17x17 3-loop default data for this type of plant. Direct input is used to override the default data as needed to match the values in SFCOMPO 2.0 database. Soluble boron data is given pointwise as a function of elapsed days; however, sample burnup is given as a function of the elapsed days. Therefore, detailed point-wise data is given for soluble boron letdown. Relative power was derived by comparing the sample power (MW/MTU) to the overall core thermal power (MW/MTU). Local moderator temperature was given for each cycle and was input to the code.
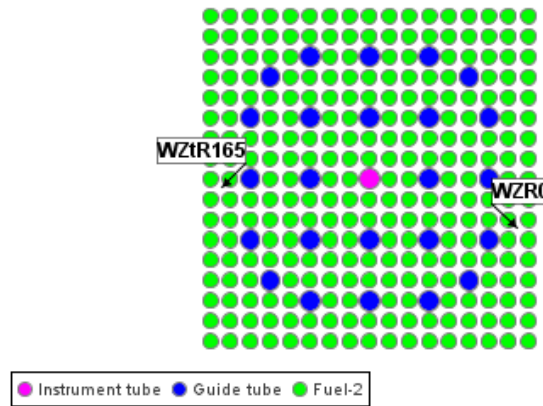
Figure 3-36: Planar Pin Arrangement for Assembly EC45
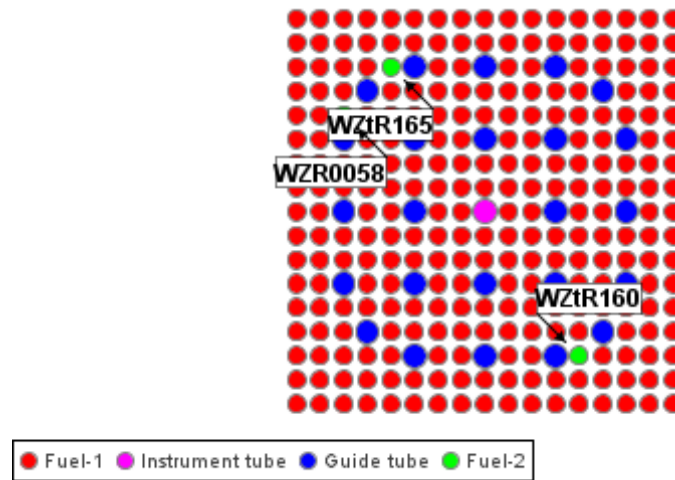
Figure 3-37: Planar Pin Arrangement for Assembly EF05

3.2.6   Evaluations and Analyses

The final pin burnups in PARAGON2 were iterated on until the values were considered to be sufficiently close to the sample burnups. Comparisons of the PARAGON2 predictions and the measured data from the SFCOMPO database were performed using the following formula:

$$C/E - 1, \% = \left(\frac{PARAGON2\ Value}{Experimental\ Value} - 1\right) * 100$$

Figure 3-38 through Figure 3-49 show PARAGON2 predictions compared to measurements for all the samples described in the previous sections. Each figure has actinides and fission products comparisons. Individually some isotopes may show large differences, but there is nothing that is unusual for this type of analyses. Within the same sample, variations in measurement are broad. The uncertainties reported for measurement could exceed [   ]ᵃ,ᶜ. The basic cross-section and numerical solution uncertainties are also contributing to these discrepancies. All the calculations of

these samples were done using 2D assemblies with infinite boundary conditions, which in itself is a significant approximation that could lead to large differences, despite the fact that local conditions seen by the sample were modeled as accurately as possible. Overall, for actinides the average relative differences (values in Figure 3-38 through Figure 3-49) are [   ]^{a,c}. For fission products, the corresponding values are [

        ]^{a,c}. These results are acceptable and fall within the usual discrepancies seen in this type of comparison. Therefore, the depletion module of PARAGON2 produces the expected accuracy results.

3.2.7   Saxton and Yankee Isotopics Data

The spectrograph-measured isotopics data for Saxton Cores 2 and 3 with mixed oxide fuel, Yankee cores 1, 2, and 4 with stainless steel clad fuel, and Yankee Core 5 with zircaloy clad fuel have been compared to PARAGON2 isotopic concentrations. The measured data for these isotopics used in Ref. [41] are documented in Refs. [4], [9], [33], and [50] for Saxton and [24] and [32] for Yankee. Since the measured fuel rods for both the Saxton and Yankee cases were far enough away from lattice heterogeneities that they were exposed to the asymptotic flux spectrum, PARAGON2 pin cell calculations were used for these comparisons. The pin cell cases were set up to approximate the core operating history for each isotopic data set.

The Saxton Cores 2 and 3 isotopic comparisons for the major isotopes are shown in Figure 3-50 through Figure 3-62. Comparisons for the Yankee Cores 1, 2, and 4 stainless steel clad UO_2 fuel isotopics are shown in Figure 3-63 through Figure 3-75. Comparisons for Yankee Core 5 zircaloy clad UO_2 fuel isotopics are shown in Figure 3-76 through Figure 3-88.

As noted in Ref. [41], the Saxton isotopic case was particularly challenging since it is for a mixture of PuO_2 in a natural uranium matrix. In addition, the wet fraction was changed at an intermediate burnup due to the removal of fuel rods for isotopics measurements. As seen in the figures, PARAGON2 matches the measured values in both shape and magnitude.

The Yankee core data represent a typical UO_2 light water lattice with two clad materials. The figures comparing measured to PARAGON2 isotopics for these data also show very good agreement throughout the isotopic burnup range.

The isotopic comparisons for both the Saxton and Yankee isotopics show no significant trend for any isotope with burnup. These excellent results demonstrate the capability of PARAGON2 for predicting the depletion characteristics of both UO_2 and PuO_2 LWR fuel over a wide range of burnup conditions.

a,b,c
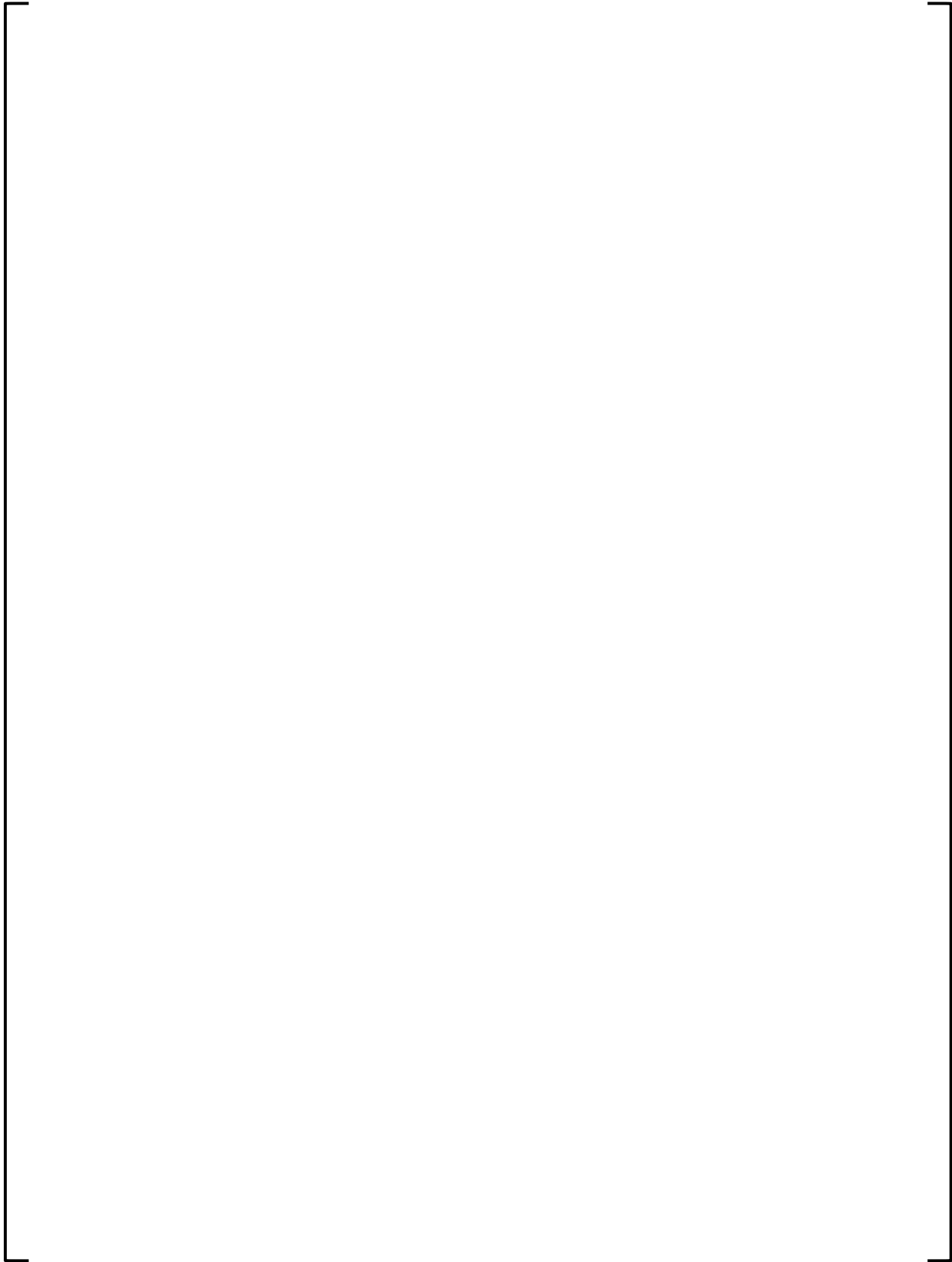
Figure 3-38: PARAGON2 vs. Measured Isotopics for Rod 14H13, Sample GUI of Gösgen-1

a,b,c
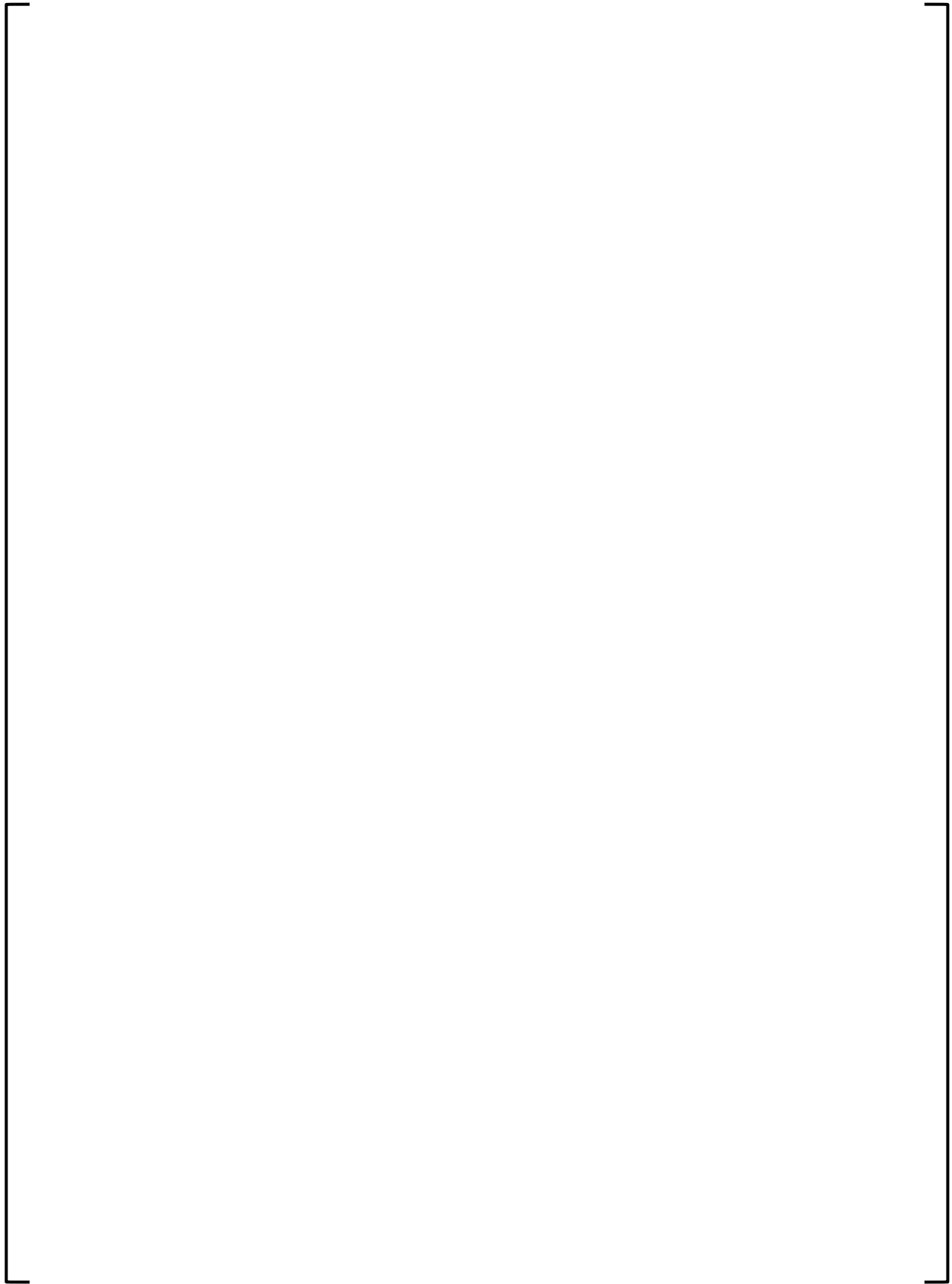
Figure 3-39: PARAGON2 vs. Measured Isotopics for Rod D5, Sample A1 of TMI-1

a,b,c
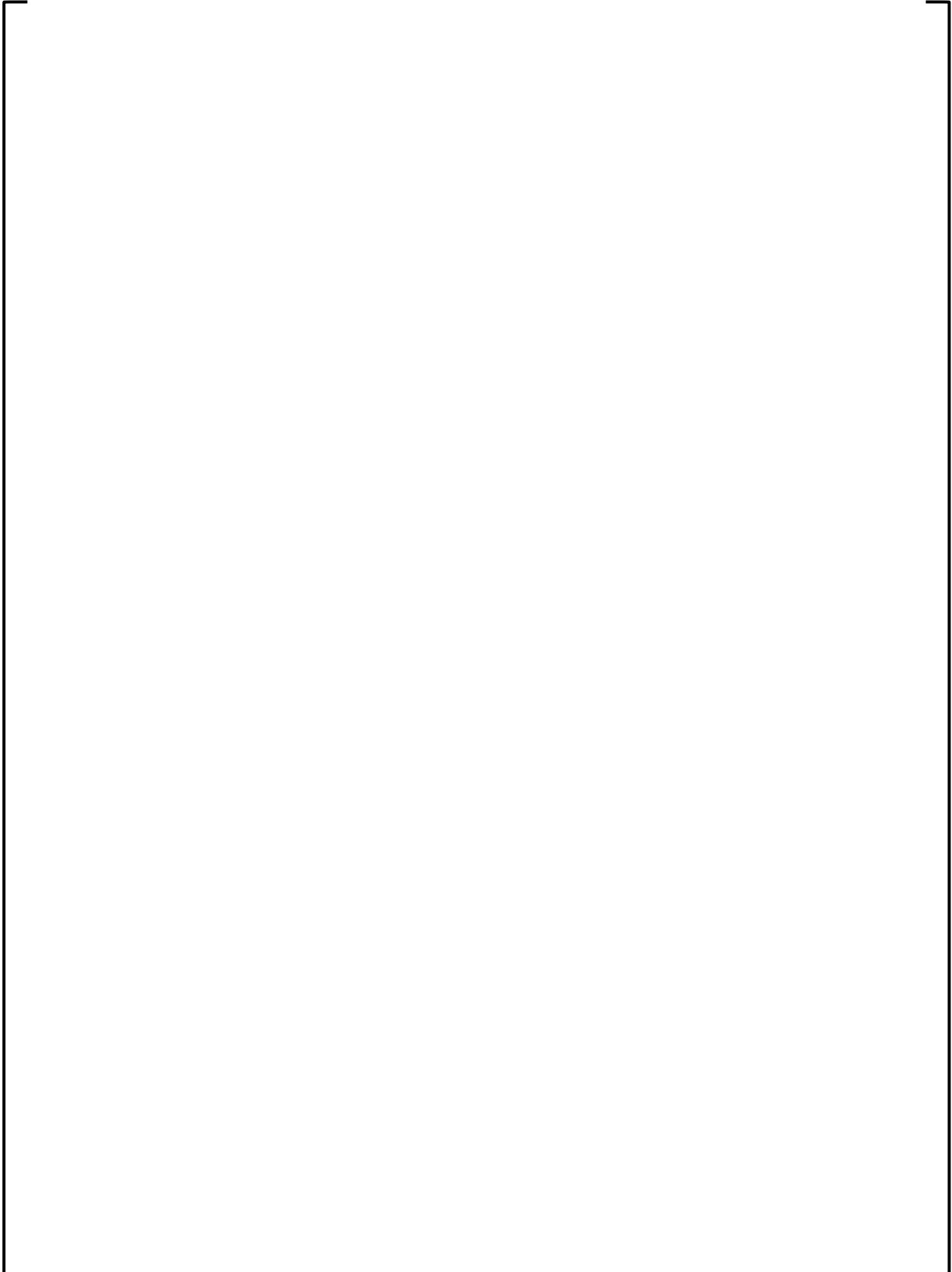
Figure 3-40: PARAGON2 vs. Measured Isotopics for Rod D5, Sample B1 of TMI-1

a,b,c
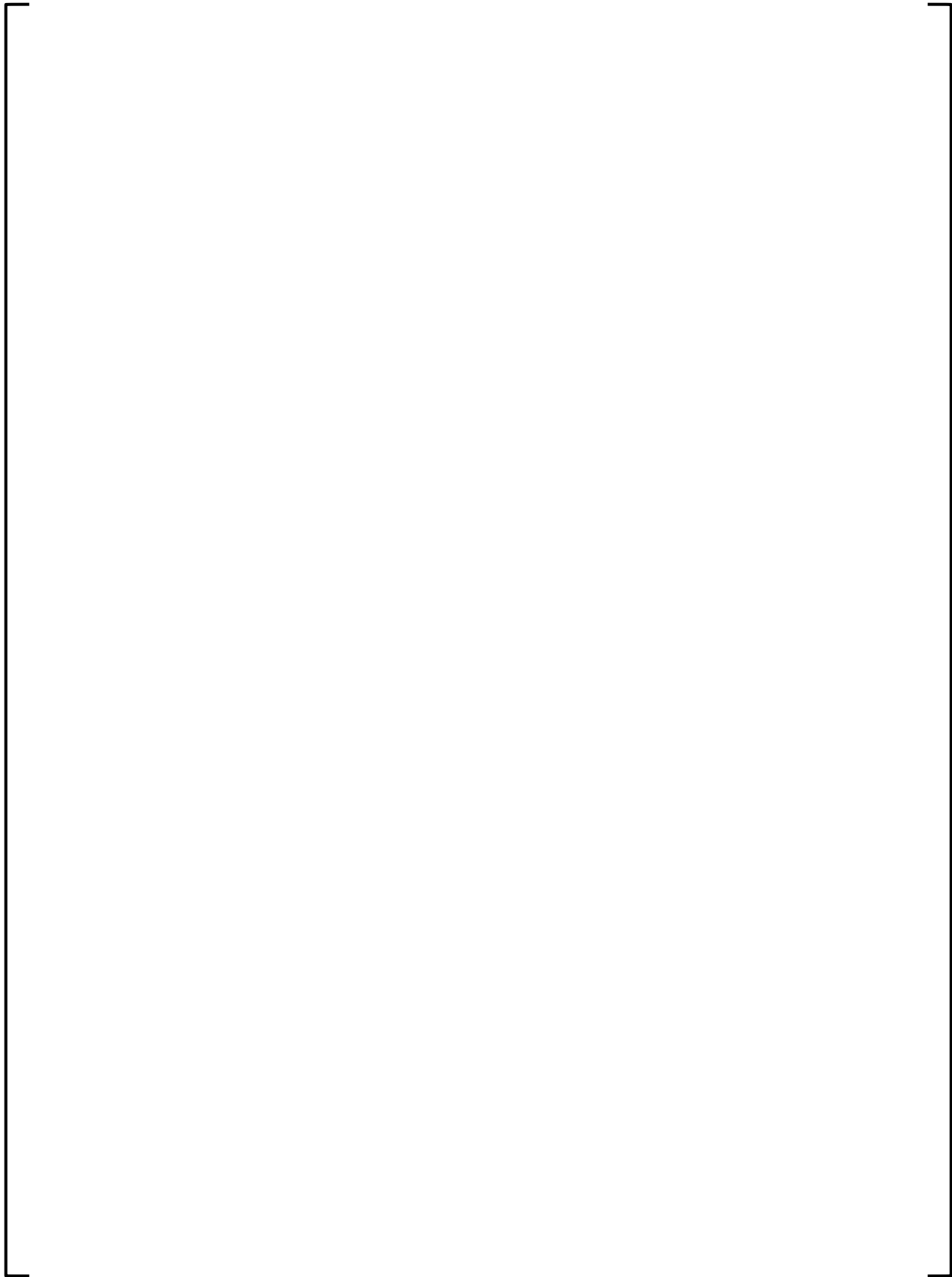
Figure 3-41: PARAGON2 vs. Measured Isotopics for Rod H6, Sample C2D1 of TMI-1

a,b,c
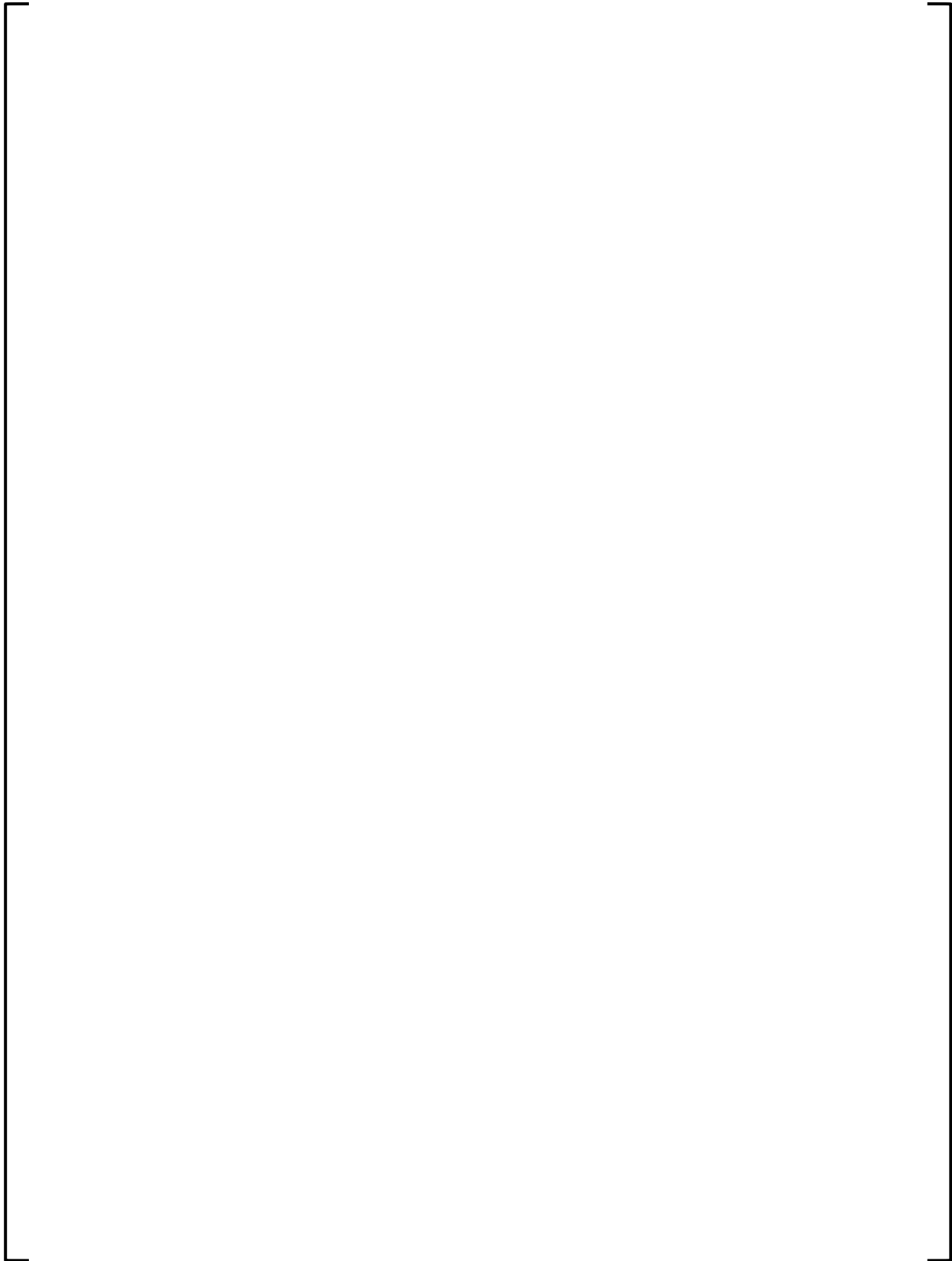
Figure 3-42: PARAGON2 vs. Measured Isotopics for Rod H6, Sample C2D2 of TMI-1

a,b,c
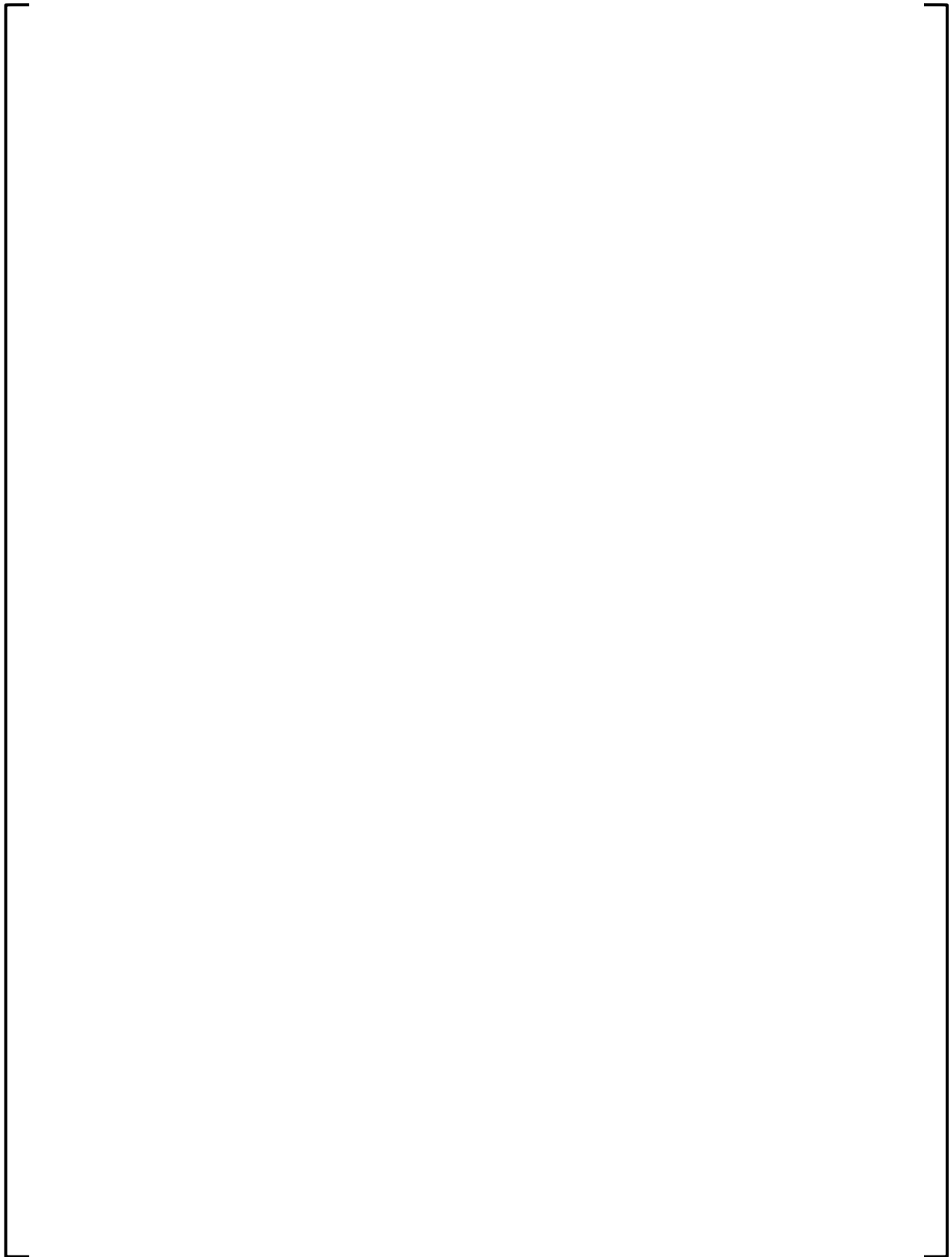
Figure 3-43: PARAGON2 vs. Measured Isotopics for Rod MKP109, Sample CC of Calvert Cliffs-1

a,b,c
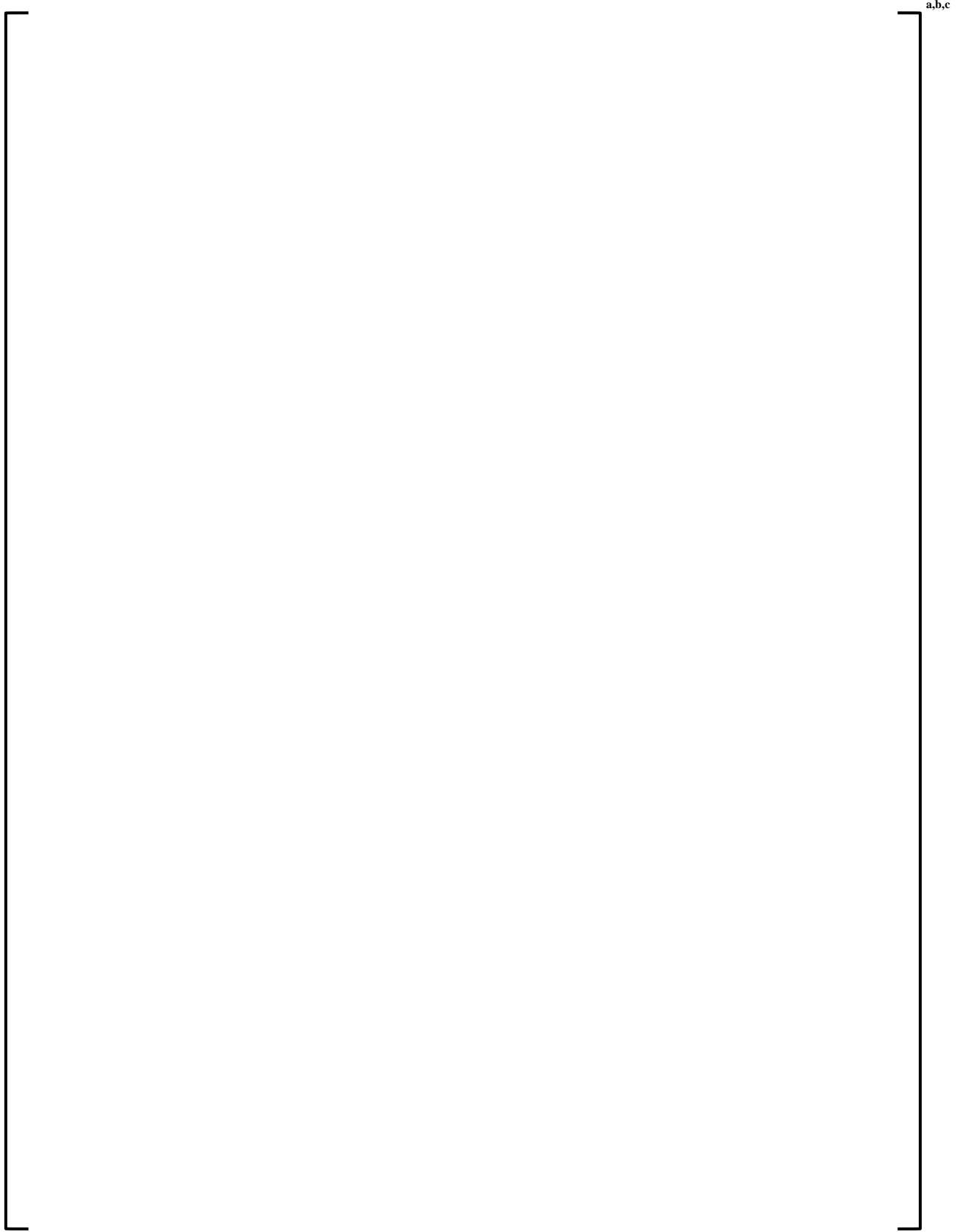
Figure 3-44: PARAGON2 vs. Measured Isotopics for Rod MKP109, Sample LL of Calvert Cliffs-1

a,b,c
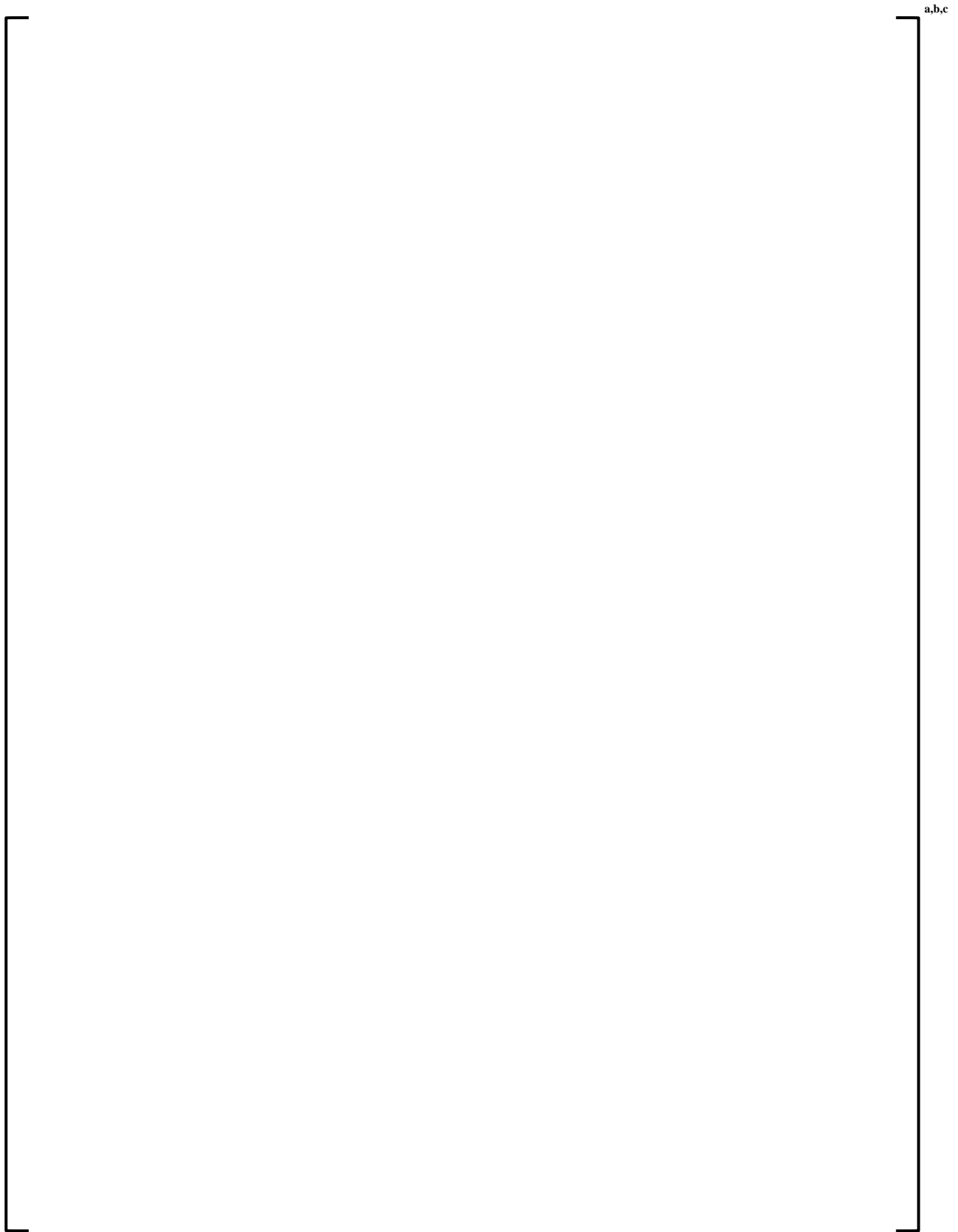
Figure 3-45: PARAGON2 vs. Measured Isotopics for Rod MKP109, Sample P of Calvert Cliffs-1

a,b,c

Figure 3-46: PARAGON2 vs. Measured Isotopics for Sample 4 of Turkey Point

a,b,c
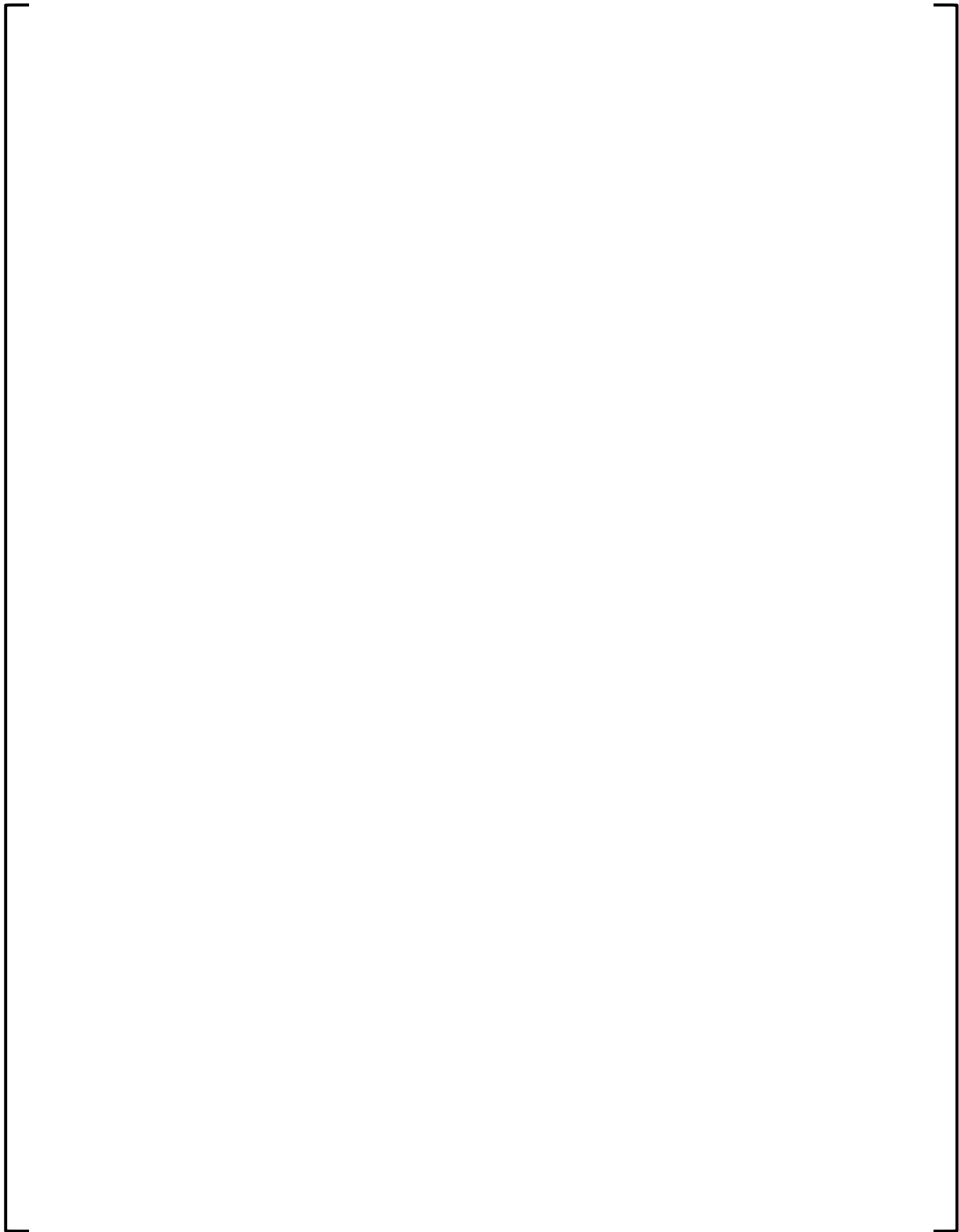
Figure 3-47: PARAGON2 vs. Measured Isotopics for Sample E58-88 at 43.5 GWD/MTU of Vandellos

a,b,c
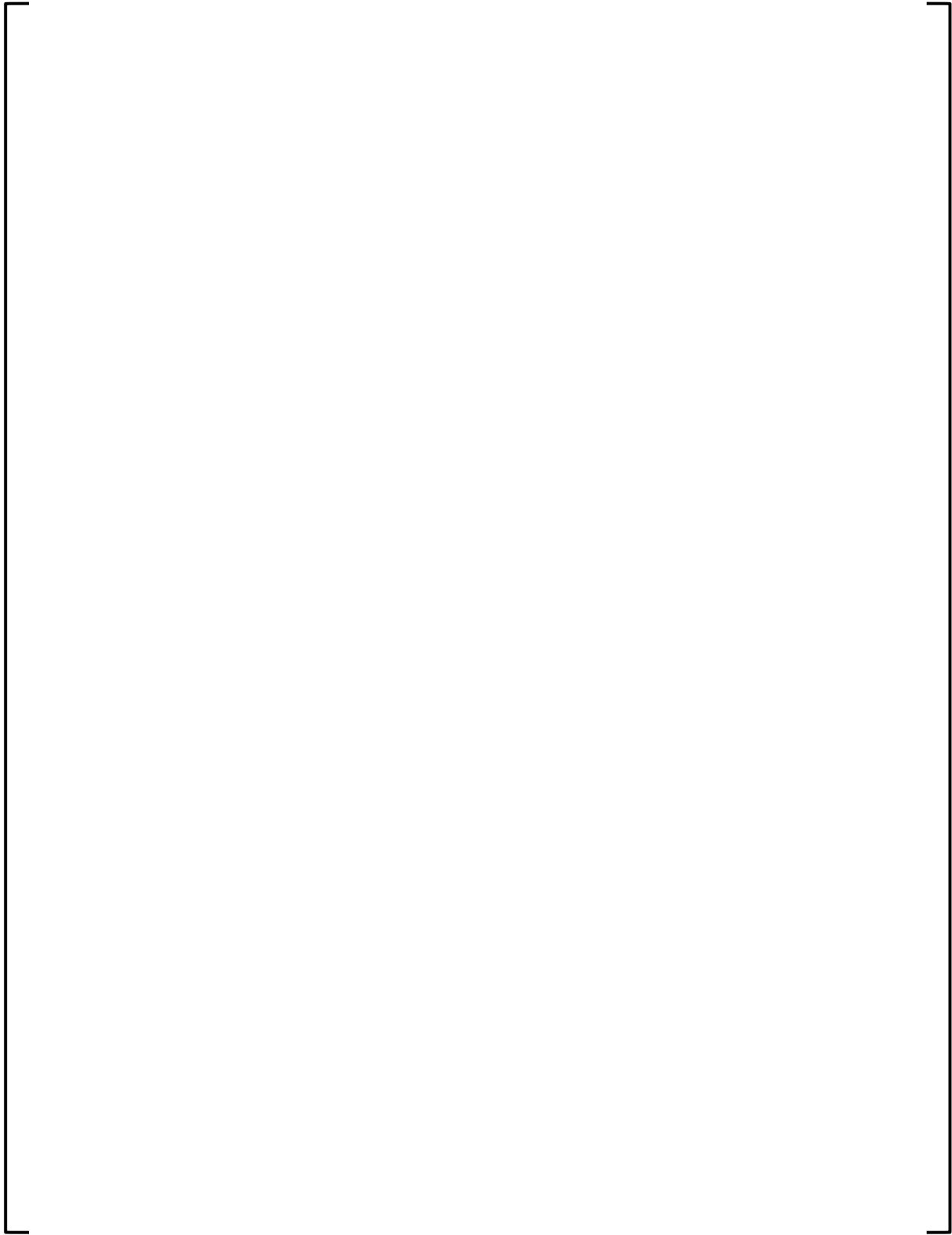
Figure 3-48: PARAGON2 vs. Measured Isotopics for Sample E58-263 at 63.01 GWD/MTU of Vandellos

a,b,c
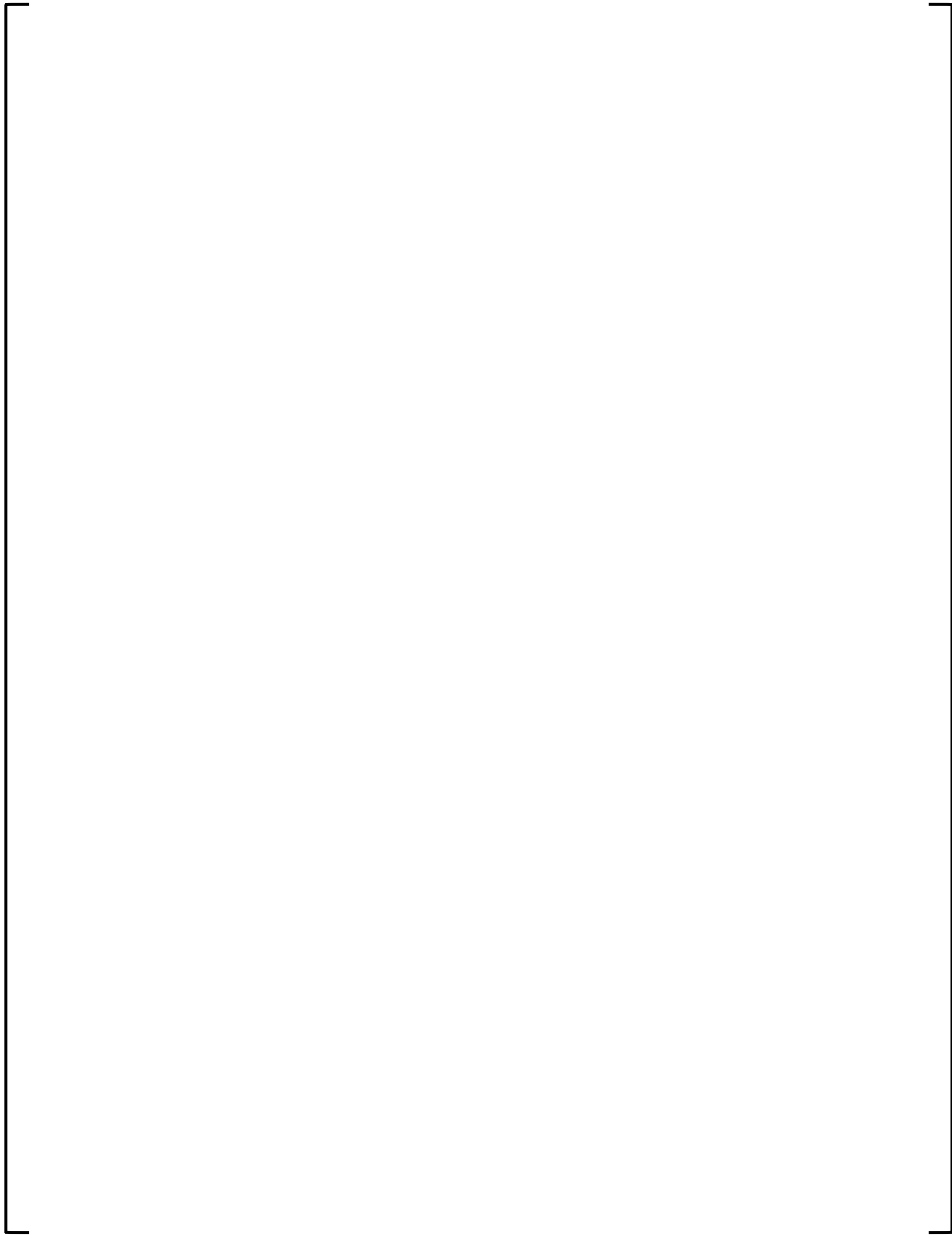
Figure 3-49: PARAGON2 vs. Measured Isotopics for Sample E58-773 at 74.57 GWD/MTU of Vandellos

a,b,c

Figure 3-50: Saxton Fuel Performance Evaluation Program: PARAGON2 U-235/U Prediction vs. Burnup

a,b,c
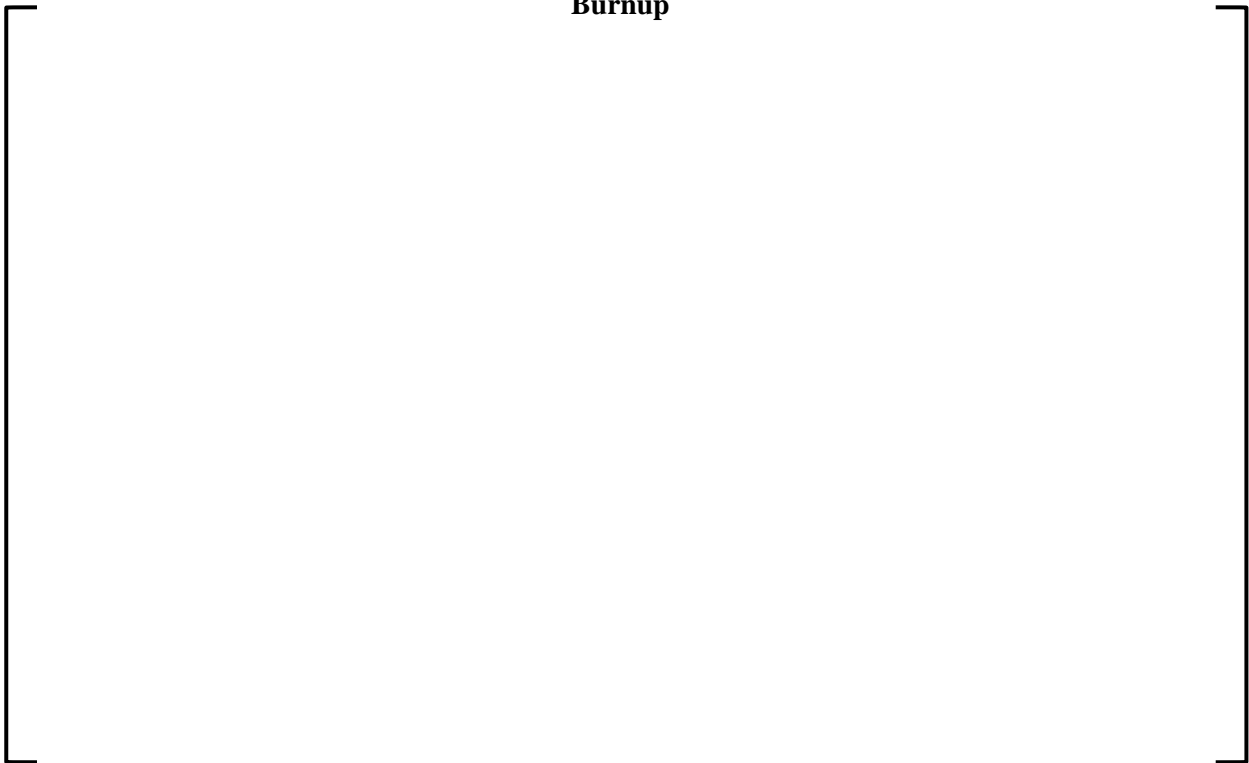
Figure 3-51: Saxton Fuel Performance Evaluation Program: PARAGON2 U-236/U Prediction vs. Burnup

a,b,c

Figure 3-52: Saxton Fuel Performance Evaluation Program: PARAGON2 U-238/U Prediction vs. Burnup

a,b,c

Figure 3-53: Saxton Fuel Performance Evaluation Program: PARAGON2 Pu-239/Pu Prediction vs. Burnup

a,b,c

Figure 3-54: Saxton Fuel Performance Evaluation Program: PARAGON2 Pu-240/Pu Prediction vs. Burnup

a,b,c
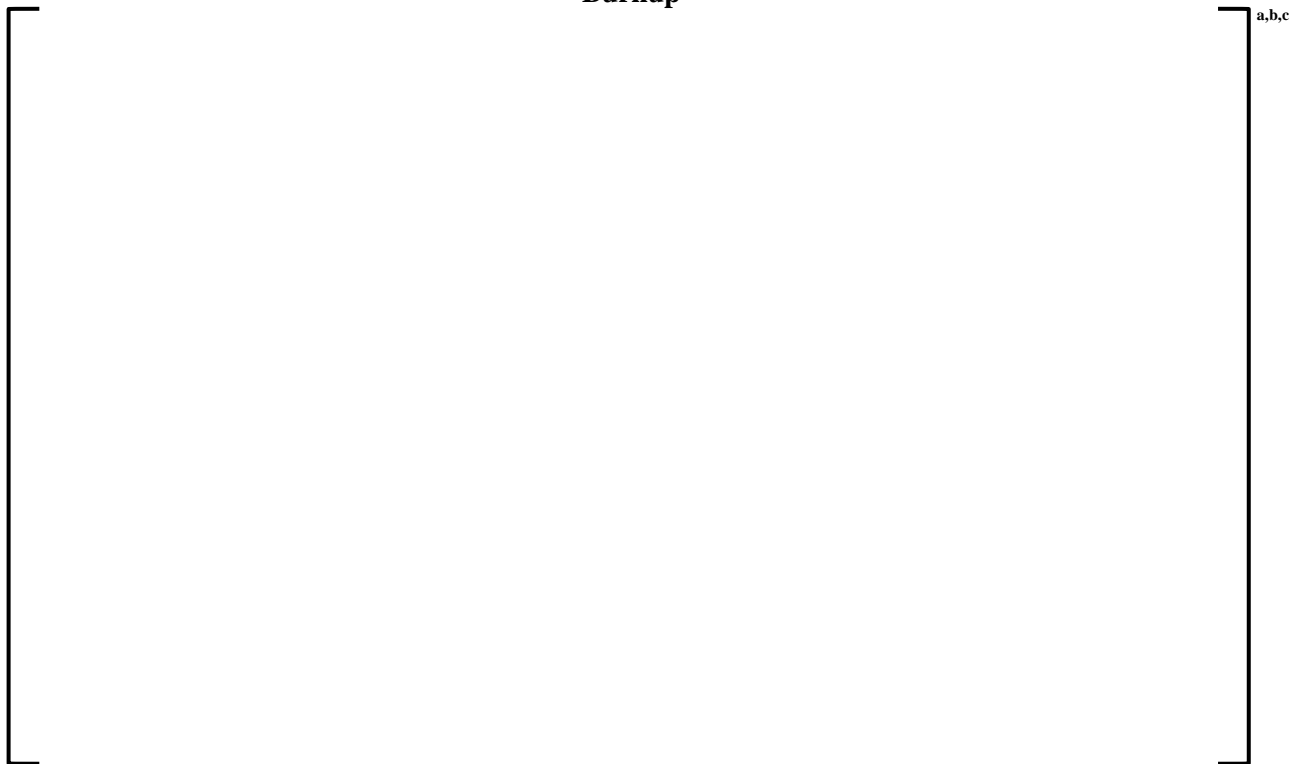
Figure 3-55: Saxton Fuel Performance Evaluation Program: PARAGON2 Pu-241/Pu Prediction vs. Burnup

a,b,c

Figure 3-56: Saxton Fuel Performance Evaluation Program: PARAGON2 Pu-242/Pu Prediction vs. Burnup

a,b,c
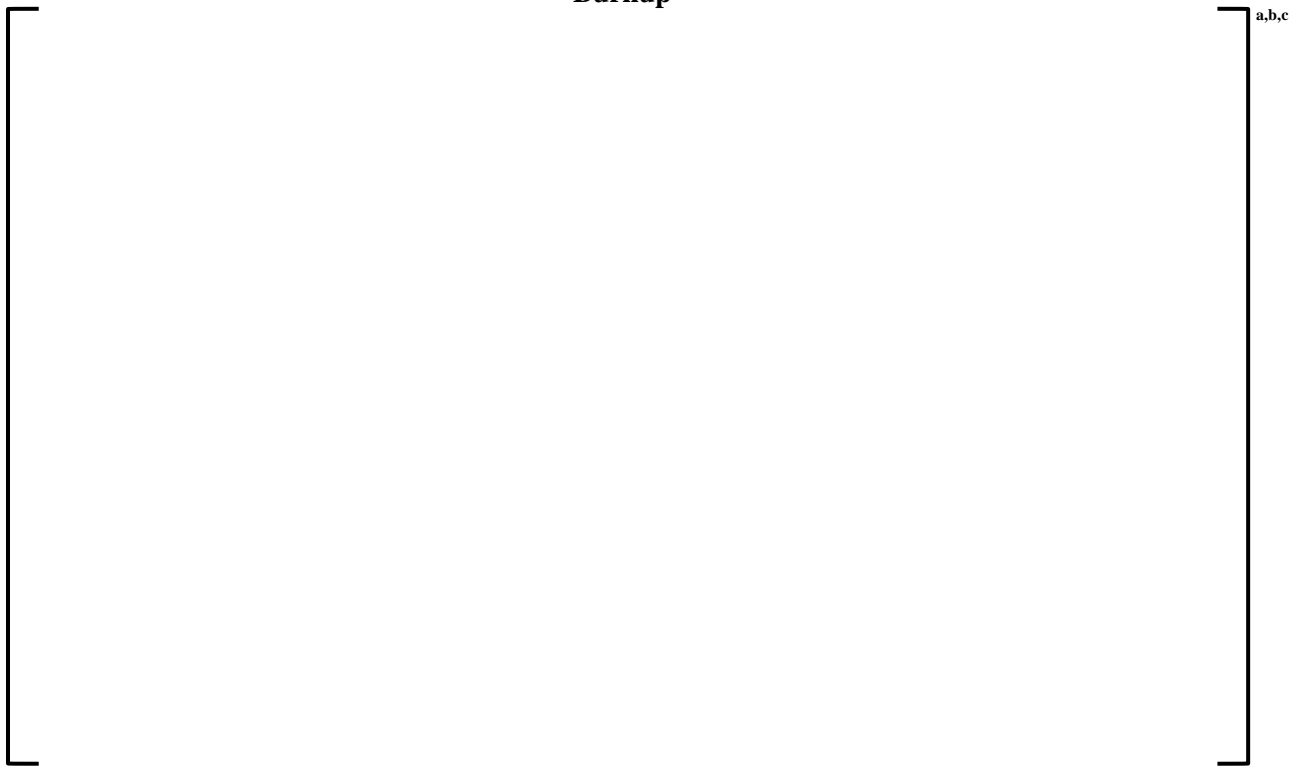
Figure 3-57: Saxton Fuel Performance Evaluation Program: PARAGON2 Pu-239/U-238 Prediction vs. Burnup

a,b,c

Figure 3-58: Saxton Fuel Performance Evaluation Program: PARAGON2 Pu-239/Pu-240 Prediction vs. Burnup

a,b,c
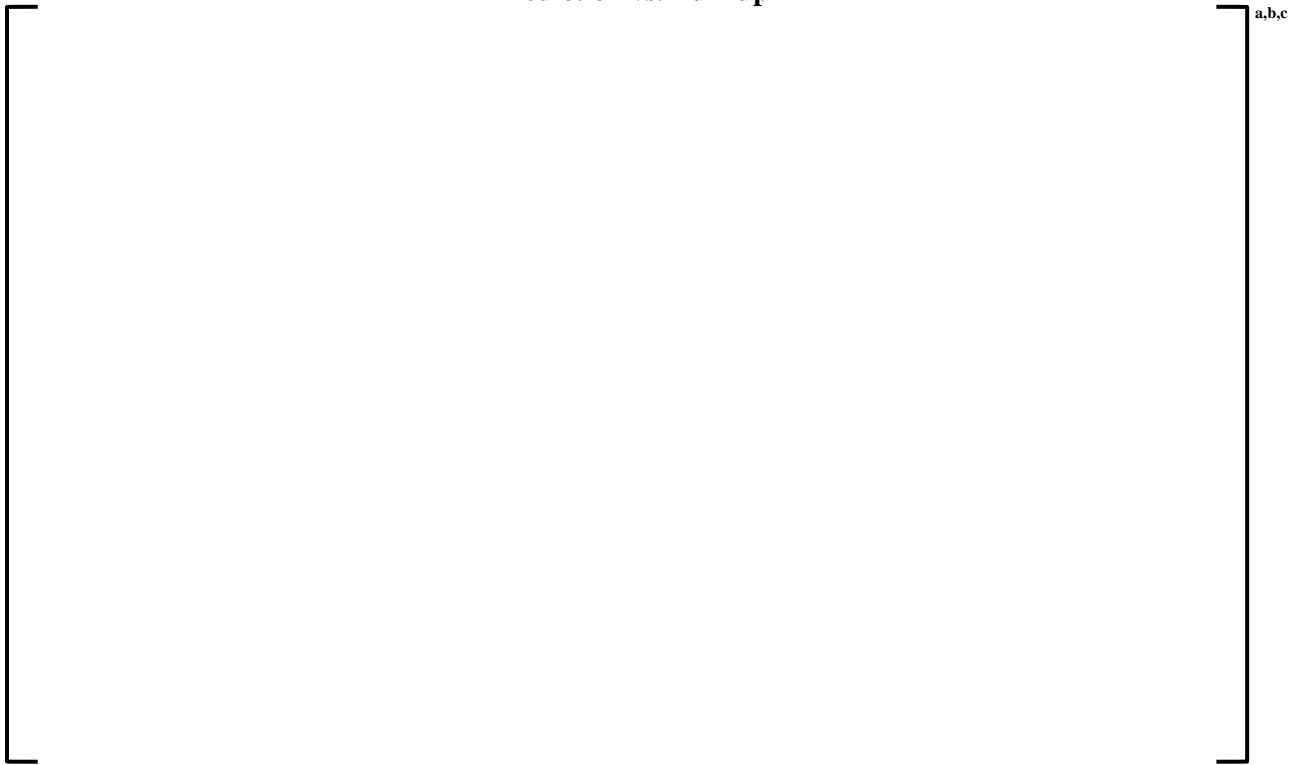
Figure 3-59: Saxton Fuel Performance Evaluation Program: PARAGON2 Pu-240/Pu-241 Prediction vs. Burnup

a,b,c

Figure 3-60: Saxton Fuel Performance Evaluation Program: PARAGON2 Pu-241/Pu-242 Prediction vs. Burnup

a,b,c
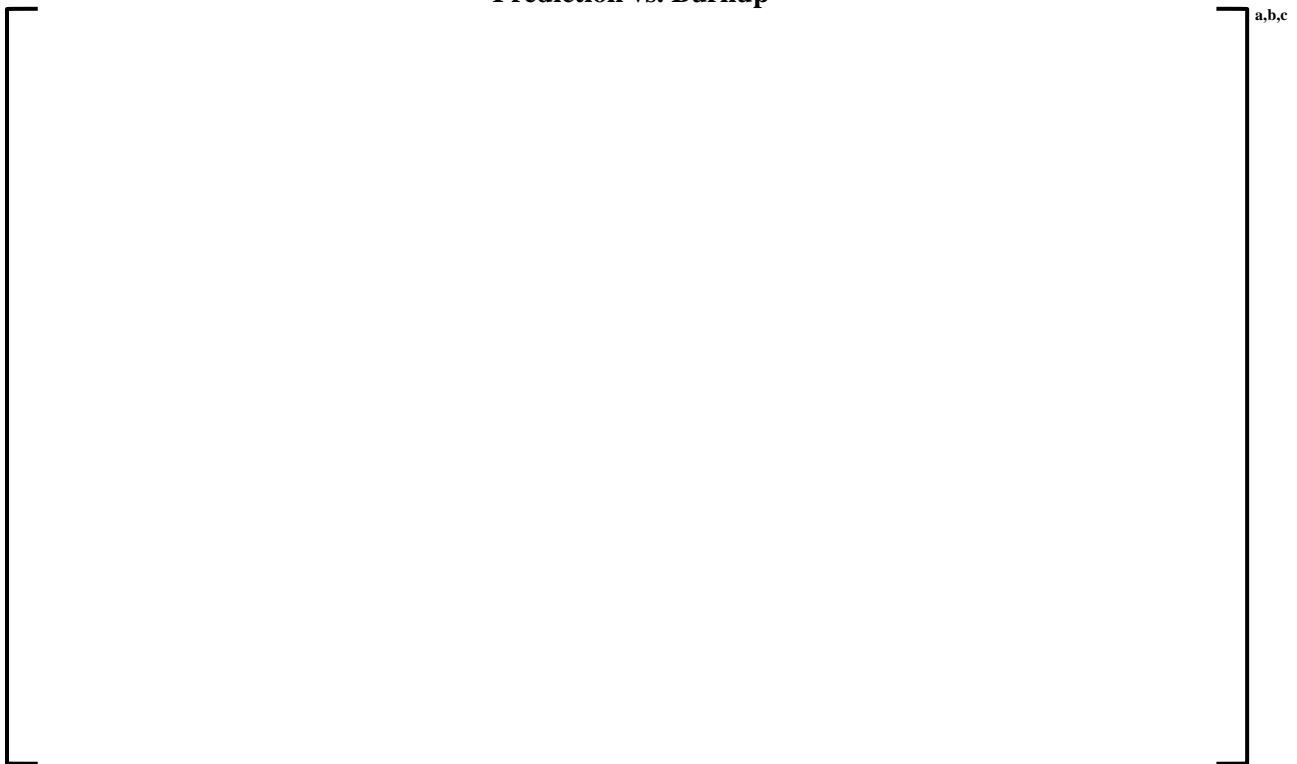
Figure 3-61: Saxton Fuel Performance Evaluation Program: PARAGON2 U-236/U-235 Prediction vs. Burnup

a,b,c

Figure 3-62: Saxton Fuel Performance Evaluation Program: PARAGON2 U-236/U-238 Prediction vs. Burnup

a,b,c
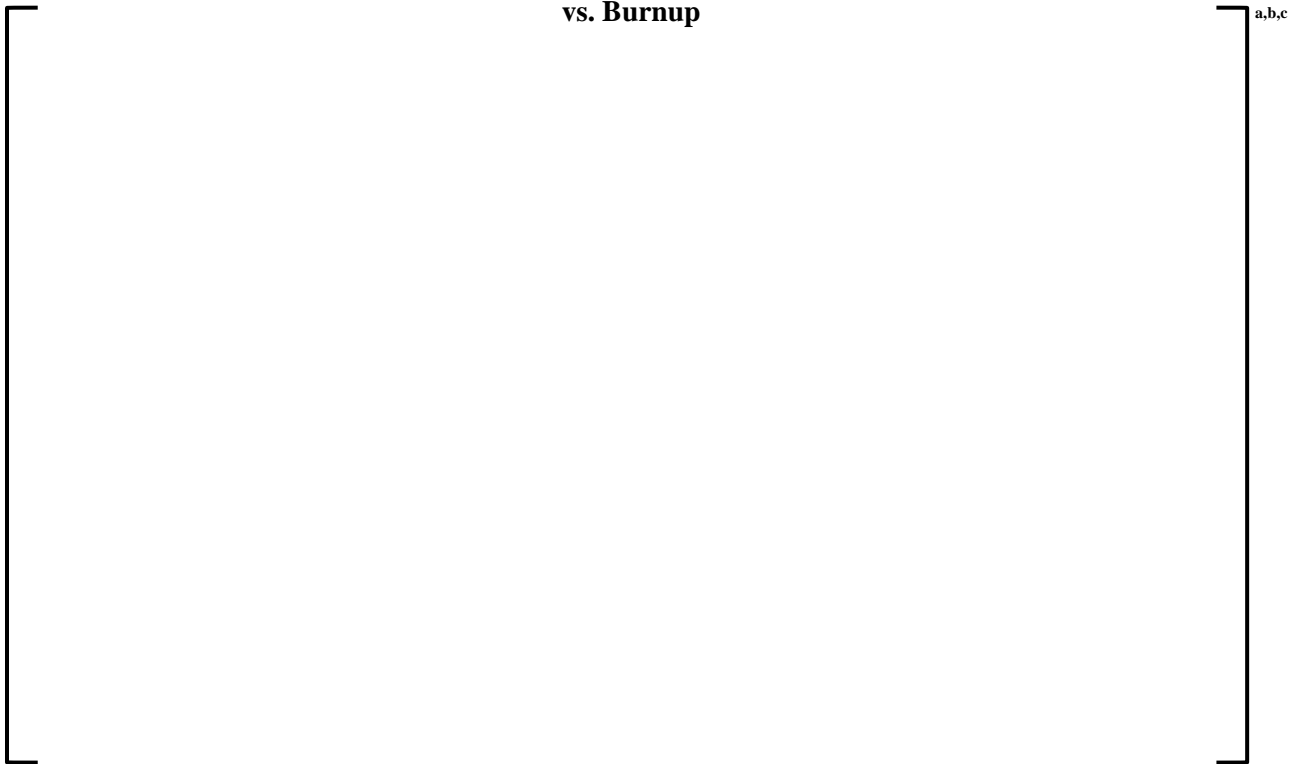
Figure 3-63: Yankee Core Evaluation Program (Stainless Steel Clad): PARAGON2 U-235/U Prediction vs. Burnup

a,b,c

Figure 3-64: Yankee Core Evaluation Program (Stainless Steel Clad): PARAGON U-236/U Prediction vs. Burnup

a,b,c

Figure 3-65: Yankee Core Evaluation Program (Stainless Steel Clad): PARAGON2 U-238/U Prediction vs. Burnup

a,b,c

Figure 3-66: Yankee Core Evaluation Program (Stainless Steel Clad): PARAGON2 Pu-239/Pu Prediction vs. Burnup

a,b,c

Figure 3-67: Yankee Core Evaluation Program (Stainless Steel Clad): PARAGON2 Pu-240/Pu Prediction vs. Burnup

a,b,c

Figure 3-68: Yankee Core Evaluation Program (Stainless Steel Clad): PARAGON2 Pu-241/Pu Prediction vs. Burnup

a,b,c
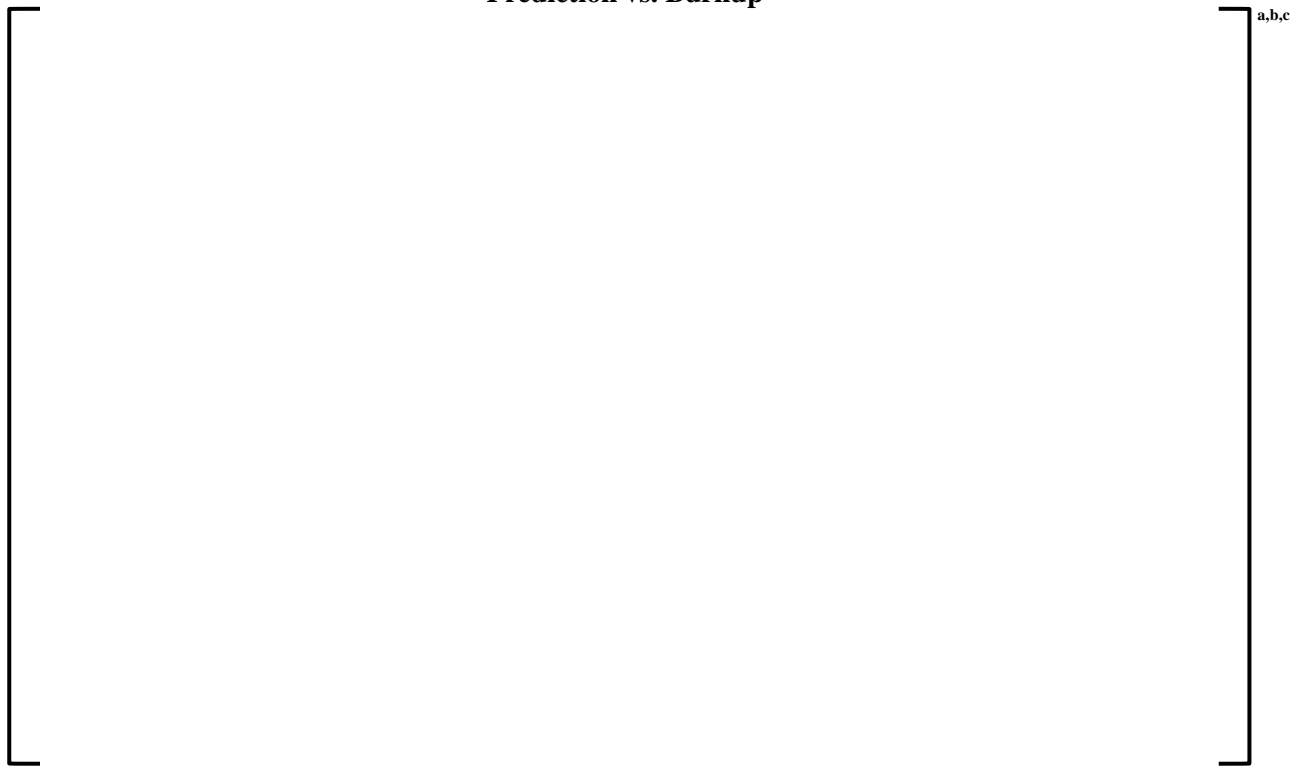
Figure 3-69: Yankee Core Evaluation Program (Stainless Steel Clad): PARAGON2 Pu-242/Pu Prediction vs. Burnup

a,b,c

Figure 3-70: Yankee Core Evaluation Program (Stainless Steel Clad): PARAGON2 Pu-239/U-238 Prediction vs. Burnup

a,b,c
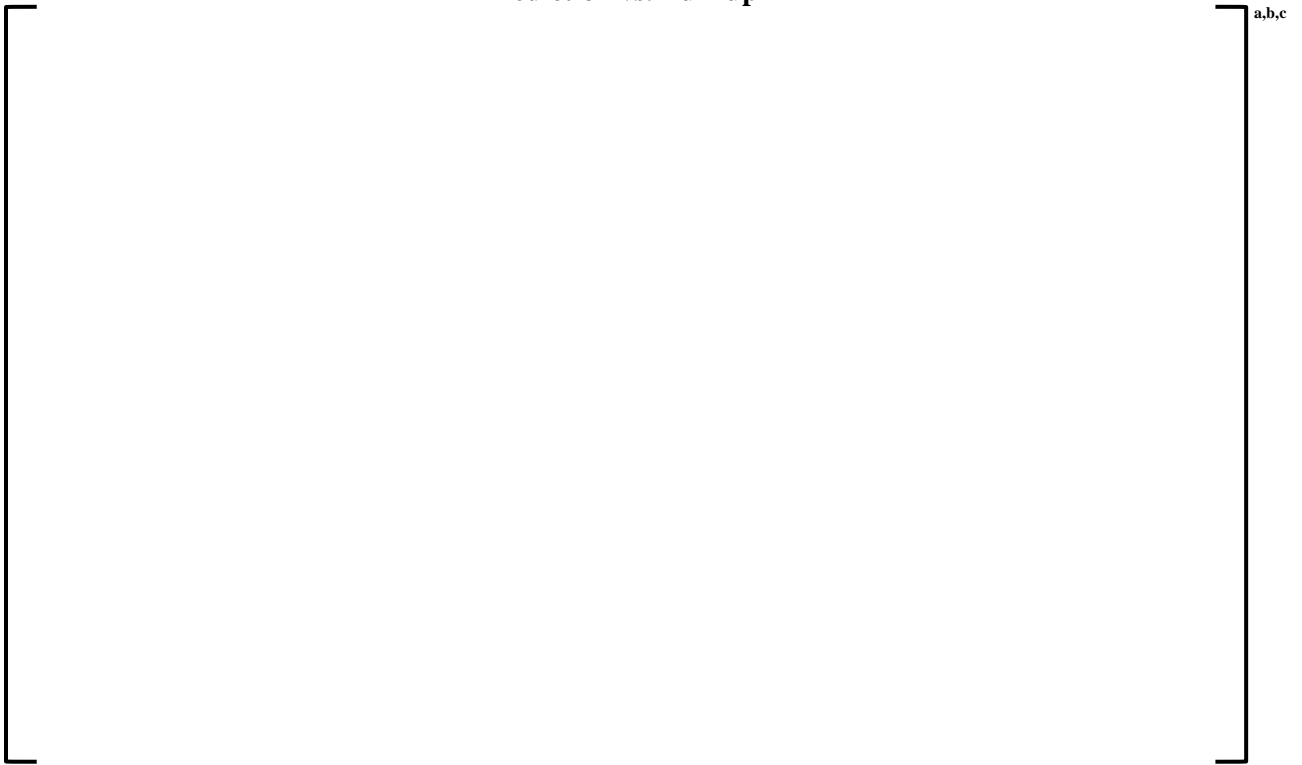
Figure 3-71: Yankee Core Evaluation Program (Stainless Steel Clad): PARAGON2 Pu-239/Pu-240 Prediction vs. Burnup

a,b,c

Figure 3-72: Yankee Core Evaluation Program (Stainless Steel Clad): PARAGON2 Pu-240/Pu-241 Prediction vs. Burnup

a,b,c

Figure 3-73: Yankee Core Evaluation Program (Stainless Steel Clad): PARAGON2 Pu-241/Pu-242 Prediction vs. Burnup

a,b,c

Figure 3-74: Yankee Core Evaluation Program (Stainless Steel Clad): PARAGON2 U-236/U-235 Prediction vs. Burnup

a,b,c
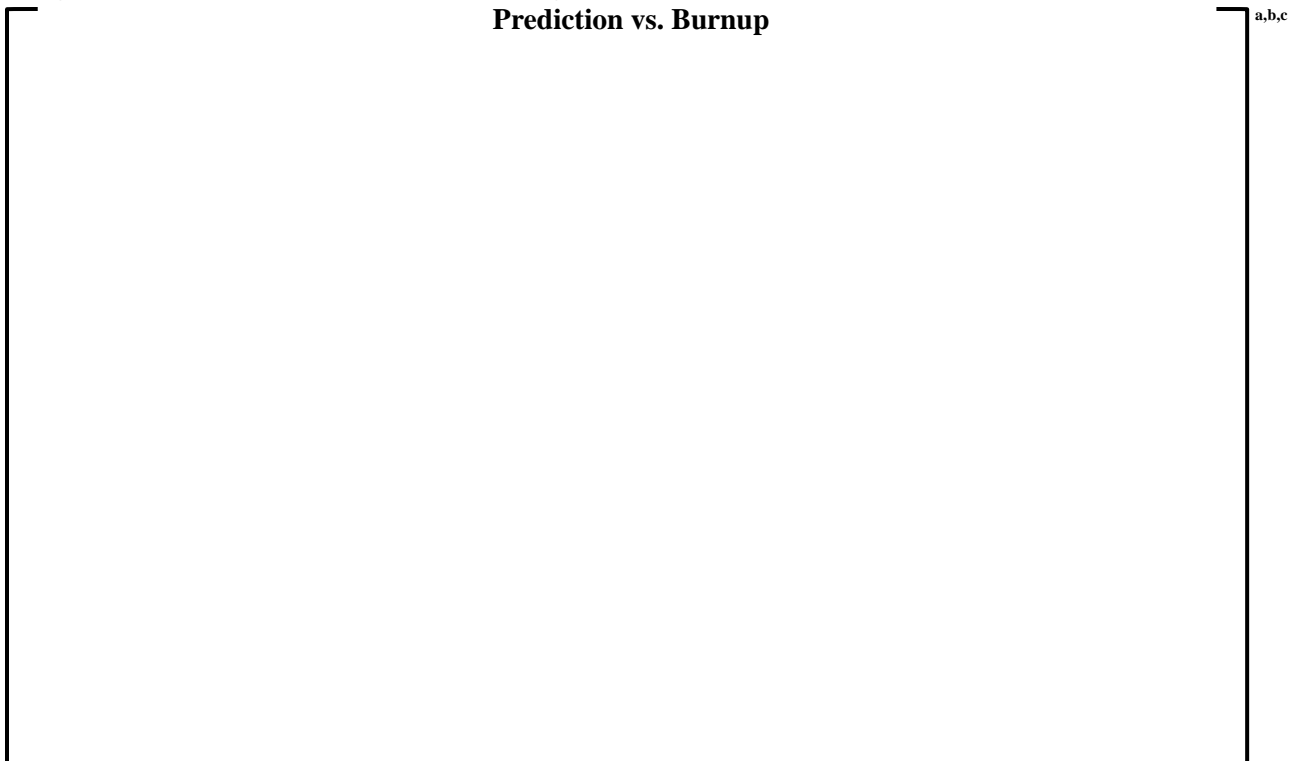
Figure 3-75: Yankee Core Evaluation Program (Stainless Steel Clad): PARAGON2 U-235/U-238 Prediction vs. Burnup

a,b,c

Figure 3-76: Yankee Core Evaluation Program (Zircaloy Clad): PARAGON2 U-235/U Prediction vs. Burnup

a,b,c
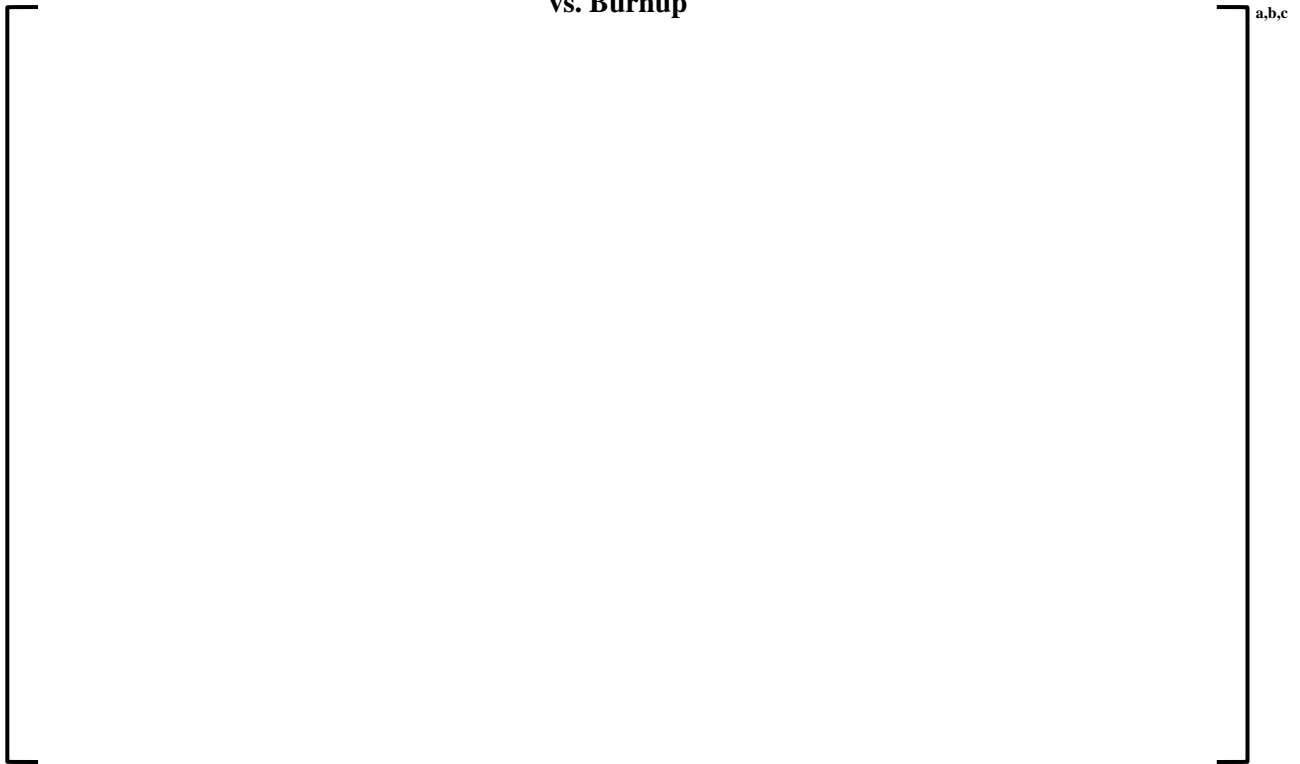
Figure 3-77: Yankee Core Evaluation Program (Zircaloy Clad): PARAGON2 U-236/U Prediction vs. Burnup

a,b,c

Figure 3-78: Yankee Core Evaluation Program (Zircaloy Clad): PARAGON2 U-238/U Prediction vs. Burnup

a,b,c

Figure 3-79: Yankee Core Evaluation Program (Zircaloy Clad): PARAGON2 Pu-239/Pu Prediction vs. Burnup

a,b,c
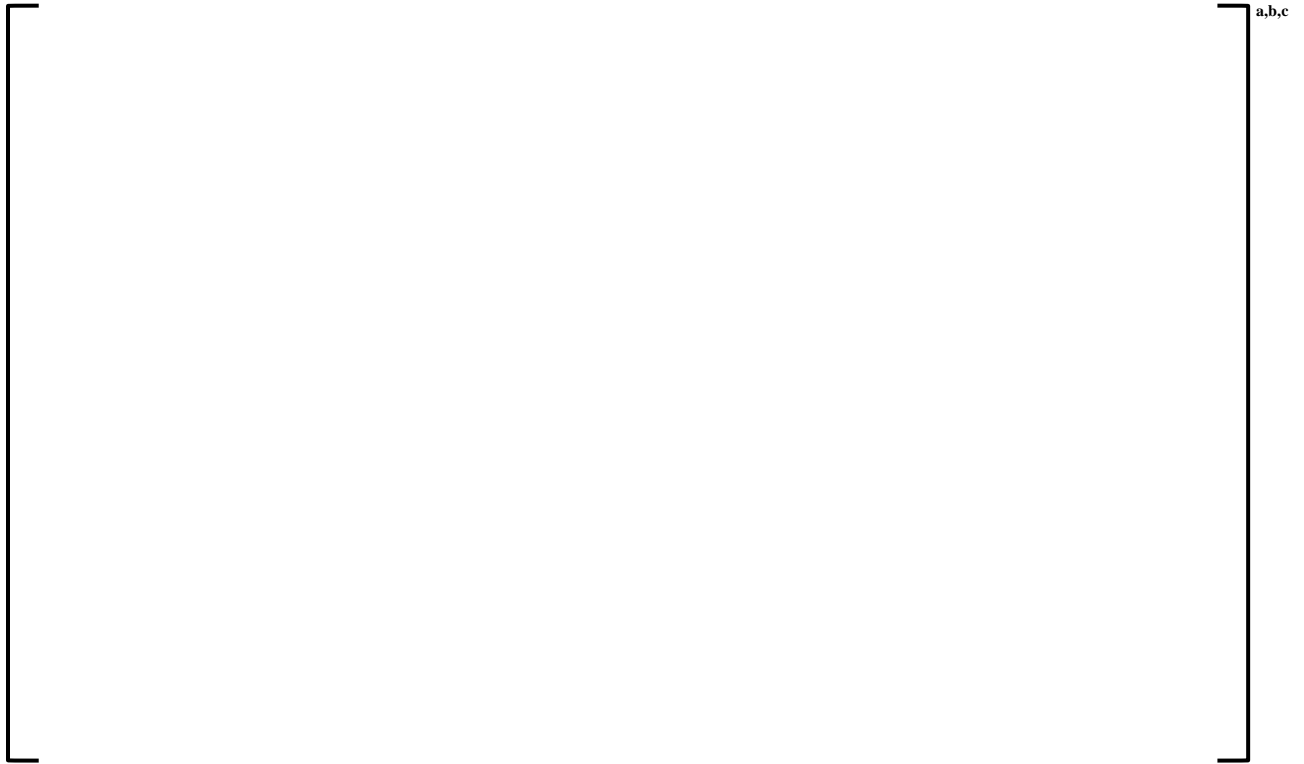
Figure 3-80: Yankee Core Evaluation Program (Zircaloy Clad): PARAGON2 Pu-240/Pu Prediction vs. Burnup

a,b,c
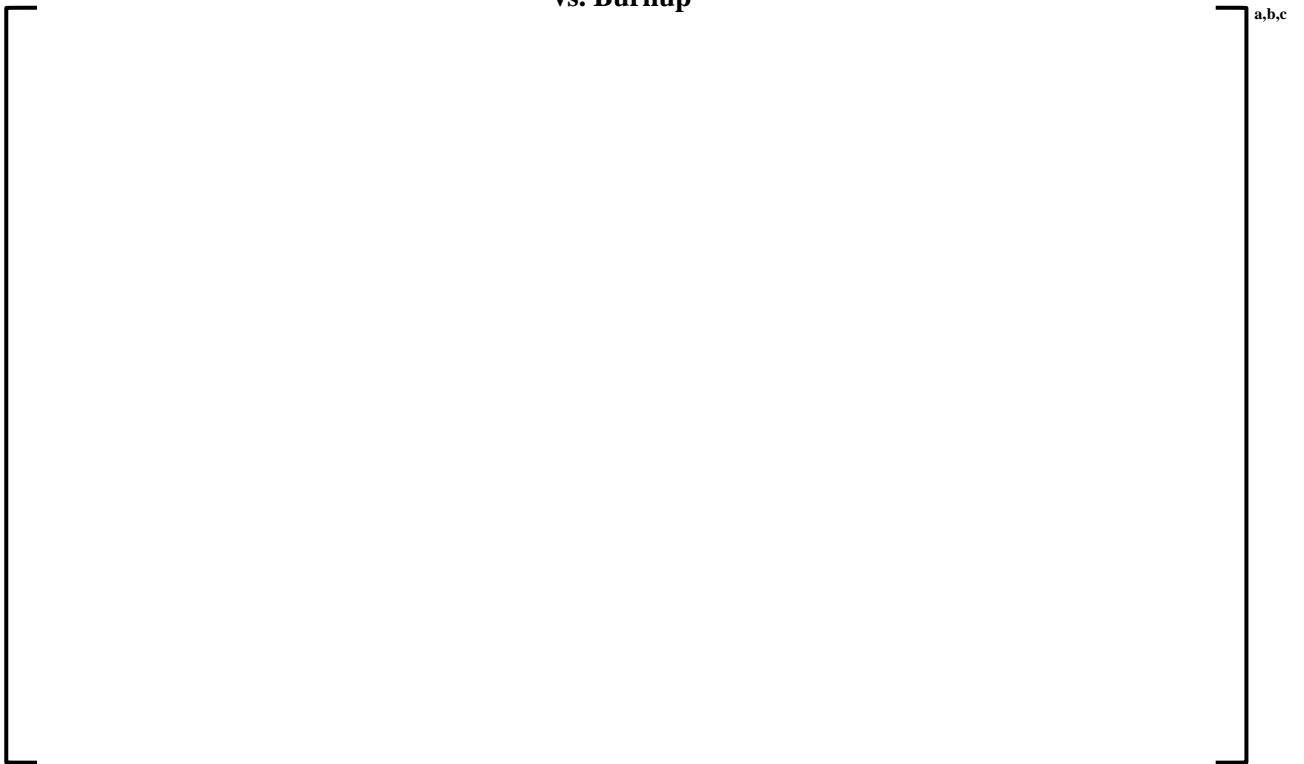
Figure 3-81: Yankee Core Evaluation Program (Zircaloy Clad): PARAGON2 Pu-241/Pu Prediction vs. Burnup

a,b,c

Figure 3-82: Yankee Core Evaluation Program (Zircaloy Clad): PARAGON2 Pu-242/Pu Prediction vs. Burnup

a,b,c
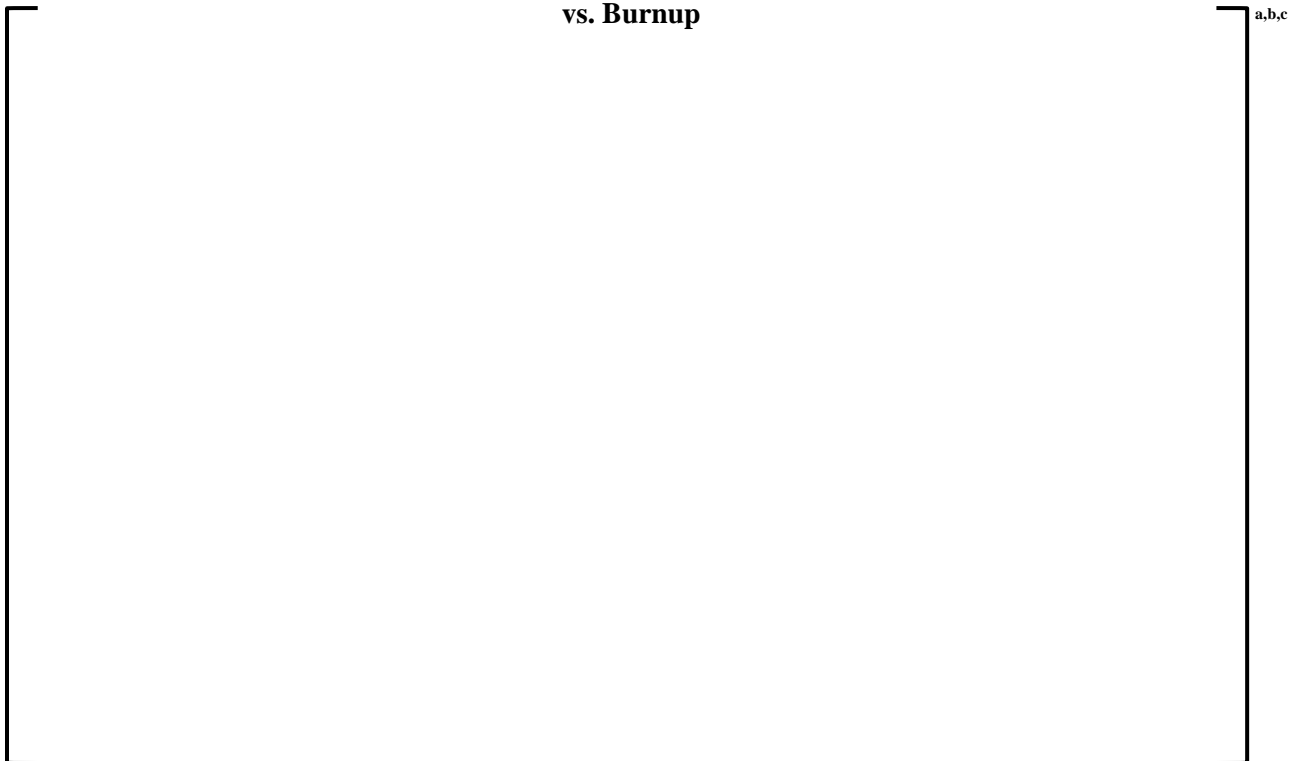
Figure 3-83: Yankee Core Evaluation Program (Zircaloy Clad) PARAGON2 Pu-239/U-238 Prediction vs. Burnup

a,b,c

Figure 3-84: Yankee Core Evaluation Program (Zircaloy Clad): PARAGON2 Pu-239/Pu-240 Prediction vs. Burnup

a,b,c
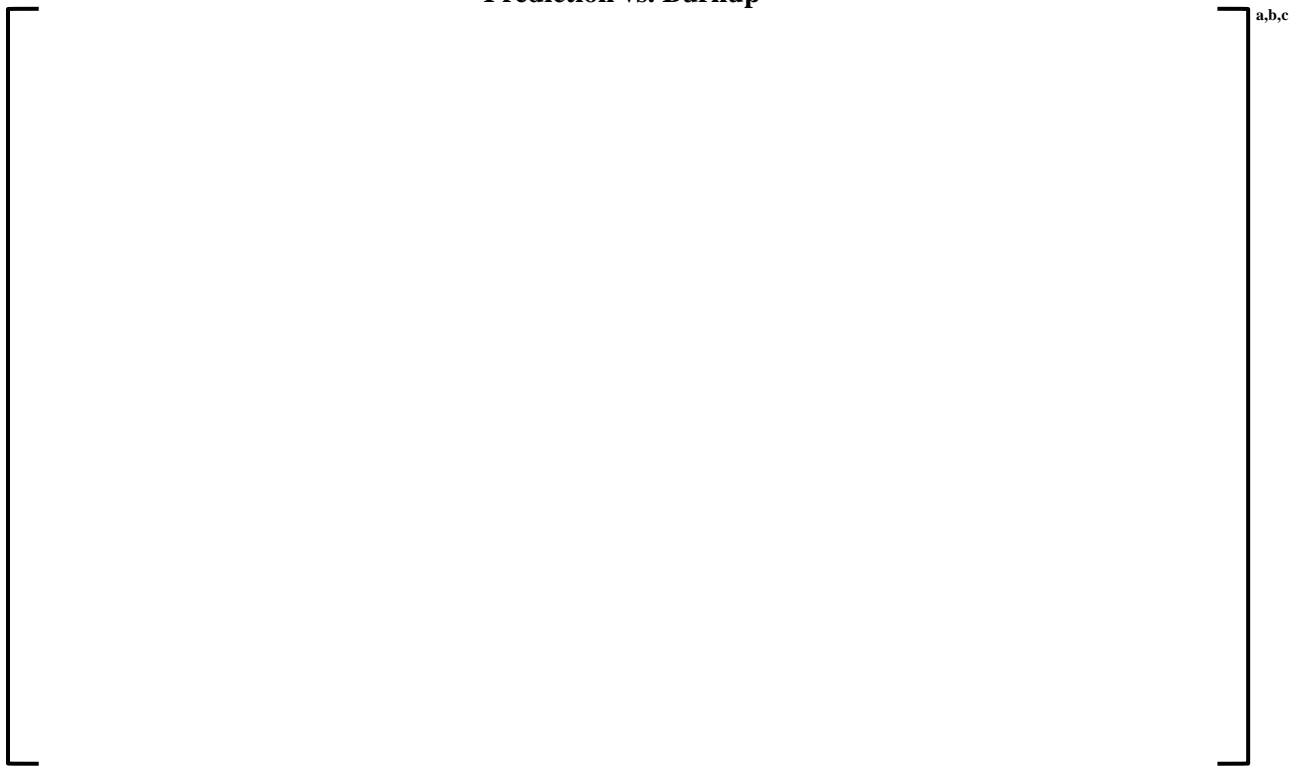
Figure 3-85: Yankee Core Evaluation Program (Zircaloy Clad): PARAGON2 Pu-240/Pu-241 Prediction vs. Burnup

a,b,c

Figure 3-86: Yankee Core Evaluation Program (Zircaloy Clad): PARAGON2 Pu-241/Pu-242 Prediction vs. Burnup

a,b,c

Figure 3-87: Yankee Core Evaluation Program (Zircaloy Clad): PARAGON2 U-236/U-235 Prediction vs. Burnup

a,b,c

**Figure 3-88: Yankee Core Evaluation Program (Zircaloy Clad): PARAGON2 U-235/U-238
Prediction vs. Burnup**

4   MONTE CARLO BENCHMARKS

SERPENT2 Monte Carlo code [19] will be used in this analysis, instead of MCNP, in order to use its depletion capability. However, SERPENT2 is equivalent to the MCNP code, in that the effective multiplication factors and homogenized few-group cross-sections are within the statistical accuracy of the reference MCNP results when equivalent inputs are used

Ten assembly configurations were calculated in both PARAGON2 and the Monte Carlo code SERPENT2. These assembly configurations were chosen to cover a variety of lattice types, burnable absorbers, a large enrichment range, and both UO_2 and MOX. Specifically, the following describes the parameter range covered by these configurations:

[   ]^{a,c}

The RSM in SERPENT2 models was limited to some selected isotopes (Ref. [36]) in contrast to PARAGON2 models where all isotopes use the RSM. In addition, the RSM theoretical models of the two codes are slightly different. Therefore, the asymptotic results were chosen for most of the reported Monte-Carlo comparisons instead of the RSM results.

Table 4-1 presents the reactivity results of the assembly calculations for cold (300 K), HZP (600 K) and HFP conditions at zero burnup and enrichment less than 5 wt%. The temperatures used in HFP are 900 K for fuel and 600 K for clad and moderator regions. For each assembly configuration, the table presents the lattice type, the enrichment, the number and type of burnable absorber present and the difference in pcm between the PARAGON2 and SERPENT2 k-infinities for cold, HZP, HFP and HFP with control rods inserted. [   ]^{a,c} As it can be seen from the table, the mean difference between the PARAGON2 and SERPENT2 k_{inf} values was very good and in the interval between [   ]^{a,c}. All the absolute differences are less than [   ]^{a,c}. The agreement between the two codes is very good for all conditions and all fuel types. The SERPENT2 runs were performed with sufficient neutron histories to achieve [   ]^{a,c} for all the k-infinities including during the depletion.

Figure 4-1 through Figure 4-10 display the HFP delta reactivity (PARAGON2 minus SERPENT2) in pcm as a function of burnup as well as the k-infinities of both codes. The k_{inf} values plotted correspond to the asymptotic scattering model. The deltas ($\delta_k = k_\infty^{P2} - k_\infty^{S2}$) are presented for both asymptotic and resonance scattering models. The RSM models used a fuel temperature of [   ]^{a,c} to emphasize the impact the upscattering phenomenon (other temperatures are kept the same as in the asymptotic case). For both the asymptotic and the RSM calculations, the maximum average difference between SERPENT2 and PARAGON2 is [   ]^{a,c}. The maximum absolute difference obtained is [   ]^{a,c}. Combining all the assembly cases, the statistics for the asymptotic runs are given in Figure 4-11 for all the burnup points. Overall, the results in Figure 4-11 are very good

with an average difference of only **[   ]ᵃ,ᶜ**. More in-depth analysis is in Ref. [37].

Figure 4-12 through Figure 4-21 present comparisons between SERPENT2 and PARAGON2 rod power distributions for the ten assemblies listed in Table 4-1. For each power distribution figure, the comparison was made at 0 MWD/MTU (BOL), 10 GWD/MTU (MOL) and 70 GWD/MTU (EOL). These figures demonstrate that PARAGON2 rod power predictions are well predicted. The maximum standard deviation is **[   ]ᵃ,ᶜ** and, for the individual pins, the maximum absolute error obtained for all calculations of all burnups is **[   ]ᵃ,ᶜ**. For the overall statistics given in Figure 4-22, the standard deviation of the relative differences is **[   ]ᵃ,ᶜ**. The predictions of PARAGON2 are very good and very consistent across all burnups and all fuel types. Sufficient histories were run so that the SERPENT2 1σ standard deviation for each rod power was less than 1 percent in all cases.

In Figure 4-23, PARAGON2 is compared to SERPENT2 for all selected assemblies. The comparison was first made for the CZP conditions, where the temperature was set to 300 K for all regions in the assemblies. The results obtained were very good. Indeed, the absolute maximum difference between two codes is **[   ]** for all cases and all enrichments with an average of **[   ]ᵃ,ᶜ**.

Next, the PARAGON2 calculations were done for HZP condition where the isothermal temperature used is 600 K. The results obtained were, again, very good and slightly better than the cold case, with an average of **[   ]ᵃ,ᶜ**. The maximum absolute difference is also slightly better with a value of **[   ]ᵃ,ᶜ**.

The HFP results for cases with control rods inserted are also displayed in Figure 4-23 for zero burnup. The fuel temperature in these cases is 900 K, while the temperature of the other assembly regions (clad, moderator, etc.) is set to 600 K. The results for these HFP cases are good. The maximum absolute difference is **[   ]ᵃ,ᶜ**, with an average of **[   ]ᵃ,ᶜ**. **[**

]ᵃ,ᶜ

For all enrichments, the assemblies described above were depleted up to **[   ]**^{a,c} using SERPENT2 and PARAGON2. Figure 4-24 through Figure 4-29 contains the comparisons of the reactivity as a function of burnup. Each figure has four plots corresponding to the enrichments considered. The y-axis of these figures gives the delta ($\delta_k = k_\infty^{P2} - k_\infty^{S2}$) in pcm between PARAGON2 and SERPENT2. All the calculations used the elastic asymptotic scattering model.

For all burnup points of all cases, the absolute average difference between SERPENT2 and PARAGON2 is **[   ]**^{a,c} with a maximum standard deviation of **[   ]**^{a,c}. The maximum absolute difference obtained is **[   ]**^{a,c}. Combining all the assembly cases and all enrichments, the statistics for all the runs are given in Figure 4-30 for all the burnup points. Overall, the results in Figure 4-30 are very good with an average difference of only **[   ]**^{a,c}. The statistical two-sample t-test null hypothesis was also performed to compare PARAGON2 and SERPENT2 distributions (test of mean difference = 0). The P-value obtained is **[   ]**^{a,c}, indicating that there is not a statistically significant difference between the two results at the 95% confidence level. Therefore, this analysis confirms that PARAGON2 can reproduce the Monte Carlo continuous energy neutron multiplication factors with the desired accuracy **[   ]**^{a,c} on average.

The analyses performed show that the power distribution comparison between PARAGON2 and SERPENT2 is similar **[**

]^{a,c} For both assemblies, the maximum absolute difference between PARAGON2 and SERPENT2 is **[   ]**^{a,c}, with a maximum standard deviation of **[   ]**^{a,c}. Overall, the differences seen **[   ]**^{a,c} are very similar **[   ]**^{a,c}. Thus, the same conclusion applies here and again the predictions of PARAGON2 are remarkably very good and very consistent **[   ]**^{a,c}.

Table 4-1: Numerical Benchmarks – Reactivity Comparison of PARAGON2 and SERPENT2 At Zero Burnup

a,b,c

a,b,c

a,b,c

a,b,c

a,b,c
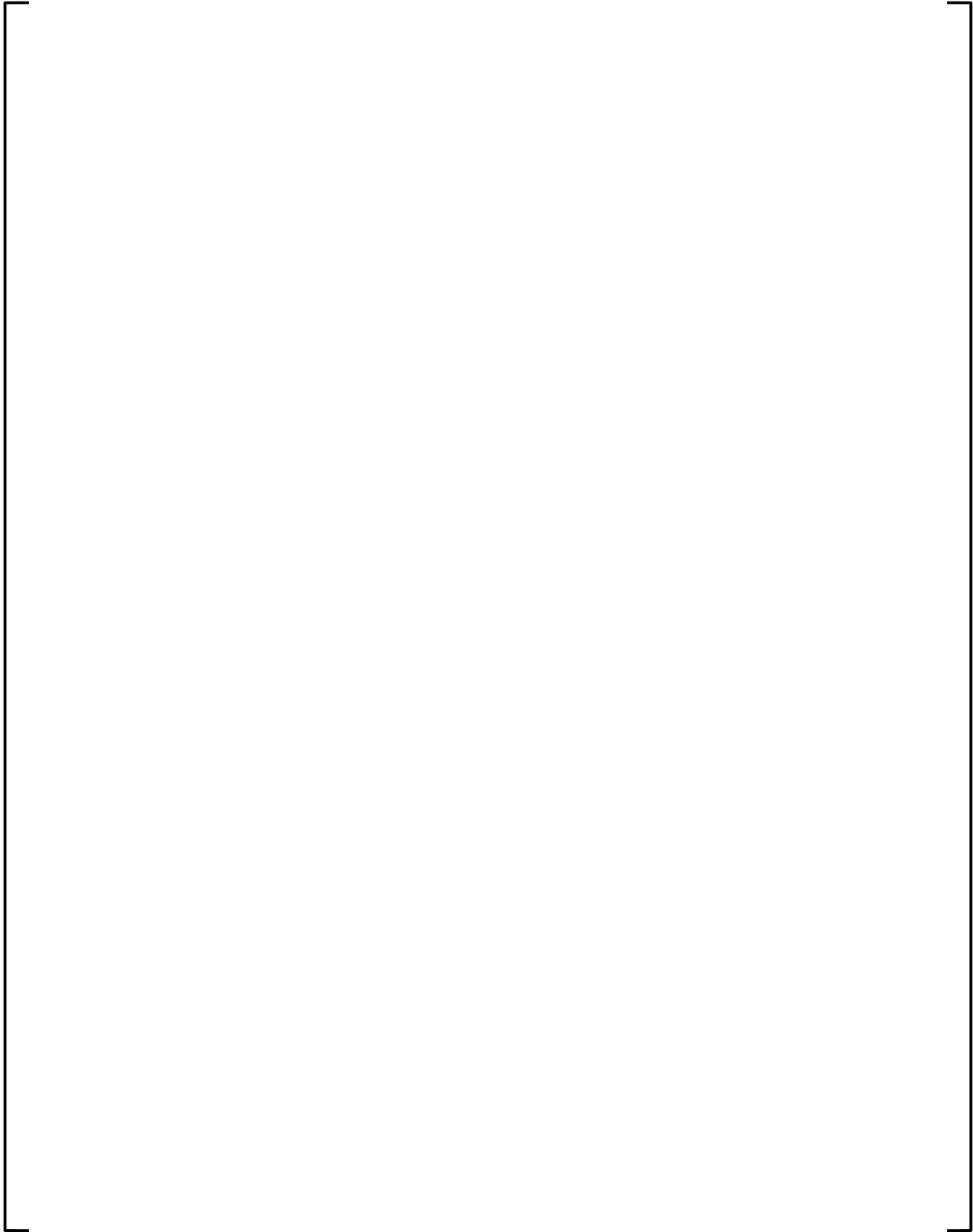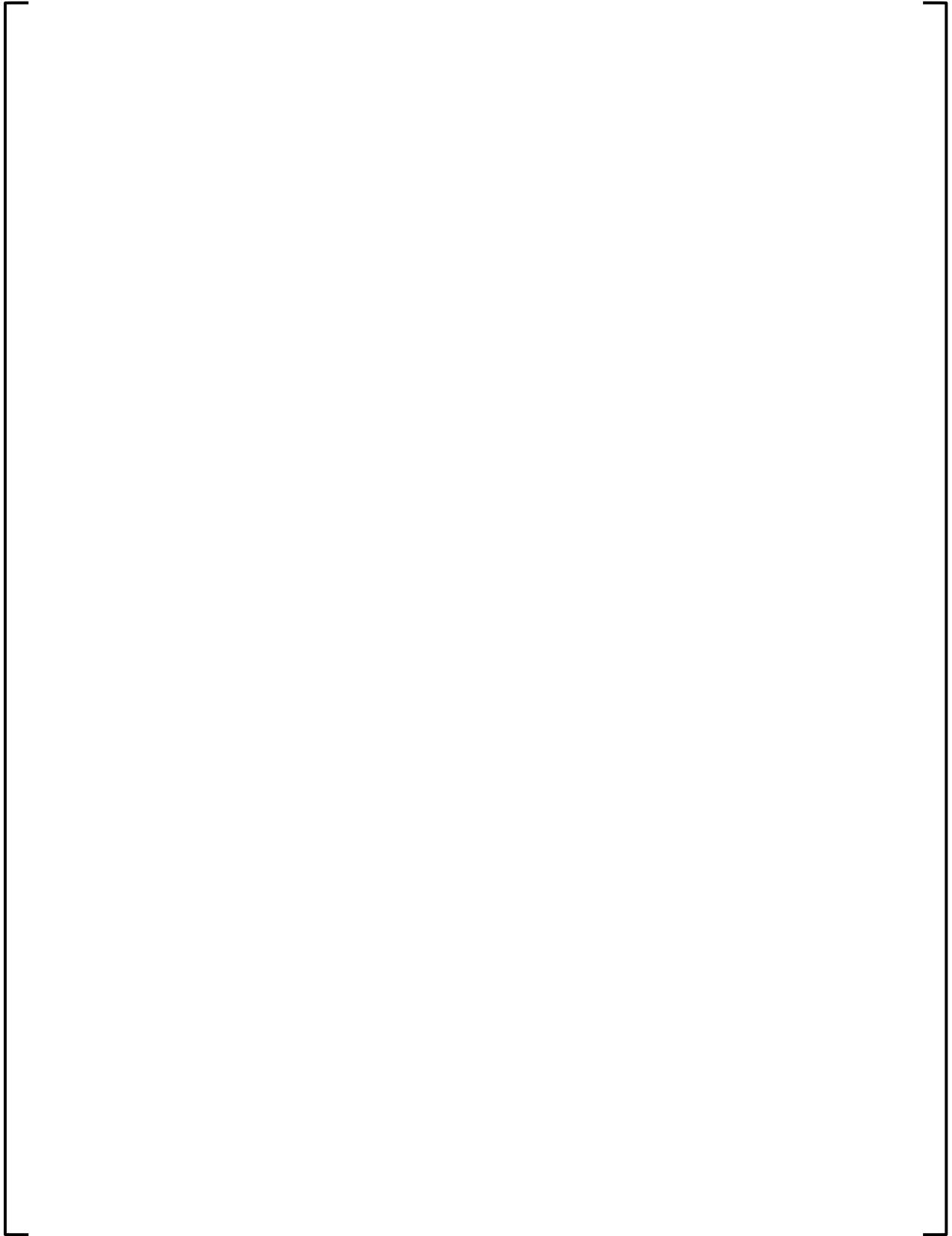
a,b,c
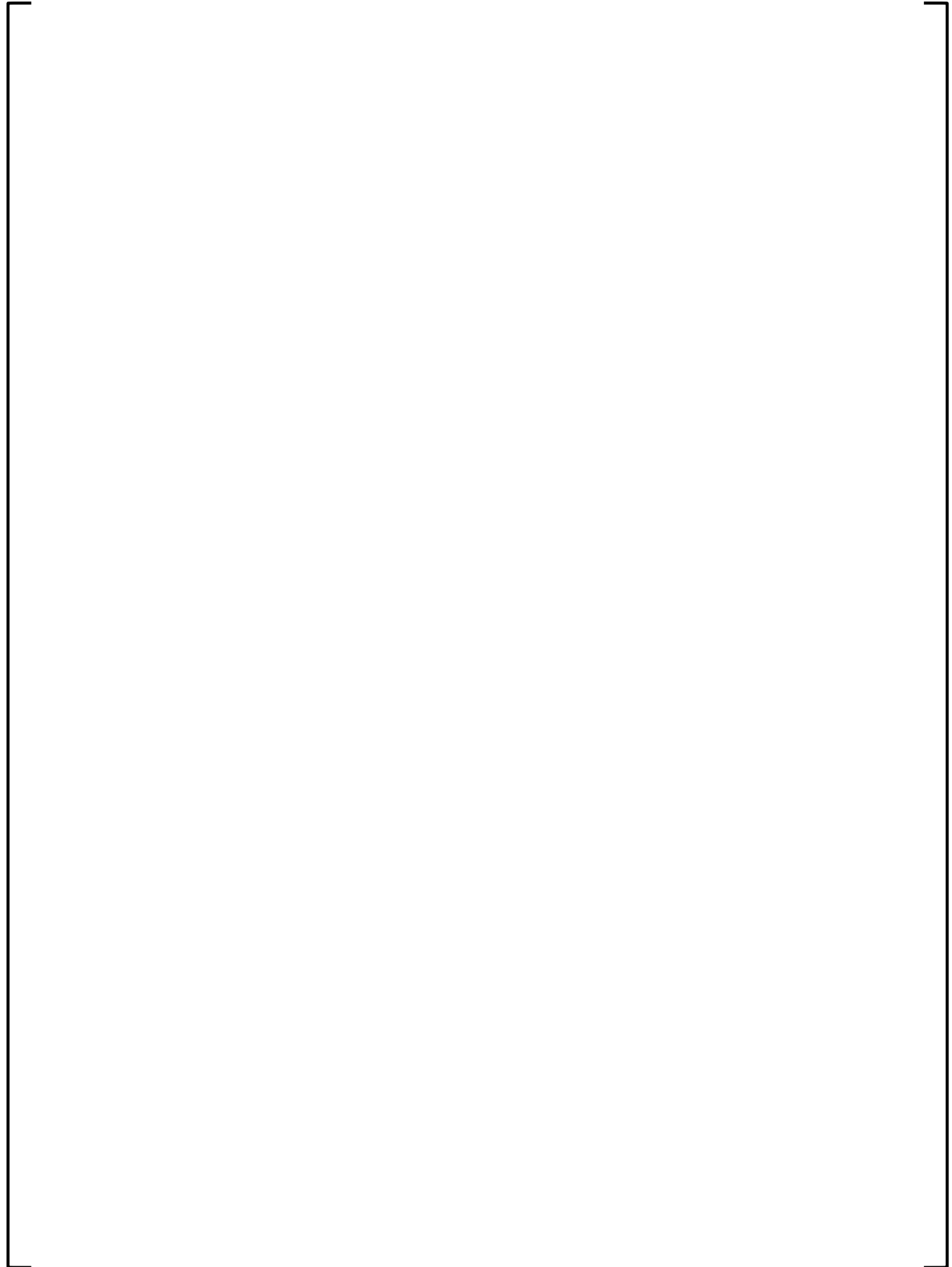
a,b,c

a,b,c

Figure 4-11: Summary of k$_{inf}$ Differences between PARAGON2 and SERPENT2

a,b,c

a,b,c

a,b,c

a,b,c

a,b,c

a,b,c

a,b,c

a,b,c
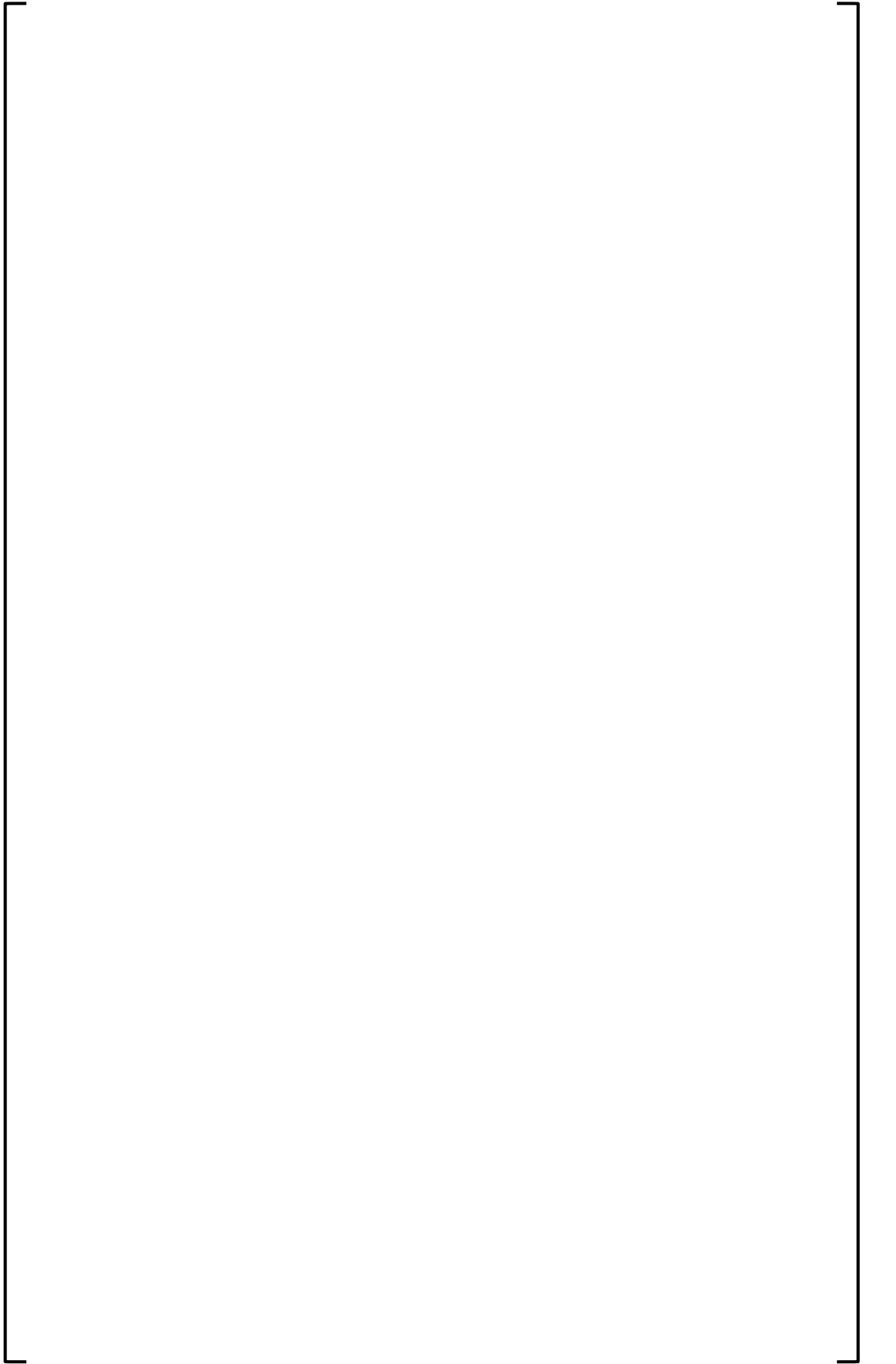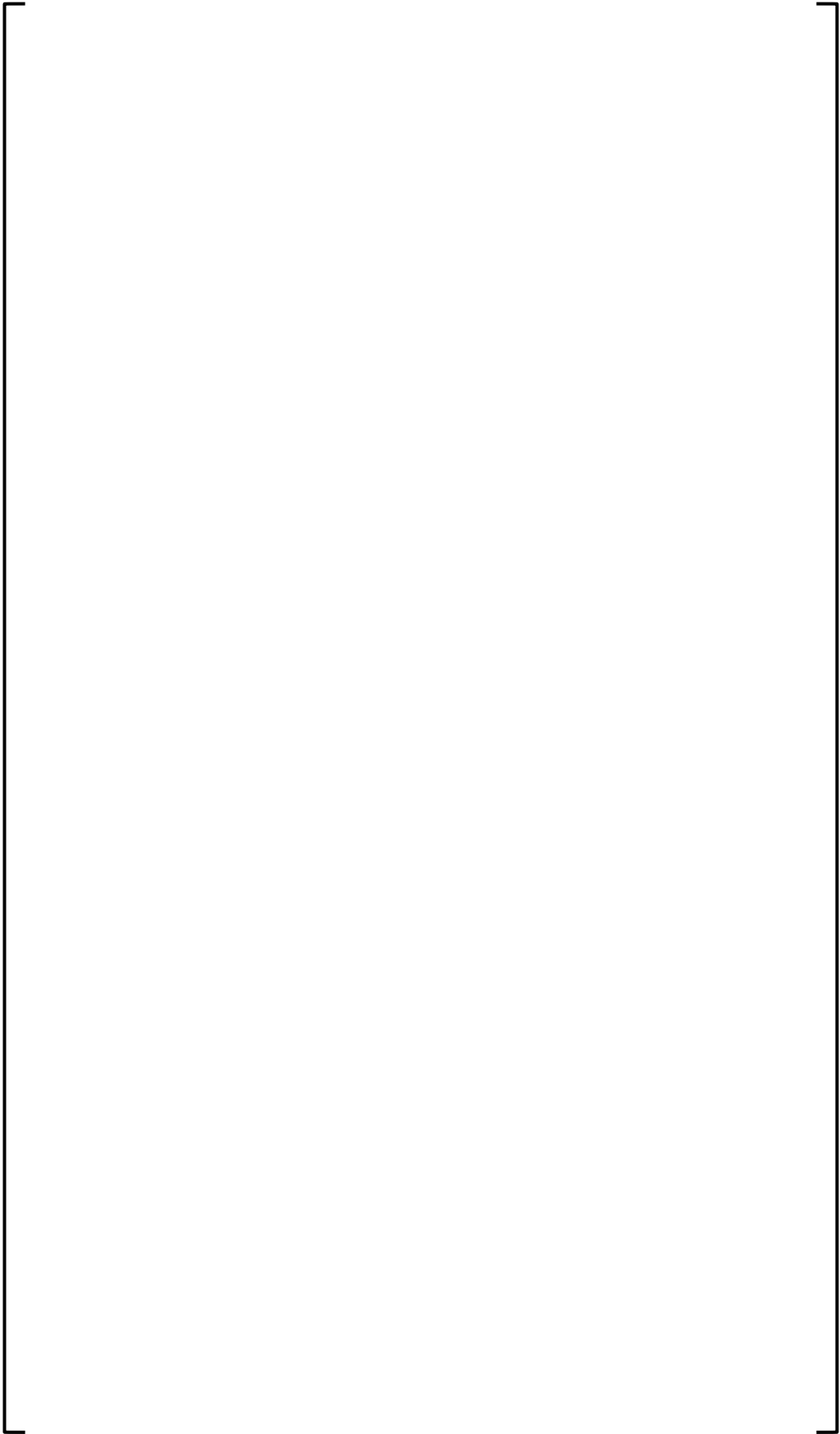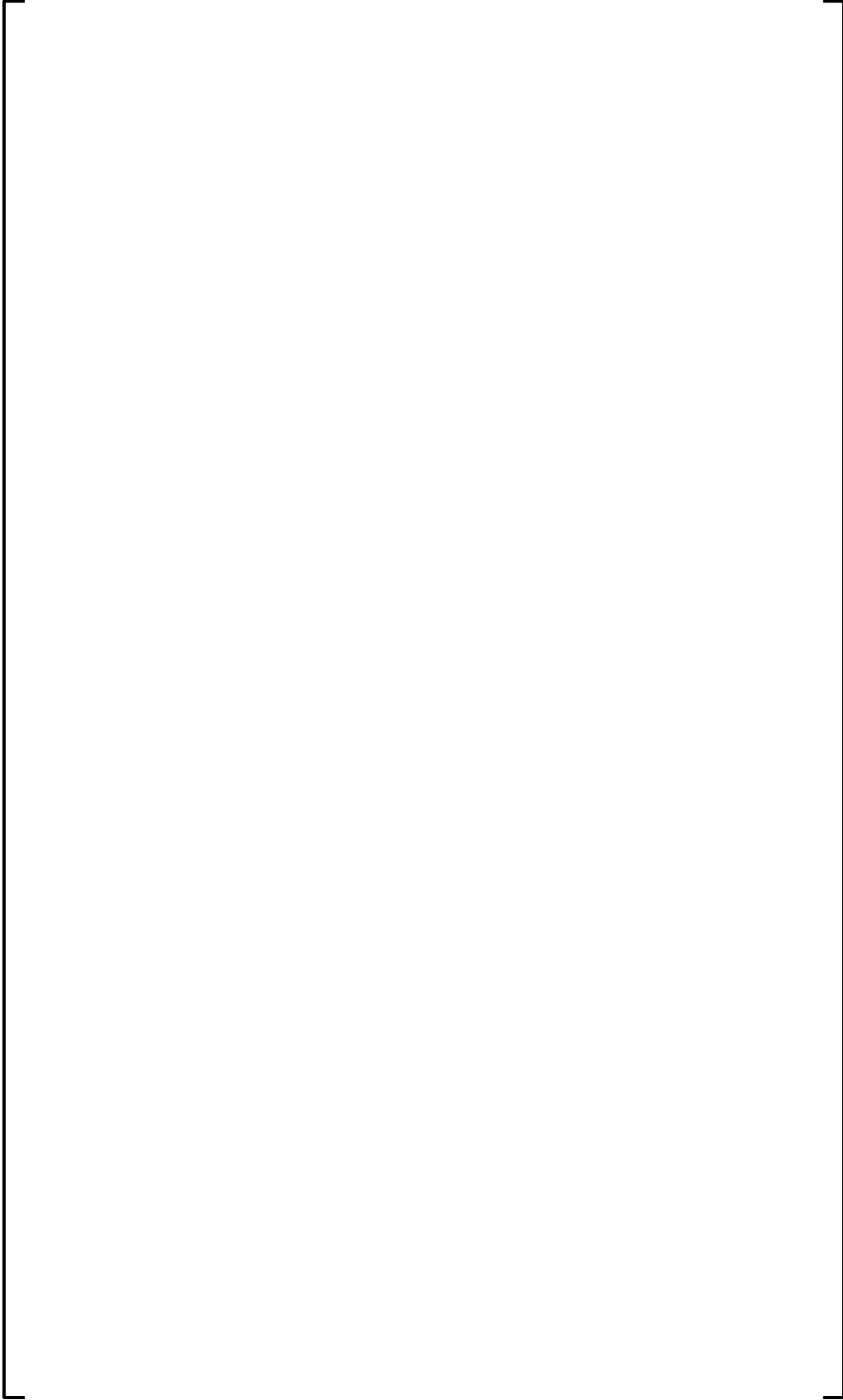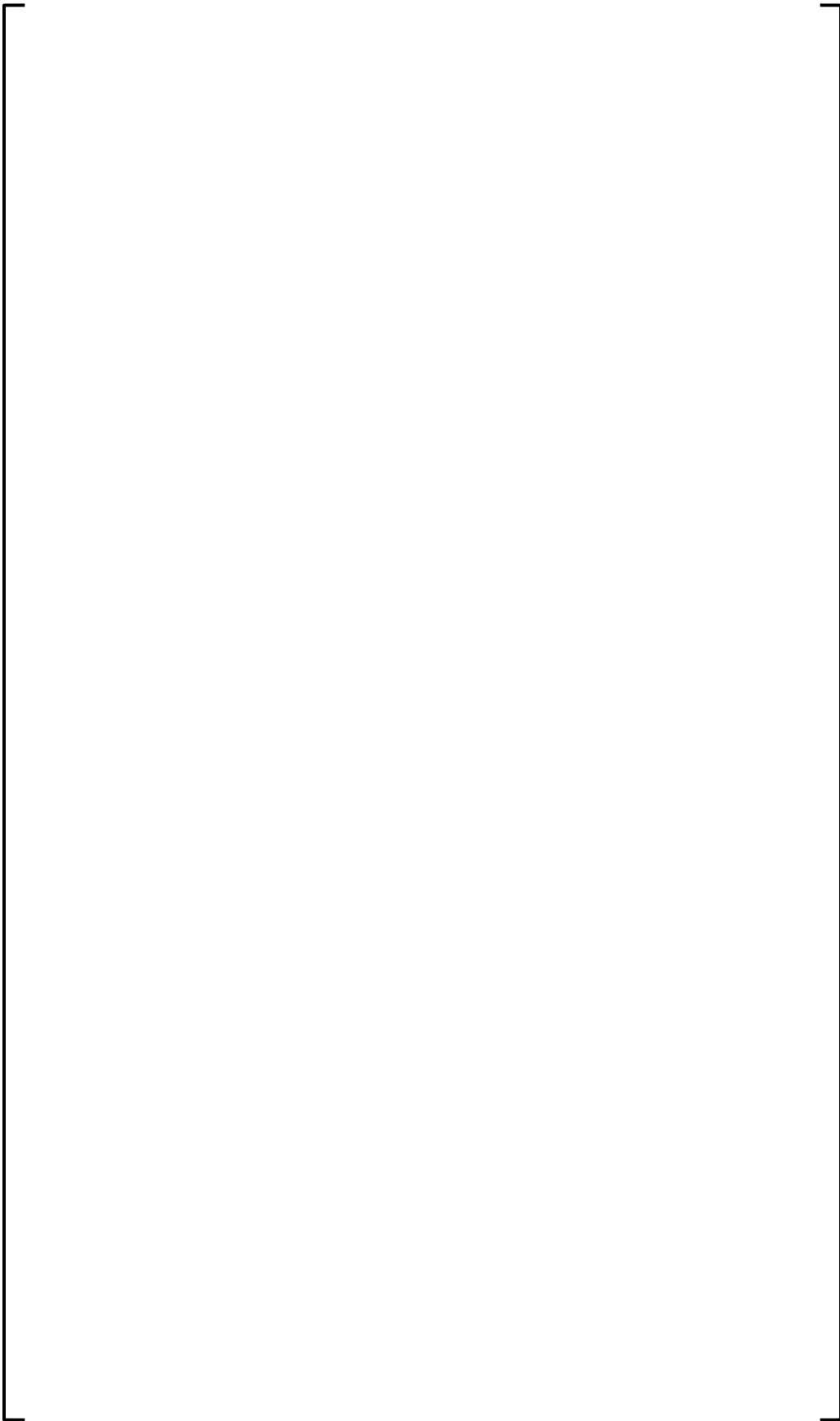
a,b,c

a,b,c
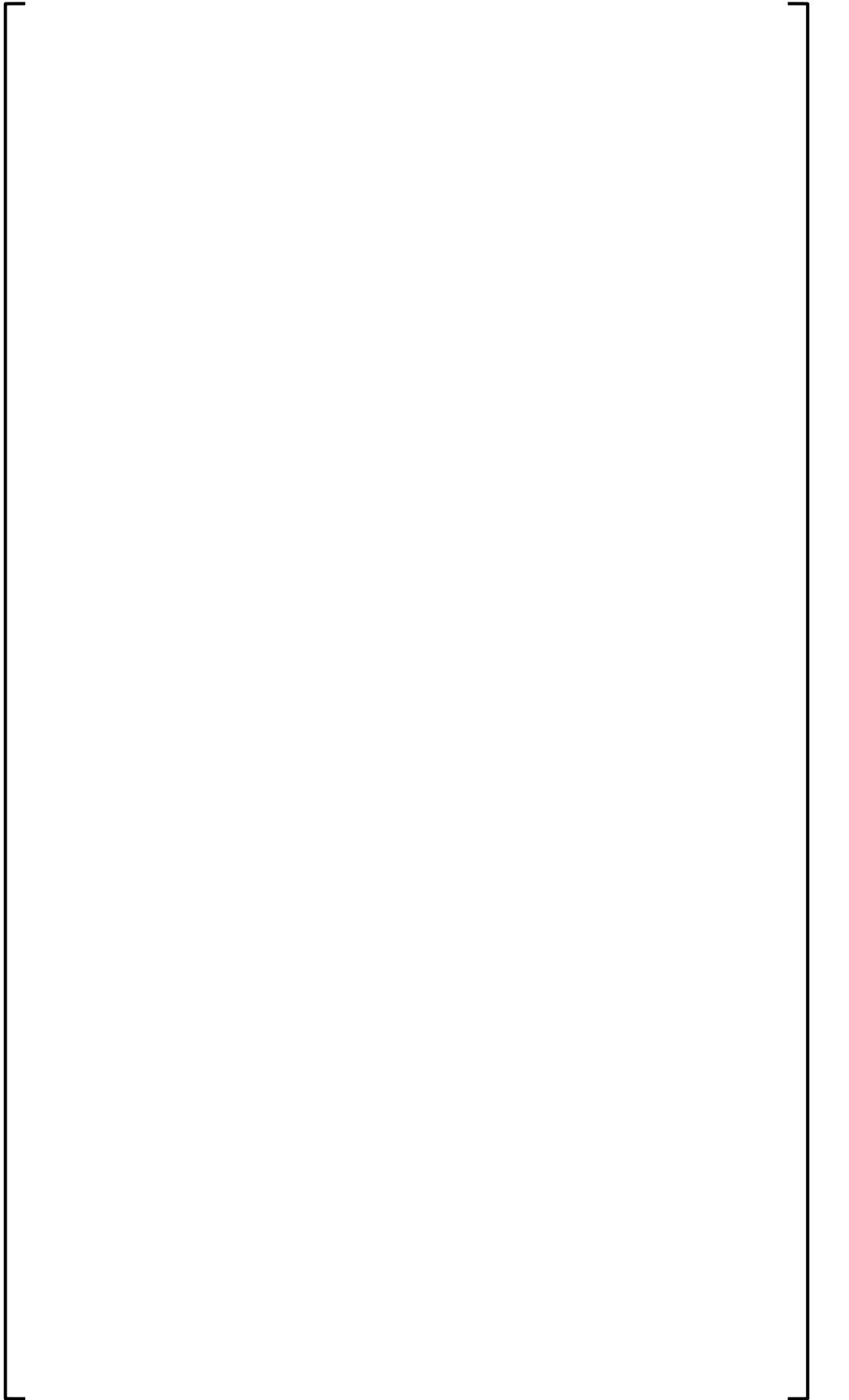
a,b,c
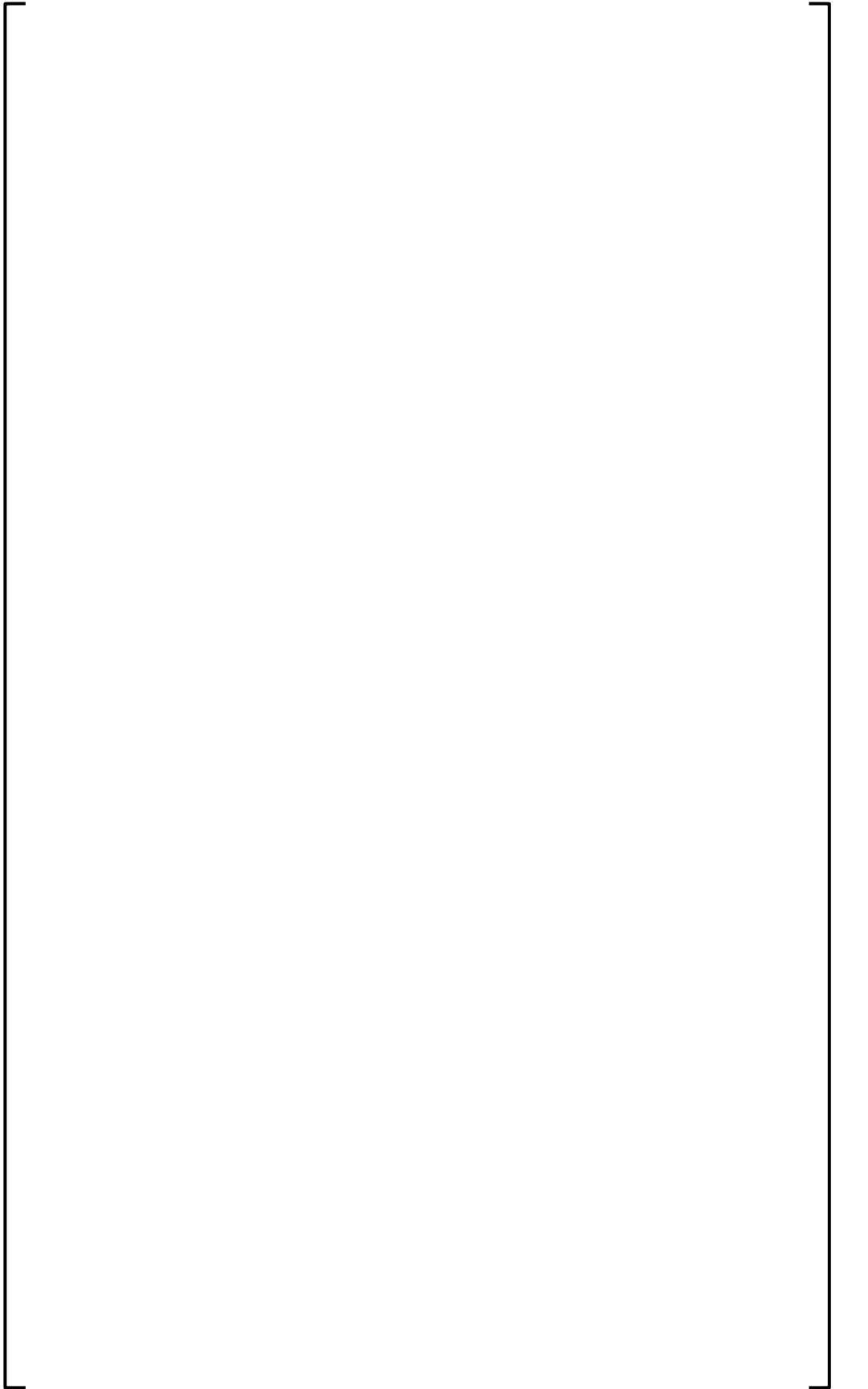
Figure 4-22: Summary of Pin Power Distributions

a,b,c

a,b,c

a,b,c
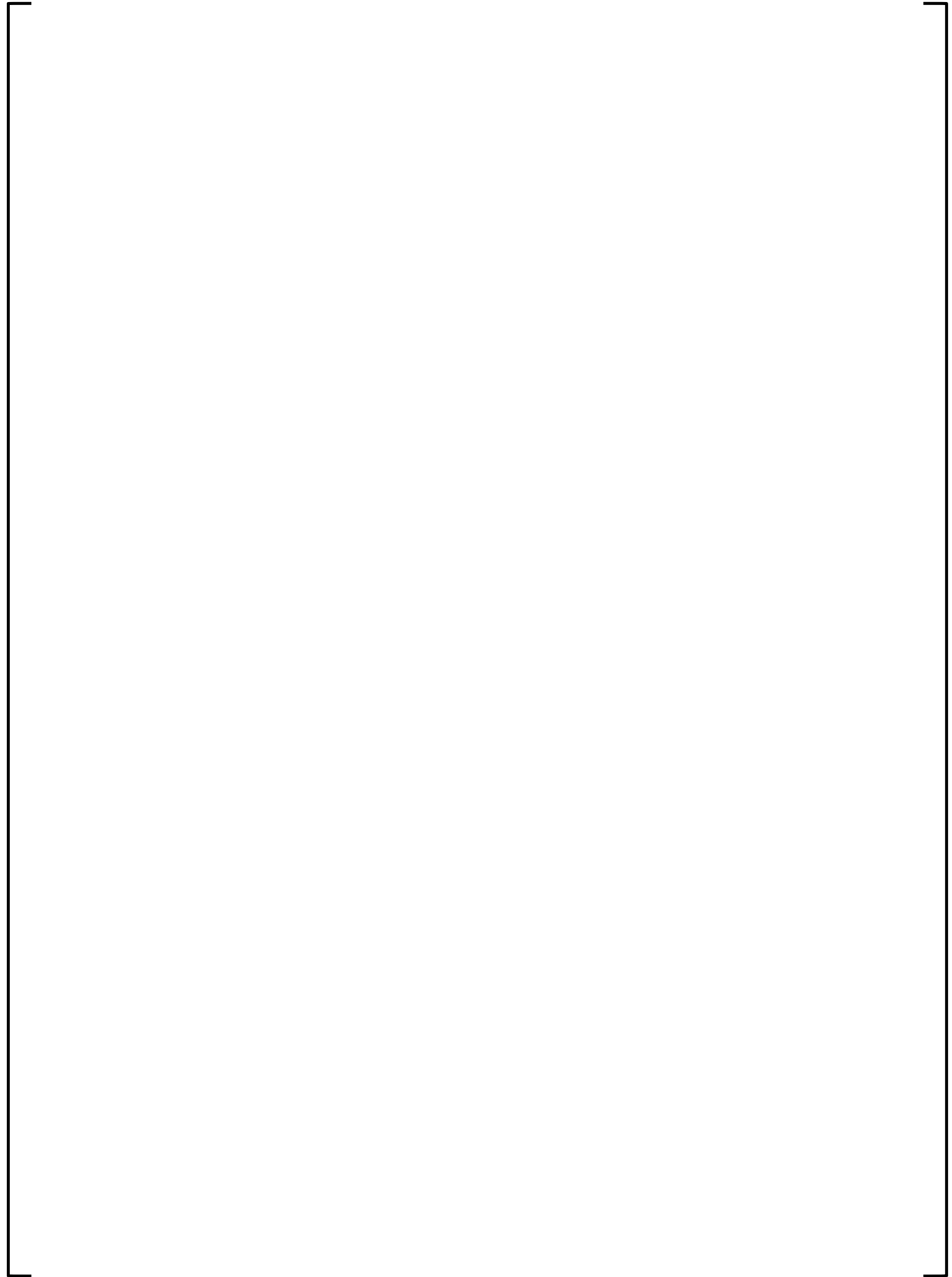
a,b,c
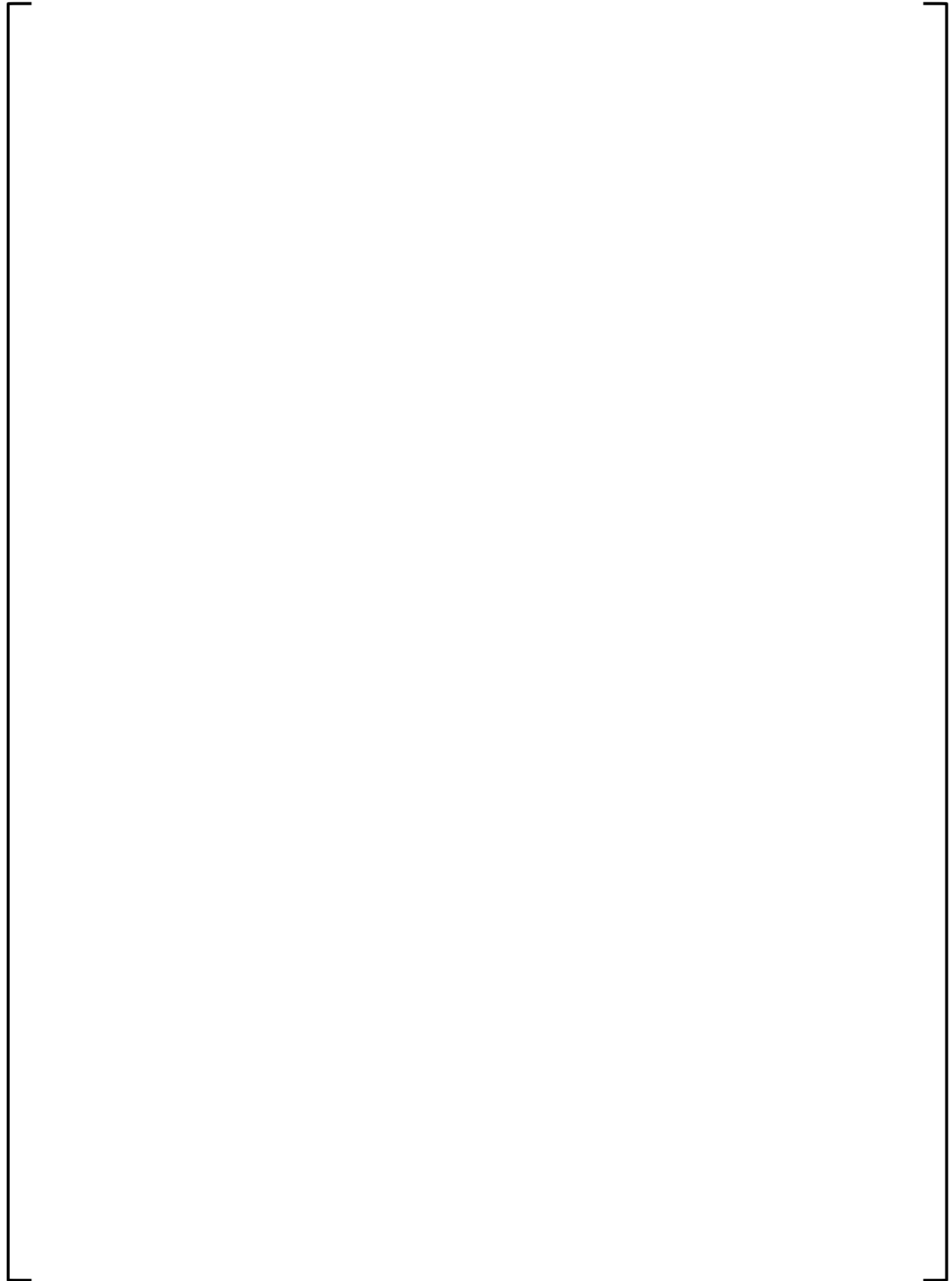
a,b,c
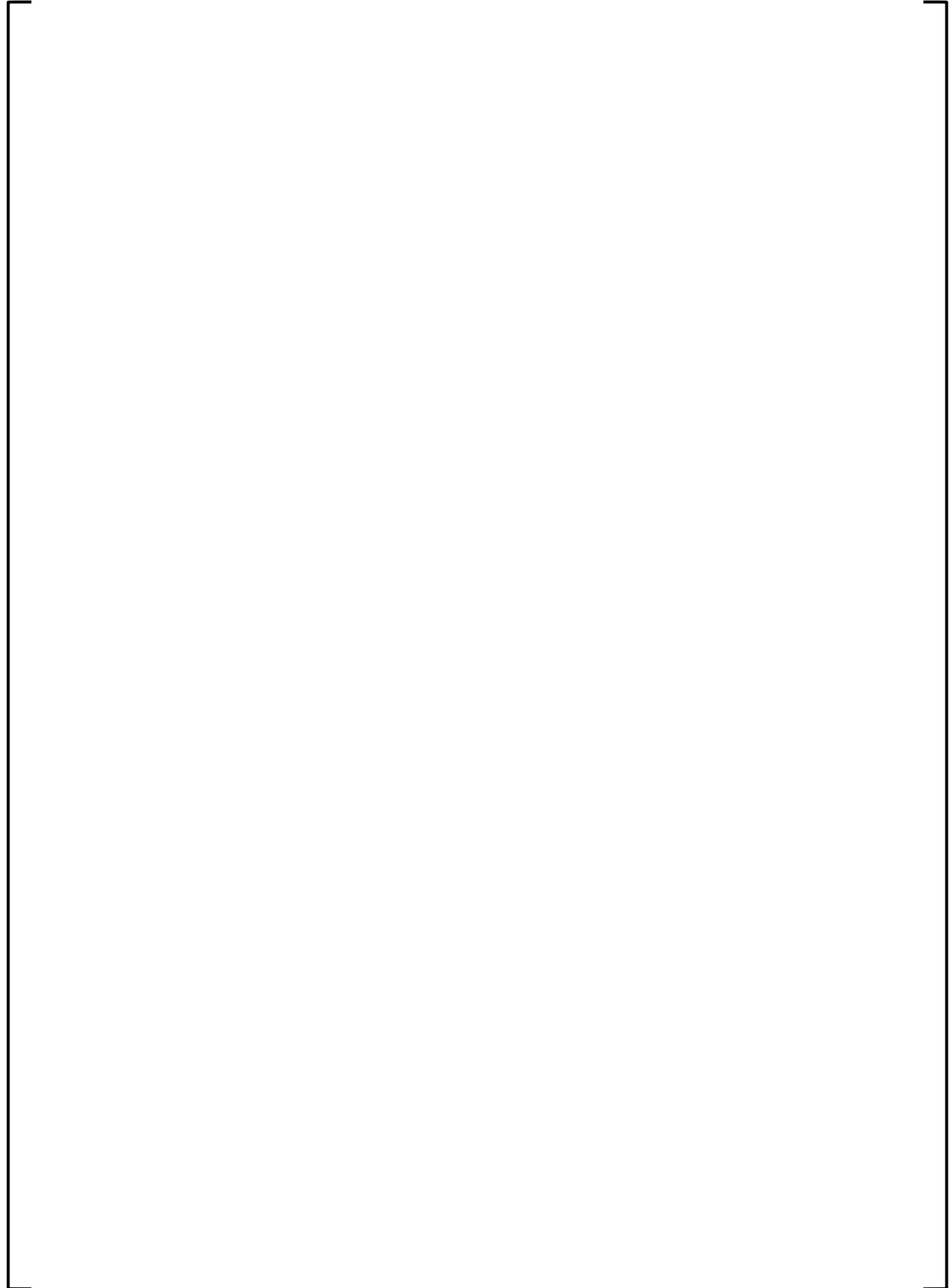
5 PLANT QUALIFICATION

5.1 INTRODUCTION

The PARAGON2 results discussed in the prior sections demonstrated the accuracy of the code in predicting the results of critical experiments and isotopic evaluations. However, the primary use of PARAGON2 will be to generate nuclear data for use in various core simulators. Thus, the most important qualification for PARAGON2 is a comparison between plant measurements and core simulation results based on PARAGON2 nuclear data.

This section discusses the ANC [20] results for PWR core calculations with nuclear data supplied by PARAGON2. Comparisons are made between PARAGON2/ANC results and their corresponding plant measurements where available or PARAGON/ANC results for the same calculations to demonstrate throughout this section and Appendices A-N the accuracy and predictability of PARAGON2/ANC. Plant cycle data are contained within Appendices A-N and are summarized in this section. The RSM is used for all results presented in this section.

The following sections are summarized below:

- Section 5.2 provides a detailed description of the plant cycles that were considered in the comparison between PARAGON2/ANC and plant measurement or PARAGON/ANC when measurement data is unavailable.

- Section 5.3 provides a detailed analysis of the comparison of PARAGON2/ANC to plant measurement for parameters that are considered for Startup Physics Testing: ARO HZP BOC ITC, ARO HZP critical boron concentrations, and total control rod worth. Additionally, Doppler Power Coefficients are provided as part of the Combustion Engineering startup test program for the Combustion Engineering plants (Plants J, M, and N) to further demonstrate the applicability of the RSM used within PARAGON2.

- Section 5.4 provides a detailed analysis of the comparison of PARAGON2/ANC to plant measurement for HFP critical boron concentration as a function of burnup and the HFP radial assembly average power distributions and HFP axial power distributions for BOC, MOC, and EOC for a given subset of plants. Also, Section 5.4 provides a detailed confirmation of the Westinghouse uncertainties approved in Ref. [17].

- Section 5.5 provides a detailed analysis of the comparison of PARAGON2/ANC to PARAGON/ANC for safety type calculations such as Steam line Break (i.e. Shutdown Margin), dropped rod, and rod ejection calculations for a given subset of plants. Moreover, Section 5.5.1 provides a detailed analysis of the comparison of PARAGON2/ANC to PARAGON/ANC and plant measurement for near EOC MTC.

5.2   DESCRIPTION OF PLANT CYCLES USED FOR COMPARISONS

The approach to choosing a representative set of plants was to encompass a wide variety of plants designs as it relates to plant vendor, fuel lattice types, burnable absorber types, and fuel rod dimensions. The key representative set must cover the following criteria:

$$\left[\right]^{a,c}$$

Table 5-1 contains a comprehensive list of the variety of plant designs and their associated plant and fuel features that provide a representative data set for the qualification of PARAGON2. In addition, Table 5-2 through Table 5-15 catalog the plant cycles, types of RCCAs, burnable absorbers, and fuel pellets used, enrichment range, and cycle length for each cycle considered for this report. As an aside, the representative set contains several data points that represent Cycle 1 data to demonstrate the accuracy of PARAGON2 in a first cycle. These cycles are accommodated with more Cycle 1 data in Ref. [44]. For use in benchmarking the results, Table 5-16 contains a list of acceptance criteria that define the applicability of PARAGON2 based results.

Not all cycles are used for every type of calculation performed in this report. A particular cycle may not be used in a particular calculation because of a lack of a complete data set or demonstrated anomalous behavior correlated to known measurement error. For comparisons against PARAGON/ANC calculations, a representative subset of the plants shown in Table 5-1 was used. In all calculations, the particular cores being used for that calculation are clearly identified.

The large data set chosen for this qualification serves two purposes: 1) it demonstrates the robustness of PARAGON2 and its library to analyze over a large range of cycle designs, and 2) it serves to qualify PARAGON2 to analyze each feature by direct comparison of results.

5.3   STARTUP TEST RESULTS COMPARISONS

Three common tests are performed during PWR startups to demonstrate the accuracy of predictions to plant measurements: ARO HZP critical boron concentration, ARO isothermal temperature coefficient, and HZP rod worth measurements with exception for some CE reactor cores where an additional measurement is taken for Doppler Power Coefficient. These measurements are taken in the just-loaded core at zero power critical conditions. This eliminates complexities, which come into play in analyzing a core at power, including the depletion power history, feedback effects and B-10 depletion, which are not yet present. Thus, these tests provide a good measure of the accuracy of the code system since the core conditions are well defined and can be simulated with high reliability in the ANC code.

For each of the aforementioned startup physics testing parameters, Table 5-17 through Table 5-20 list the results for the plants listed in Table 5-1. Each table lists the mean, standard deviation, number of data points (otherwise known as observations), minimum value, maximum value, and 95/95 one-sided tolerance limits (where applicable) for each plant and their combined contribution for the measured-minus-predicted results. For plant cycle specific information, Appendices A through N list the PARAGON2/ANC and measurement results used in the calculations.

The comparison of HZP ARO critical boron concentrations between PARAGON2/ANC and plant measurement is listed in Table 5-17. The mean and standard deviation of the measured-minus-predicted differences show good agreement. In addition, the 95/95 one-sided tolerance limit is within the listed acceptance criterion for HZP ARO critical boron concentration in Table 5-16. The conversion from units of ppm to pcm was done by applying a conservative **[   ]ᵃ,ᶜ** boron worth multiplier to the 95/95 one-sided tolerance limit for ppm differences. The boron worth multiplier conservatively bounds the actual boron worths for each plant type at startup conditions.

The comparison of HZP ARO ITC values between PARAGON2/ANC and plant measurement is listed in Table 5-18. The mean and standard deviation of the measured-minus-predicted differences show good agreement. In addition, the 95/95 one-sided upper tolerance limit is within the listed acceptance criterion for HZP ARO ITC in Table 5-16.

The comparison of HZP total rod worths between PARAGON2/ANC and plant measurement is listed in Table 5-19. The mean and standard deviation of the measured-minus-predicted differences show good agreement. In addition, 95/95 one-sided tolerance limit is within the listed acceptance criterion for HZP total rod worth in Table 5-16.

The comparison of the Doppler Power Coefficient between PARAGON2/ANC and plant measurement is listed in Table 5-20. The mean and standard deviation of the measured-minus-predicted differences show good behavior when compared to measurement.

5.4   HFP DEPLETION AND RADIAL POWER DISTRIBUTION COMPARISONS

Along with providing accurate predictions for the use in HZP startup physics testing, the core must be evaluated at HFP conditions and throughout cycle life as well. To evaluate the accuracy of PARAGON2 in HFP conditions, global core reactivity and radial and axial power distributions are compared.

For HFP core reactivity tracking, a statistical analysis was performed on PARAGON2/ANC measured-minus-predicted differences for HFP critical boron concentrations as a function of burnup for each plant and their corresponding cycles as listed within Appendix A through Appendix N. The measured-minus-predicted differences for a given plant were analyzed as a single data set and on a per-cycle basis. The evaluation of the whole data set and as a per-cycle basis is to establish the accuracy of PARAGON2 based nuclear data on a global and microscopic scale. Table 5-21 contains the combined statistics for all the measured-minus-predicted differences across each of the plant cycles listed in Table 5-2 through Table 5-15. For HFP conditions, many factors could drive the boron measured-minus-predicted differences to exceed [   ]ᵃ,ᶜ, among these factors the unknown B-10 depletion assay, the exact core power level, or the approximated power history especially for early initial cycles.

From reviewing the HFP critical boron concentration statistics, the following conclusions can be determined from Table 5-21 and Appendices A through N:

1. PARAGON2/ANC shows good agreement with plant measurement. For a variety of fuel characteristics, cycle lengths, plant types, PARAGON2/ANC still predicts core behavior reasonably well and within the acceptance criteria provided in Table 5-16. This demonstrates that PARAGON2 provides accurate plant predictions for a wide variety of plant conditions and core features. The 95/95 one-sided tolerance limit was determined using non-parametric statistics. The conversion from units of ppm to pcm was done by applying a conservative [   ]^{a,c} boron worth multiplier to the 95/95 one-sided tolerance limit for ppm differences. The boron worth multiplier conservatively bounds the actual boron worths for each plant type at full power operating conditions.

2. Some plant cycles present evidence of significant B-10 depletion, but the B-10 depletion data was not available to correct the measured-minus-predicted comparisons. The measured-minus-predicted boron concentrations for Plants A and N demonstrate the effect of not correcting for B-10 depletion. The larger measured-minus-predicted differences can be attributed to the lack of B-10 depletion when compared to the rest of the data set, which do consider B-10 depletion.

The full core radial power distributions were compared for a subset of plants to demonstrate the accuracy of PARAGON2/ANC: Plants D Cycle 28, F Cycle 30, and H Cycle 22. The radial power distribution comparisons are listed in Appendix D, F, and H for the selected plants. From the radial power distribution, the following conclusions can be determined:

1. Among the subset of plants that have radial power distribution comparisons, the root-mean-square deviation for measured-minus-predicted differences show good results.

2. Additionally, radial and total peaking factors ($F_{\Delta H}$, F_Q) standard deviations demonstrate good agreement to measurement and are within the acceptance criteria listed in Table 5-16. The methodology for developing the peaking factor uncertainties is based on the methodology used in Ref. [17]. [

                                                                                    ]^{a,c} The radial peaking factor uncertainty is a combination of the total standard deviation of the radial power distributions and the total standard deviation of the critical experiments outlined in Section 3. The total peaking factor uncertainty consists of the radial peaking factor components plus the combined standard deviation of the axial power distributions. Table 5-22 through Table 5-24 contain the standard deviations for each uncertainty component.

The following equations define the peaking factor uncertainties as defined by Ref. [17]:

$$\begin{bmatrix} & & \\ & & \\ & & \\ & & \\ & & \end{bmatrix}^{a,c}$$

The combination of uncertainties outlined in Ref. [17] and previously listed assumes independence about the uncertainty components and normality. The 95/95 one-side tolerance limit is calculated the same as in Ref. [17] with a multiplier of **[   ]a,c** about the combined standard deviation.
**[

]a,c** The results of the Monte Carlo sampling show the methods outlined in Ref. [17] are applicable for the confirmation of the Westinghouse peaking factor uncertainties.

Considering a 95/95 one-sided tolerance limit, the radial and total peaking factor uncertainties described in Ref. [17] bound the radial and total peaking factor uncertainties calculated by PARAGON2/ANC for the given subset of plants with the equations above. The results are listed in Table 5-16.

Core-wise axial power distributions for key times in life are presented for a select subset of plants to demonstrate the accuracy of PARAGON2/ANC compared to plant measurement: Plant D Cycle 28, F Cycle 30, and H Cycle 22. The axial power distributions are listed in Appendix D, F, and H. After reviewing the axial power distributions, the axial power profile is accurately depicted using PARAGON2/ANC.

5.5 PARAGON/ANC VERSUS PARAGON2/ANC COMPARISONS

The PARAGON/ANC nuclear code system has been licensed by the NRC since 2004 and has had extensive use in PWR safety and design calculations [41]. As part of the qualification of PARAGON2, comparisons have been made between the results of core calculations of the two systems to demonstrate predictive capability of PARAGON2/ANC for operating PWR cores to the same or better accuracy. Thus, any uncertainties or biases appropriate for PARAGON/ANC are also appropriate for PARAGON2/ANC. In this section, comparisons are made between PARAGON/ANC and PARAGON2/ANC results for the steamline break rod worths and peaking factors, dropped rod worths and peaking factors, EOC HFP ARO MTC, and ejected rod worths and peaking factors.

For each parameter, the following plants were selected to act as a representative set of the whole set outlined in Table 5-1: Plant D Cycles 26 and 27, Plant F Cycles 29 and 30, Plant G Cycles 11 and 12, and Plant H Cycles 20 and 21. The comparisons for the aforementioned plant cycles are made in Table 5-26 through Table 5-29.

The calculations comparing the ARI worth minus the worth of the highest worth stuck control rod (called the worst stuck rod or WSR) were performed in full core geometry at BOC HZP conditions. These calculations are of interest for confirming plant shutdown margin and contribute to input used in the steam line break accident scenario. The WSR configuration peaking factors (F_Q, $F_{\Delta H}$, and F_Z) are also compared since these results may be of interest in the calculation of steam line break or other accident power distributions.

Table 5-27 summarizes the results of the steam line break related parameters, ARI-WSR and peaking factors, for the aforementioned plant cycles for both code systems. It can be concluded from the results that PARAGON2/ANC show similar results to PARAGON/ANC.

The calculations for the dropped rod scenario are performed at HFP EOC conditions in full core geometry with all the rods out of the core (ARO). Then, each control rod will be dropped to the ARI position and the maximum among all the control rods is considered the limiting condition. The parameters of interest for this calculation are the same as the ARI-WSR calculations which are the dropped rod worth, total peaking factor (F_Q), nuclear enthalpy rise hot channel factor ($F_{\Delta H}$), and axial peaking factor (F_Z).

Table 5-28 summarizes the results from EOC dropped rod calculations for the aforementioned plant cycles with PARAGON/ANC and PARAGON2/ANC. It can be concluded from the results that PARAGON2/ANC show similar results to PARAGON/ANC.

The calculations for the rod ejection event are performed at BOC and EOC for both HFP and HZP conditions. The control rods are placed at their respective control rod insertion limits and are ejected instantaneously. To capture the instantaneous nature of the event, all feedback effects are frozen to the pre-ejection condition. The parameters of interest for rod ejection are the ejected rod worth and total peaking factor (F_Q).

Table 5-29 summarizes the results for the rod ejection event for the aforementioned plant cycles with PARAGON/ANC and PARAGON2/ANC. It can be concluded from the results that PARAGON2/ANC show similar results to PARAGON/ANC.

5.5.1   Near EOC MTC Plant Measurement

At EOL, one of the key safety analysis input parameters is the most positive MDC / most negative MTC. The MDC values used in the safety analysis are based on predictions which are confirmed to remain conservative by performing the near-EOL Moderator Temperature Coefficients (MTC) surveillance at approximately 300 ppm and HFP conditions.

Several benchmark plant/cycles were selected for comparison of the near EOL MTC predictions to plant measurement data: Plant B Cycles 17-21, Plant G Cycles 11-15, and Plant H Cycle 21. These cycles were chosen to cover a broad range of PWR core characteristics such as cycle length, power density, neutron spectrum, and fuel lattice types. The plants selected also cover a variety of at-power MTC measurement techniques currently used by the industry. Thus, the set of benchmarks chosen represents a good unbiased sample of the larger data set used in Reference [5]. The measured versus predicted PARAGON2/ANC results are provided in Table 5-25 and show good agreement between measurement and prediction, consistent with the results previously reported in Reference [5].

Along with plant measurement, a comparison between PARAGON/ANC and PARAGON2/ANC is shown in Table 5-26. The plant cycles that were evaluated were the following: Plant D Cycles 26 & 27, Plant F Cycles 29 & 30, Plant G Cycles 11 & 12, and Plant H Cycles 20 & 21 (See Section 5.5). The good agreement between PARAGON2/ANC and PARAGON/ANC demonstrate that the implementation of PARAGON2/ANC would not introduce any additional uncertainty and/or bias in performing a near EOC measurement and EOL MTC predictions with accuracy consistent with the previously approved PARAGON/ANC methodology.

Additionally, the predictive correction term defined in Reference [5] was set as a tolerance limit based on the difference between measured-to-predicted BOC HZP MTC values. Following the same definition in Reference [5], the HFP predictive correction term for PARAGON2/ANC combines the HZP BOC ITC predictive correction and HFP xenon and burnup sensitivities. Based on the HZP BOC ITC statistics listed in Table 5-18, the HZP predictive correction term is **[**

]a,c and is representative of the 95/95 upper CI. Combined with the sum of the HFP xenon and burnup sensitivities of **[**   **]a,c** (Reference [5]), the predictive correction term using PARAGON2/ANC is **[**   **]a,c**, which is nearly identical to the PHOENIX-P/ANC calculated HFP predictive correction of **[**   **]a,c** from Reference [5]. Therefore, the current HFP predictive correction value of **[**   **]a,c** from Reference [5] will continue to be used with PARAGON2/ANC.

The results presented in this section demonstrate that PARAGON2/ANC can predict accurately the near EOC MTC measurement. Additionally, the data presented in Table 5-25 lie within the population established in Reference [5]. Therefore, PARAGON2/ANC can be a direct replacement to PHOENIX-P/ANC that was used in Reference [5] and to PARAGON/ANC. Consequently, the plants with the exemption of the most negative EOL MTC measurement obtained with either PHOENIX-P/ANC or PARAGON/ANC can retain this exemption when using PARAGON2/ANC without submitting new NRC licensing requests.

Table 5-1: Benchmark Plant Description

Plant Designation	Vender	Loops	Number of Assemblies	Lattice Type	Fuel Rod Diameter (in.)
A	W	4	193	W 17x17	0.374
B	W	4	193	W 17x17	0.360
C	W	2	121	W 16x16	0.374
D	W	3	157	W 17x17	0.360
E	W	2	121	W 14x14	0.422
F	W	2	121	W 14x14	0.422
G	W	4	193	W 17x17	0.374
H	W	4	193	W 15x15	0.422
I	W	3	157	W 17x17	0.374
J	CE	2	241	CE 16x16	0.382
K	W	3	157	W 17x17	0.360
L	W	3	157	W 17x17	0.374
M	CE	2	217	CE 14x14	0.440
N	CE	2	177	CE 16x16	0.374

Table 5-2: Benchmark Cycle Details – Plant A

Cycle	RCCA Material	Burnable Absorber Type	Fuel Pellet Type	Enrichment Range (wt%)	End of Cycle Burnup (MWD/MTU)
AC1	Hf	PYREX	Solid	2.10-2.90	11,971
AC2	Ag-In-Cd	PYREX	Solid	2.10-3.60	9,447
AC3	Ag-In-Cd	PYREX	Solid	2.60-4.00	13,752
AC15	Ag-In-Cd	IFBA	Solid/Annular	2.60-4.80	19,417
AC16	Ag-In-Cd	IFBA	Solid/Annular	2.60-4.80	17,659
AC17	Ag-In-Cd	IFBA	Solid/Annular	2.60-4.60	17,247
AC18	Ag-In-Cd	IFBA	Solid/Annular	2.60-4.60	19,381
AC19	Ag-In-Cd	IFBA	Solid/Annular	2.60-4.60	18,930

Table 5-3: Benchmark Cycle Details – Plant B

Cycle	RCCA Material	Burnable Absorber Type	Fuel Pellet Type	Enrichment Range (wt%)	End of Cycle Burnup (MWD/MTU)
BC17	Ag-In-Cd	IFBA	Solid/Annular	4.20-4.95	21,709
BC18	Ag-In-Cd	IFBA	Solid/Annular	4.20-4.95	24,520
BC19	Ag-In-Cd	IFBA	Solid/Annular	4.20-4.95	22,933
BC20	Ag-In-Cd	IFBA	Solid/Annular	4.20-4.95	21,983
BC21	Ag-In-Cd	IFBA/WABA	Solid/Annular	4.20-4.95	24,240

Table 5-4: Benchmark Cycle Details – Plant C

Cycle	RCCA Material	Burnable Absorber Type	Fuel Pellet Type	Enrichment Range (wt%)	End of Cycle Burnup (MWD/MTU)
CC25	Ag-In-Cd	IFBA	Solid/Annular	2.60-4.95	21,010
CC26	Ag-In-Cd	IFBA	Solid/Annular	2.60-4.95	19,506
CC27	Ag-In-Cd	IFBA	Solid/Annular	2.60-4.95	20,385
CC28	Ag-In-Cd	IFBA	Solid/Annular	2.60-4.95	20,195
CC29	Ag-In-Cd	IFBA	Solid/Annular	2.60-4.85	20,923

Table 5-5: Benchmark Cycle Details – Plant D

Cycle	RCCA Material	Burnable Absorber Type	Fuel Pellet Type	Enrichment Range (wt%)	End of Cycle Burnup (MWD/MTU)
DC25	Ag-In-Cd	IFBA	Solid/Annular	4.20-4.60	21,361
DC26	Ag-In-Cd	IFBA	Solid/Annular	4.20-4.60	21,506
DC27	Ag-In-Cd	IFBA	Solid/Annular	4.20-4.60	21,088
DC28	Ag-In-Cd	IFBA	Solid/Annular	4.20-4.95	20,650

Table 5-6: Benchmark Cycle Details – Plant E

Cycle	RCCA Material	Burnable Absorber Type	Fuel Pellet Type	Enrichment Range (wt%)	End of Cycle Burnup (MWD/MTU)
EC36	Ag-In-Cd	IFBA	Solid/Annular	2.60-4.95	18,312
EC37	Ag-In-Cd	IFBA	Solid/Annular	2.60-4.95	19,154
EC38	Ag-In-Cd	IFBA	Solid/Annular	2.60-4.95	18,955
EC39	Ag-In-Cd	IFBA	Solid/Annular	2.60-4.95	19,749
EC40	Ag-In-Cd	IFBA	Solid/Annular	2.60-4.95	19,594

Table 5-7: Benchmark Cycle Details – Plant F

Cycle	RCCA Material	Burnable Absorber Type	Fuel Pellet Type	Enrichment Range (wt%)	End of Cycle Burnup (MWD/MTU)
FC25	Ag-In-Cd	Gadolina	Solid/Annular	2.88-4.95	20,357
FC26	Ag-In-Cd	Gadolina	Solid/Annular	2.52-4.95	19,323
FC27	Ag-In-Cd	Gadolina	Solid/Annular	2.52-4.95	17,683
FC28	Ag-In-Cd	Gadolina	Solid/Annular	2.52-4.90	22,420
FC29	Ag-In-Cd	Gadolina	Solid/Annular	2.52-4.95	21,810
FC30	Ag-In-Cd	Gadolina	Solid/Annular	2.52-4.95	24,000

Table 5-8: Benchmark Cycle Details – Plant G

Cycle	RCCA Material	Burnable Absorber Type	Fuel Pellet Type	Enrichment Range (wt%)	End of Cycle Burnup (MWD/MTU)
GC1	B$_4$C/Ag-In-Cd		a,c Solid	2.10-3.10	16,942
GC2	B$_4$C/Ag-In-Cd		Solid	2.10-3.70	18,063
GC3	B$_4$C/Ag-In-Cd		Solid/Annular	2.10-4.40	19,338
GC11	Ag-In-Cd		Solid/Annular	3.20-4.60	17,898
GC12	Ag-In-Cd		Solid/Annular	3.20-4.60	19,590
GC13	Ag-In-Cd		Solid/Annular	2.80-4.60	19,034
GC14	Ag-In-Cd		Solid/Annular	2.80-4.95	18,919
GC15	Ag-In-Cd		Solid/Annular	2.80-4.95	19,143

Table 5-9: Benchmark Cycle Details – Plant H

Cycle	RCCA Material	Burnable Absorber Type	Fuel Pellet Type	Enrichment Range (wt%)	End of Cycle Burnup (MWD/MTU)
HC19	Ag-In-Cd	IFBA/WABA	Solid/Annular	3.20-4.95	24,844
HC20	Ag-In-Cd	IFBA/WABA	Solid/Annular	3.20-4.95	23,739
HC21	Ag-In-Cd	IFBA/WABA	Solid/Annular	3.20-4.95	25,085
HC22	Ag-In-Cd	IFBA/WABA	Solid/Annular	3.20-4.95	26,024
HC23	Ag-In-Cd	IFBA/WABA	Solid/Annular	3.60-4.95	23,767

Table 5-10: Benchmark Cycle Details – Plant I

Cycle	RCCA Material	Burnable Absorber Type	Fuel Pellet Type	Enrichment Range (wt%)	End of Cycle Burnup (MWD/MTU)
IC1	Ag-In-Cd	PYREX	Solid	2.10-3.10	14,893

Table 5-11: Benchmark Cycle Details – Plant J

Cycle	CEA Material	Burnable Absorber Type	Fuel Pellet Type	Enrichment Range (wt%)	End of Cycle Burnup (MWD/MTU)
JC1	B$_4$C/Ag-In-Cd	B$_4$C	Solid	1.90-3.30	17,092

Table 5-12: Benchmark Cycle Details – Plant K

Cycle	RCCA Material	Burnable Absorber Type	Fuel Pellet Type	Enrichment Range (wt%)	End of Cycle Burnup (MWD/MTU)
KC1	Hf	PYREX	Solid	1.60-3.10	11,965

Table 5-13: Benchmark Cycle Details – Plant L

Cycle	RCCA Material	Burnable Absorber Type	Fuel Pellet Type	Enrichment Range (wt%)	End of Cycle Burnup (MWD/MTU)
LC22	B$_4$C/Ag-In-Cd	Gadolina	Solid	2.80-4.70	20,569
LC23	B$_4$C/Ag-In-Cd	Gadolina	Solid	2.80-4.70	20,350
LC24	B$_4$C/Ag-In-Cd	Gadolina	Solid	2.81-4.70	19,850

Table 5-14: Benchmark Cycle Details – Plant M

Cycle	CEA Material	Burnable Absorber Type	Fuel Pellet Type	Enrichment Range (w/o)	End of Cycle Burnup (MWD/MTU)
MC13	B$_4$C/Ag-In-Cd	Erbia	Solid	3.40-4.47	21,175
MC14	B$_4$C/Ag-In-Cd	Erbia	Solid	3.40-4.47	19,789
MC15	B$_4$C/Ag-In-Cd	Erbia	Solid	3.40-4.47	20,360
MC16	B$_4$C/Ag-In-Cd	IFBA/Erbia	Solid/Annular	2.60-4.60	22,247

Table 5-15: Benchmark Cycle Details – Plant N

Cycle	CEA Material	Burnable Absorber Type	Fuel Pellet Type	Enrichment Range (w/o)	End of Cycle Burnup (MWD/MTU)
NC1	B_4C/Ag-In-Cd	B_4C	Solid	1.93-2.94	12,451
NC15	B_4C/Ag-In-Cd	B_4C/Gadolina	Solid	2.30-4.48	17,384
NC16	B_4C/Ag-In-Cd	Gadolina/Erbia	Solid	2.30-4.48	19,686
NC17	B_4C/Ag-In-Cd	Gadolina/Erbia	Solid	2.30-4.54	19,802
NC18	B_4C/Ag-In-Cd	Erbia/IFBA	Solid/Annular	3.81-4.54	20,954
NC19	B_4C/Ag-In-Cd	IFBA	Solid/Annular	3.75-4.63	19,788
NC20	B_4C/Ag-In-Cd	IFBA	Solid/Annular	3.57-4.63	19,981
NC21	B_4C/Ag-In-Cd	IFBA	Solid/Annular	3.57-4.16	19,747
NC22	B_4C/Ag-In-Cd	IFBA	Solid/Annular	3.58-4.38	21,214
NC23	B_4C/Ag-In-Cd	IFBA	Solid/Annular	3.55-4.38	19,936
NC24	B_4C/Ag-In-Cd	IFBA	Solid/Annular	3.55-4.43	18,602
NC25	B_4C/Ag-In-Cd	IFBA	Solid/Annular	3.00-4.43	17,579

Table 5-16: Summary of Validation Criteria and Results

Low Power Startup Physics Comparisons

Table 5-17: HZP ARO Critical Boron Concentration Statistics

a,b,c

Table 5-18: HZP ARO ITC Statistics

a,b,c

Table 5-19: HZP Total Rod Worth Statistics

a,b,c

Table 5-20: CE Specific Doppler Power Coefficient Comparison Statistics

a,b,c

HFP Depletion Comparison

Table 5-21: HFP Critical Boron Concentration Statistics

a,b,c

Table 5-22: HFP ARO Radial Power Distribution Statistics
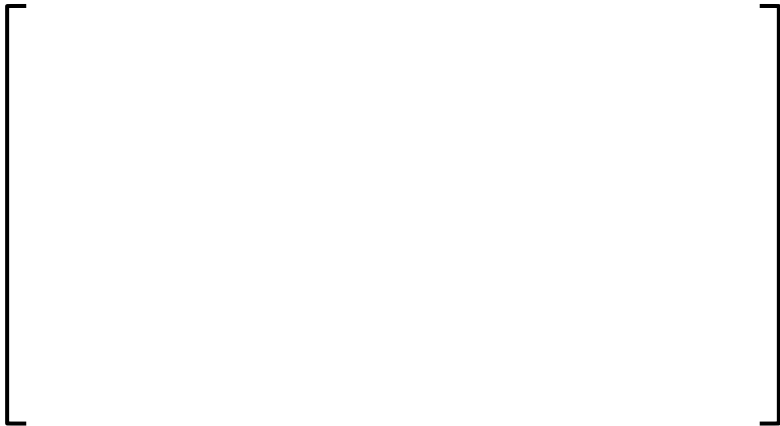
a,b,c

Table 5-23: Critical Experiment Statistics
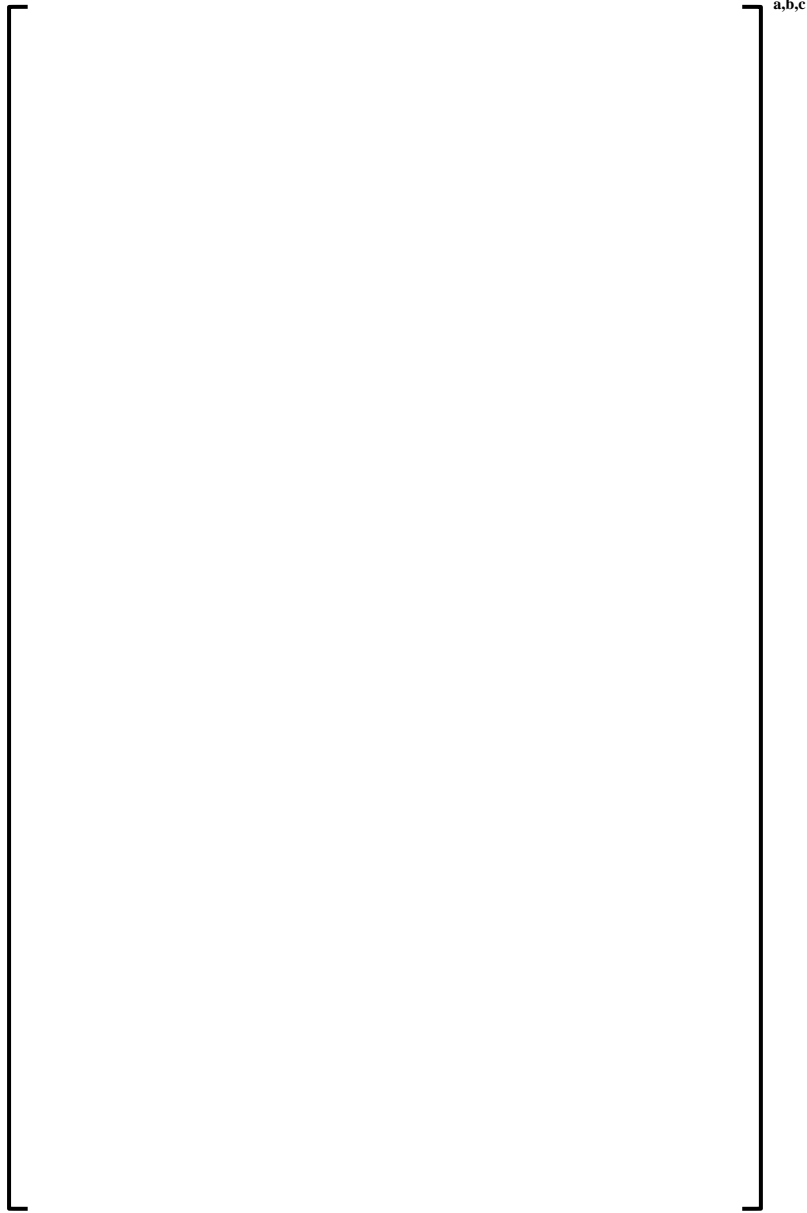
a,b,c

Table 5-24: HFP Axial Power Distribution Statistics

a,b,c

Table 5-25: Near EOC HFP ARO MTC Measurement to PARAGON2/ANC Statistics

a,b,c

Table 5-26: Near EOC HFP ARO MTC PARAGON2/ANC to PARAGON/ANC Statistics

a,b,c

PARAGON/ANC vs. PARAGON2/ANC Comparison

Table 5-27: Steam line Break/Shutdown Margin Statistics

a,b,c

Table 5-28: Dropped Rod Statistics

a,b,c

Table 5-29: Rod Ejection Statistics

a,b,c

Page Intentionally Left Blank

6   CONCLUSION

The objective of this report was to provide the information and data necessary to license PARAGON2; both as a standalone transport code and as a nuclear data source for a core simulator in a complete nuclear design code system for core design, safety and operational calculations. PARAGON2 is a new transport code developed by Westinghouse and is based on collision probability methods and is written entirely in FORTRAN. PARAGON2 can provide nuclear data, including both cross-sections and pin power information, to a core simulator code such as ANC.

Section 2 presented an overview of the PARAGON2 code and theory. The main enhancements implemented in PARAGON2 are the adoption of an UFEML and the implementation of the RSM. With UFEML, PARAGON2 reproduces the continuous energy solutions and therefore bypass the usage of the traditional resonance self-shielding calculation that is typically used in lattice physics codes.

The qualification presented in this report followed a systematic qualification process, which has been used previously by Westinghouse to qualify nuclear design codes. This process starts with the qualification of the basic methodology used in the code and proceeds in logical steps to qualification of the code as applied to a complete nuclear design code system.

6.1   PARAGON2 BENCHMARKING

Consistent with the qualification process described above, Section 3 presented the results of PARAGON2 run as a standalone code for a series of critical experiments; these experiments included integral experiments and critical experiments. The integral experiments comprise the Hellstrand, TRX, Strawbridge-Barry criticals, and CRIEPI experiments. The critical experiments encompass the KRITZ high temperature criticals, a large number of spatial criticals from the B&W physics verification program, the KRITZ-2 MOX experiment, the VENUS-2 MOX experiment, the NCA experiments, the RPI experiments, and [   ]**a,c**. Some of these experiments provided both reactivity and power distribution measurements.

The analyses of the PIE experiments were also presented in Section 3. Various samples from many reactors were considered, covering several PWR fuel lattices, enrichments and burnups. Actinides and fission products were considered in the comparison between measurement and PARAGON2 predictions.

In Section 4, PARAGON2 predictions were compared to Monte Carlo continuous energy solutions. The comparisons included all PWR lattice types, a variety of burnable absorbers, a range of UO_2 enrichments [   ]**a,c**, and several fuel composition types. Comparisons included all reactor operating conditions (CZP to HFP, control rod insertions, etc.), and assembly depletions.

6.1.1   Critical Experiments

6.1.1.1   Integral Experiments

The Hellstrand's experiments for measuring U-238 RI were analyzed. Irradiated fuel rods of uranium metal and uranium oxides provide measured capture rates at epithermal energy range that are compared to PARAGON2 predicted values. PARAGON2 with RSM model compared better to the experiments than the asymptotic model. PARAGON2 RI coefficient values are [

]**a,c**

The resonance integrals as a function of fuel rod size were also analyzed and PARAGON2 predictions compared well with experiment values.

The relative U-238 resonance neutron capture per atom was measured for cylindrical, 0.387-in. diameter rods of uranium metal, UO_2, and U-Zr alloy placed in a water hole in the TRX critical facility. The measured radial distribution of the U-238 resonance capture was compared to PARAGON2 predictions for the three fuel rod types. The measured capture reaction rate profile within the pellet for all fuels was accurately predicted by PARGAON2 as demonstrated in the figures provided in Section 3.

The CRIEPI PIE experiment for a UO_2 pin was analyzed and outlined in Section 3.1.1.3. The discharge average burnup of the UO_2 sample in this experiment is ~74.5 GWd/t and the burnup of the peripheral region was estimated at about 150 GWd/t. The measured radial distributions of the burnup and actinides concentrations (uranium and plutonium) were compared to the PARAGON2 predicted values. PARAGON2 predicts accurately both the measured burnup including the peak at the pellet periphery and the profile variations of the uranium and plutonium actinides within the depleted fuel pellet.

The Strawbridge-Barry 101 criticals cover a wide range of lattice parameters and therefore provide a severe test for the lattice code. Since these experiments are uniform lattices, the criticals were run as single pin cells in PARAGON2. There are 40 UO_2 experiments among the 101 criticals. The mean k_{eff} for these experiments calculated by PARAGON2 is [   ]^{a,c}. The mean k_{eff} for all experiments was [   ]^{a,c}. As for the comparison with Monte Carlo, the two codes give almost the same results, with a mean delta k_{inf} of [
           ]^{a,c}. The results of these criticals were plotted as a function of water to uranium ratio, enrichment, experimental buckling, and pellet diameter. No biases or trends were seen as a function of any of these parameters.

PARAGON2's good predictions of the experimental values of:

1) the total pellet U-238 capture resonance integral as a function of the temperature,

2) the U-238 capture profile within a fuel pellet,

3) the radial distribution of burnup and actinides concentrations within a depleted pellet, and

4) the reactivity of large number of pin cells covering wide range of lattice parameters,

show that: 1) the fine energy mesh method adopted in PARAGON2 and its cross-section library is accurate, and, 2) the resonance scattering model is important to accurately predict the fuel temperature Doppler effect that results from U-238 capture.

6.1.1.2   Critical Experiments

6.1.1.2.1 B&W Spatial Critical Experiments

The B&W spatial criticals provided data on both reactivity and power distribution for a variety of uranium-oxide fueled lattices. A total of twenty-nine configurations were analyzed: nine with pyrex rods, six with gadolinia rods, five with gadolinia rods and control rods with 2.46 wt% U-235 enrichment, six with gadolinia and control rods with 4.02 wt% U-235, and three with gadolinia and 2x2 water rods simulating a CE type core. k_{inf} comparisons were made between PARAGON2 and the Monte Carlo code MCNP for all

twenty-nine experiments. In addition, the measured axial bucklings were used with the PARAGON2 results to calculate k_{eff}. The reactivity results for all configurations were very good with the overall k_{eff} for the twenty-nine experiments being **[   ]a,c**.

Rod power distribution comparisons of PARAGON2 results against measurements were provided for six of the experiments – two with no burnable absorbers, two with gadolinia burnable absorbers, and two with Pyrex burnable absorbers. The average difference between the measured and PARAGON2 power distribution for the six experiments was **[   ]a,c**.

6.1.1.2.2 KRITZ High Temperature Critical Experiments

The KRITZ high temperature criticals provide critical benchmark data for uranium-fueled, water moderated lattices at high temperatures. The criticals were run at temperatures as high as 519 K. Twelve KRITZ experiments were modeled in PARAGON2. The mean k_{eff} for the twelve experiments was **[   ]a,c**. No significant trends across the large temperature range of these criticals were observed. The small standard deviation shows that PARAGON2 predicts very consistently across the large temperature range.

6.1.1.2.3 MOX Critical Experiment

6.1.1.2.3.1 KRITZ-2 Experiment

KRITZ-2:19 experiment was designed to attain criticality of a rectangular array of mixed oxide Zircaloy-2-clad fuel rods in light water by regulating the concentration of boron in the water and by adjusting the water level. Criticality was achieved at isothermal conditions at room temperature (294 K) (cold experiment) and at elevated temperature (509 K) (hot experiment). The fuel used was composed of 0.16 wt% U-235 uranium enriched and 1.5 wt% PuO_2 of total plutonium.

The cold and hot experiments were modeled in PARAGON2 and MCNP using the full radial 2D experimental configurations. The absolute differences in k_{inf} between the two codes are **[   ]a,c** for respectively cold and hot experiments. The measured fission reaction rates were compared to PARAGON2 predictions for both hot and cold cases. The standard deviations of these differences are **[   ]a,c** for cold and hot experiments, respectively.

6.1.1.2.3.2 VENUS-2 Experiment

The central part of the VENUS-2 MOX core consists of UO_2 fuel pins with MOX fuel pins loaded on the periphery of the core. The VENUS-2 core consists of twelve "15x15" subassemblies. Each of the four central assemblies contain 3.3 wt% U-235 enriched UO_2 fuel pins and 10 Pyrex pins. The 8 periphery assemblies contain both UO_2 and MOX fuel, with the 7 internal rows containing 4.0 wt% U-235 enriched UO_2 and the 8 external pins containing MOX fuel (UO_2-PuO_2) enriched with 2.0 wt% in U-235 and 2.7 wt% in high-grade plutonium with the major plutonium isotopes. The VENUS-2 experiment was designed to study the MOX and UO_2 assembly interactions.

VENUS-2 two-dimensional full core was modeled directly in PARAGON2. The axial buckling provided in the references was used with the PARAGON2 reactivity result to calculate k_{eff}.

The PARAGON2 k_{eff} obtained is **[   ]a,c**, which is in a good agreement with the experiment. The measured pin-wise fission reaction rates were compared to PARAGON2 values. The standard deviation for

individual fuel assembly types is small and within a maximum of [
                          ]**a,c**. The standard deviation for the whole core is slightly larger and the maximum absolute error is within [   ]**a,c**. The standard deviations of all the differences are within 1σ or 2σ of the measurement uncertainties.

6.1.1.3   NCA Critical Experiments

Toshiba NCA is a tank type light water moderated nuclear facility that is operated at room temperature and at atmospheric pressure. The level of the water is adjusted to achieve the criticality. The central region of the core is configured according to the experiments needs, while the driver region is normally built with fuel rods with 2 wt% U-235 enrichment.

Five configurations (Core-1 to Core-5) were designed to mimic current commercial cores in operation. For all the experiments, the cores are arranged in a square geometry with same rods pitches and sizes. The uranium enrichment used in these experiments ranges between 2 wt% and 4.9 wt%. Tungsten rods and gadolinium burnable absorber rods were also used. Core-4 and Core-5 simulates the hot full power PWR operating conditions by using 1000 ppm of boron and polystyrene blocks.

All five experiments were modeled using PARAGON2 and MCNP codes. The 3D results of MCNP were used to confirm the accuracy of the cross-section data used. PARAGON2 predictions were compared to the equivalent 2D MCNP. The results show good reactivity agreement between continuous energy Monte Carlo and PARAGON2. All the tungsten rodded cases (Core-1, Core-2 and Core-3) seem to be well predicted (absolute difference [   ]**a,c**). Core-4 and Core-5 show slightly larger differences because of polystyrene blocks inserted.

Measured fission rates distributions were compared to PARAGON2 predictions. For all the cores, all the differences are below two-standard deviations of the experimental errors (2σ). [
                                                                            ]**a,c** The Root Mean Square (RMS) of the differences ranges from [   ]**a,c** indicating an overall good fission rates prediction of PARAGON2 calculations.

6.1.1.4   Critical Experiments with Erbia-Urania Fuel

A series of critical experiments were conducted by CE at the RPI RCF to measure and compare predicted values of different parameters including local power distributions for lattice configurations similar to a standard 16x16 CE fuel design but with Erbia-Urania fuel. The number of Erbia pins in the central 16x16 array was varied to accommodate a range of erbium loadings. The CE fuel consisted of UO_2 fuel rods enriched to 3.65 wt% and UO_2-Er_2O_3 fuel rods of 1.5 wt% Erbia.

The main purpose of this benchmark is to compare the PARAGON2 predicted pin power distribution against the measurements for CE fuel types with Erbia. The root mean square for all these cores varies between [   ]**a,c** and is within the measurements uncertainty. The absolute maximum differences vary between [   ]**a,c**. The differences obtained for measured pin power distribution and for reactivity comparison against Monte Carlo are similar in magnitude to other experiments analyzed.

[   ]**a,c**

a,c
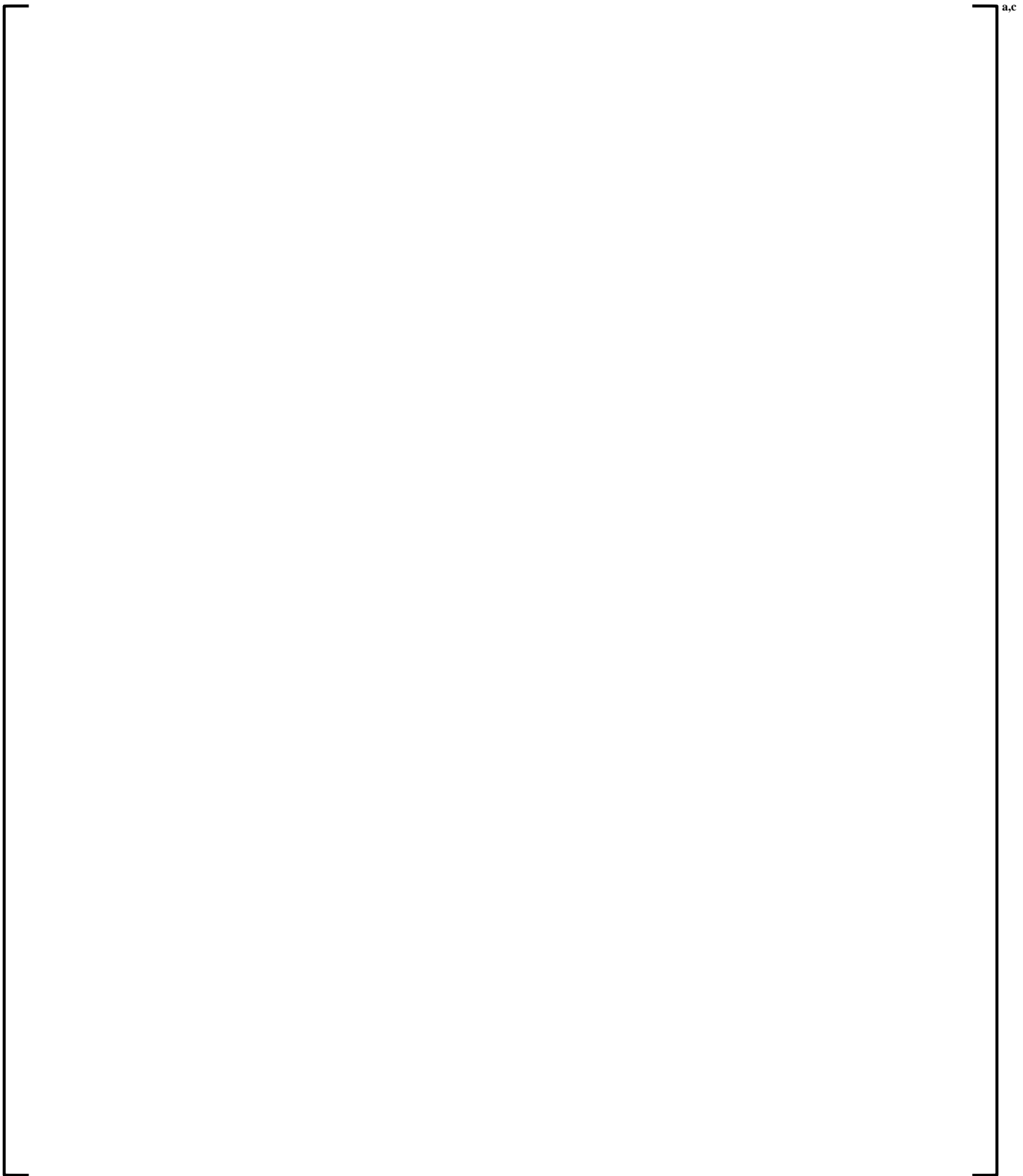
6.1.2   Isotopics Data

Several PIE benchmarks from SFCOMPO 2.0 database were analyzed. Benchmarks were selected based on several criteria; such as coverage of a wide range of burnup, coverage of multiple lattice and reactor

designs, and coverage of a wide range of enrichment. PIE benchmarks chosen for this work contain isotopic concentration data for samples from small segments of fuel rods in assemblies from past operation at the Gösgen-1, TMI-1, Calvert Cliffs-1, Turkey Point-3, and Vandellos-2 plants.

For each case, single assembly PARAGON2 modeling was performed mimicking the operating conditions as much as possible. The final pin burnups in PARAGON2 were iterated on until the values were considered to be sufficiently close to the sample burnups. PARAGON2 predictions were compared to measurements for all the samples. Overall, for actinides the average relative differences is [

]^{a,c}. For fission products, the corresponding values are [

]^{a,c}. These results are acceptable and fall within the usual discrepancies in the analyses of the PIE experiments.

The spectrograph-measured isotopics data for Saxton Cores 2 and 3 with mixed oxide fuel, Yankee cores 1, 2, and 4 with stainless steel clad fuel, and Yankee Core 5 with zircaloy clad fuel have been compared to isotopic concentrations from PARAGON2 calculations simulating the power history corresponding to these cores. These isotopic comparisons show no significant trend for any isotope with burnup. These excellent results demonstrate the capability of PARAGON2 for predicting the depletion characteristics of both UO_2 and PuO_2 LWR fuel over a wide range of burnup conditions.

6.1.3   Numerical Benchmarks

Ten different assembly configurations were calculated in both PARAGON2 and the Monte Carlo code SERPENT2. These assembly configurations were chosen to cover a variety of lattice types, fuel composition types (including MOX), and burnable absorbers over a given enrichment range [

]^{a,c}. Seven Westinghouse and three CE assemblies were included in these calculations. The PARAGON2 and SERPENT2 calculations were compared for both reactivity and power distribution.

For CZP, HZP and HFP conditions [   ]^{a,c}, the mean difference in reactivity between the PARAGON2 and SERPENT2 calculations over the ten assemblies was very good and in the interval between [   ]^{a,c}. All the absolute differences are less than [   ]^{a,c}. The differences of k_{inf} values of both codes as a function of burnup were also compared. The maximum average difference between SERPENT2 and PARAGON2 is [

]^{a,c}. Combining all the assembly cases, overall, the results are very good with an average difference of [   ]^{a,c}.

The comparison between the SERPENT2 and PARAGON2 power distributions showed very good agreement. The maximum standard deviation is [   ]^{a,c} and, for the individual pins, the maximum absolute error obtained for all calculations of all burnups is [   ]^{a,c}. For the overall statistics, the standard deviation of the relative differences is [   ]^{a,c}.

[   ]^{a,c}

The agreement between PARAGON2 and Monte Carlo is very good and very consistent **[**

][a,c]. Therefore, this analysis confirms that PARAGON2 can reproduce the Monte Carlo continuous energy neutron multiplication factors with the desired accuracy **[   ]**[a,c] in average, and the Monte Carlo continuous energy pin power with the desired standard deviation accuracy of **[   ]**[a,c].

6.2   PLANTS COMPARISONS

The primary use of PARAGON2 will be to generate nuclear data for use in Westinghouse core simulator codes. Thus, the most important qualification for PARAGON2 is comparisons of results of core calculations using PARAGON2 supplied nuclear data against measured plant data. This report presented ANC results for PWR core calculations with nuclear data supplied by PARAGON2, which were compared to corresponding plant measurements where available and to PARAGON/ANC results for some important safety related calculations. These calculations demonstrated the accuracy of the PARAGON2 nuclear data when applied to a complete nuclear design system. The calculations also demonstrated that PARAGON2 could replace all the previously licensed Westinghouse PWR lattice codes, such as PARAGON and PHOENIX-P, for use in all the previously licensed Westinghouse methodologies for PWR applications.

6.2.1   Startup Test Results Comparisons

Comparisons were made in Section 5.3 for PARAGON2/ANC predictions against measurements for the key startup physics parameters: ARO HZP BOC ITC, ARO HZP critical boron concentrations, total rod worths, and individual control rod bank worths. PARAGON2/ANC demonstrates a good agreement to measurement and provides an accurate representation of the reactor core during HZP startup physics testing. The conclusion is based on the results listed in Table 5-16.

Doppler Power Coefficients predictions were compared to plant measurements for the CE reactor cores to demonstrate the accuracy of the RSM in PARAGON2. The Doppler power coefficients are a CE specific parameter evaluated during startup physics testing of some cycles. Based on the results provided in Table 5-20, The DPC values show good agreement when compared to measurement.

6.2.2   HFP Depletion Results Comparison

Comparisons were made in Section 5.4 for PARAGON2/ANC predictions against measurements for the key HFP depletion parameters: HFP ARO critical boron concentrations and HFP radial power distributions at key times in core life. The HFP ARO critical boron concentrations were reviewed to demonstrate the acceptance level for all present and future applications of PARAGON2. Table 5-21 shows good agreement with the average and standard deviation of the measured-minus-predicted differences for all the plants listed in Table 5-1. Moreover, PARAGON2/ANC demonstrates a good agreement to measurement and provides an accurate representation of the reactor core during HFP conditions as it pertained to reconstructing assembly-wise power distributions. The peaking factor ($F_{\Delta H}$, F_Q) statistical uncertainties to be applied to all Westinghouse calculations bounds the uncertainties determined for PARAGON2/ANC. The conclusions are based on the results listed in Table 5-16.

6.2.3   Other Comparisons

Comparisons were made in Section 5.5 for PARAGON2/ANC predictions against PARAGON/ANC results as it relates to key safety parameters: ARI-WSR rod worth and peaking factors for shutdown margin,

dropped rod worth and relevant peaking factors for the dropped rod accident, ejected rod worth and relevant peaking factors for the rod ejection accident, and EOL MTC. PARAGON2/ANC demonstrates good agreement with PARAGON/ANC results for each of the aforementioned parameters and summarized in Table 5-25 through Table 5-29. Particularly for plants with the exemption of the most negative EOL MTC measurement obtained with either PHOENIX-P/ANC or PARAGON/ANC, the exemption can be maintained when using PARAGON2/ANC and does not require any new NRC licensing requests.

6.3   CONCLUSION

The data presented in this report provide the basis for the qualification of PARAGON2 both as a standalone transport code and as the nuclear data source for core simulator codes. In Sections 3 and 4, standalone PARAGON2 was qualified against a wide variety of criticals and Monte Carlo calculations. In Section 5, PARAGON2 was qualified as a supplier of core simulator code nuclear data through comparisons of the PARAGON2 results with ANC as the core simulator against measured data and against PARAGON/ANC for a wide variety of plant designs and problems. The report demonstrates that PARAGON2 can replace all the previously licensed Westinghouse PWR lattice codes, such as PHOENIX-P and PARAGON, for use in all the previously licensed Westinghouse methodologies for PWR applications. The uncertainties used in the current safety analysis will remain bounding.

7 SUMMARY AND LICENSING CRITERIA

The data and conclusions shown in the previous sections provide a qualification basis for PARAGON2 as a standalone code and as a supplier of assembly lattice nuclear data to a core simulator. PARAGON2 predictions were compared to Monte-Carlo continuous energy solutions, to clean critical experiments, and to plant measurement data. These comparisons demonstrated consistent representation across all fuel types (i.e. no trends as a function of geometry, material compositions, or lattice type). The main reason behind this high degree of accuracy was that the ultimate goal and philosophy used in developing PARAGON2 was to attempt to obtain close agreement between PARAGON2 and Monte-Carlo continuous energy solutions.

PARAGON2 can produce results that are in close agreement with Monte-Carlo continuous energy by using a UFEML. The cross-sections derived from UFEML depend only on the temperature and energy mesh used for multi-group solution. This is in contrast with the approach used in other legacy lattice physics simulation codes that generate state dependent cross-sections inside the code using a resonance self-shielding method before the flux solution. [

]^{a,c}

7.1 IMPLEMENTATION OF PARAGON2

Based on the qualification of PARAGON2 as documented herein, PARAGON2 can be used as a standalone or as a direct replacement for all the previously licensed Westinghouse PWR lattice codes, such as PHOENIX-P and PARAGON. Thus, other topical reports that reference the Westinghouse nuclear design code system will remain applicable with PARAGON2.

7.2 FUTURE UPDATES TO PARAGON2

It is a well-established understanding in reactor physics that the Monte Carlo continuous energy solution is the highest order neutron transport method that can be achieved. Monte Carlo has less approximations than any other deterministic transport method. Therefore, any deterministic code with equivalent physics models that can produce results that are in close agreement with Monte Carlo is likely to achieve the highest possible accuracy. [

]^{a,c}

With the continuous improvements in computing time as well as in the quality of the basic nuclear data, Westinghouse intends to periodically improve its cross-section library and its lattice physics code series PARAGON2. [

]^{a,c}

7.2.1 Licensing Approval Applicability Criteria – 3LAAC Process

a,c

a,c

7.3   SUMMARY

The data provided in this report demonstrates that PARAGON2 is equivalent to continuous energy Monte Carlo solutions, and that the PARAGON2/ANC code system accurately predicts plant measurement data.

a,c

a,b,c

Page Left Intentionally Blank

8   REFERENCES

1. Calic, D., Štancar, Z., & Snoj, L. (2018). Analysis of VENUS-2 Benchmark Using SERPENT2 Code. Annals of Nuclear Energy(116), 334-346.

2. Chadwick, M. B. (2011). ENDF/B-VII.1 Nuclear Data for Science and Technology: Cross-sections, Covariances, Fission Product Yields and Decay Data. Nuclear Data Sheets, 112, p. 2887. Retrieved from http://doi.10.1016/j.nds.2011.11.002

3. C-NCA-508. (2009). A General Description of the Specifications of the TOSHIBA Nuclear Critical Assembly (CA). Toshiba Corporation.

4. Crain, H. H. (1973). Saxton Plutonium Project - Quarterly Progress Report for the Period Ending September 30, 1973. WCAP-3385-37.

5. Fetterman, R. J. (1993). Safety Evaluation Supporting the Conditional Exemption of the Most Negative EOL Moderator Temperature Coefficient Measurement. WCAP-13749.

6. Gauld, I. C. et al. (2011). Analysis of Experimental Data for High Burnup PWR Spent Fuel Isotopic Validation - Vandellos II Reactor. Oak Ridge National Laboratory.

7. Gauld, I. C. et al. (2016). Re-Evaluation of Spent Nuclear Fuel Assay Data for the Three Mile Island Unit 1 Reactor and Application to Code Validation. Annals of Nuclear Energy, 87.

8. Gauld, I. C. et al. (2017). Integral Nuclear Data Validation Using Experimental Spent Nuclear Fuel Compositions. Nuclear Engineering and Technology, 49.

9. Goodspeed, R. C. (1973). *Saxton Plutonium Project - Quarterly Progress Report for the Period Ending June 20, 1973.* WCAP-3385-36.

10. Harris, D. R. et al. (1992). Critical Experiments for ABB-CE Fuel with Erbium Burnable Absorber. *Trans. American Nuclear Society, 65(414).*

11. Hellstrand, E. (1957). Measurements of the Effective Resonance Integral in Uranium Metal and Oxide in Different Geometries. *Journal of Applied Physics, 28*, 1493-1502.

12. Hellstrand, E., & Lundgren, G. (1962). The Resonance Integral For Uranium Metal and Oxide. *Letters to the Editors - Nuclear Science & Engineering, 12*, 435-436.

13. Hellstrand, E., Blomberg, P., & Horner, S. (1960). The Temperature Coefficient of the Resonance Integral for Uranium Metal and Oxide. *Nuclear Science and Engineering, 8*, 497-506.

14. Huria, H. C., & Ouisloumen, M. (1997). ENDF/B-VI: U-238 Resonance Integral Reduction - A Closer Look. *Trans. American Nuclear Society, 76*, p. 329.

15. International Handbook of Evaluated Criticality Safety Benchmark Experiments (ICSBEP). (2016). *NEA/NSC/DOC (95)03*. Nuclear Energy Agency.

16. Kelly, D. J. et al. (2014). Analysis of Select BEAVRS PWR Benchmark Cycle 1 Results Using MC21 and Open MC. *Proc. Int. Conf. on the Physics of Reactors PHYSOR 2014.* Kyoto, Japan.

17. Langford, F. L., Nath, R. J., Spier, E. M., Nguyen, T. Q., Frank, F. L., Secker, J. R., . . . Chelmer, H. (1988). *Evaluation of Nuclear Hot Channel Factor Uncertainties.* WCAP-7308-L-P-A.

18. Lee, D., Rhodes, J., & Smith, K. (2009). The Impact of 238U Resonance Elastic Scattering Approximations on Therma Reactor Doppler Reactivity. *Ann. of Nuclear Energy, 36*, p. 274.

19. Leppänen, J., Pusa, M., Viitanen, T., Valtavirta, V., & Kaltiaisenaho, T. (2015). The Serpent Monte Carlo Code: Status, Development and Applications in 2013. *Annals of Nuclear Energy* (82), 142-150.

20. Liu, Y., Meliksetian, A., Little, D., Nakano, F., & Poploski, M. (1985). *ANC: A Westinghouse Advanced Nodal Computer Code.* WCAP-10965-P-A.

21. Liu, Y., Wang, X., & Martin, W. R. (2018). Resonance Integral Validation for MPACT with Hellstrand's Experiments. *Transactions of the American Nuclear Society*, *119.* Orlando, Florida.

22. MacFarlane, R. E., & Kahler, A. C. (2010). Methods for Processing ENDF/B-VII with NJOY. *Nuclear Data Sheets, 111*, p. 2739. Retrieved from http://dx.doi.org/10.1016/j.nds.2010.11.001

23. Matsumoto, H., Ouisloumen, M., & Takeda, T. (2005). Development of Spatially Dependent Resonance Shielding Method. *Journal of Nuclear Science and Technology, 42* (8), 688-694.

24. Melehan, J. B. (1971). *Yankee Core Evaluation Program Final Report.* WCAP-3017-6094.

25. Messaoudi, N., & Na, B. C. (2004). *Benchmark on the Three-Dimensional VENUS-2 MOX Core Measurements, Final Report.* NEA/NSC/DOC(2003)5, ISBN 92-64-02160-4.

26. (1993). *Methodology for Core Designs Containing Erbium Burnable Absorbers.* ABB Combustion Engineering Nuclear Fuel, CENPD-382-P-A.

27. Michel-Sendis, F. et al. (2017). SFCOMPO-2.0: An OECD NEA Database of Spent Nuclear Fuel Isotopic Assays, Reactor Design Specifications and Operating Data. *Annals of Nuclear Energy, 110*.

28. Mosteller, R. D. (1995). Critical Lattices of UO2 Fuel Rods and Pertubing Rods in Borated Water. *LA-UR 95-1434*.

29. Mosteller, R. D. (2007). The Doppler-Defect Benchmark: Overview and Summary of Results. *Joint International Topical Meeting on Mathematics & Computation and Supercomputing in Nuclear Applications (M&C + ANC 2007).* Monterey, California.

30. Newman, L. W. (1984). *Urania-Gadolinia: Nuclear Model Development and Critical Experiment Benchmark.* DOE/ET/34212-41.

31. Nguyen, T. Q. et al. (1988). *Qualification of the PHOENIX/ANC Nuclear Design System for Pressurized Water Reactor Cores.* WCAP-11596-P-A (Proprietary), WCAP-11597-A (Non-Proprietary).

32. Nodvik, R. J. (1969). *Supplementary Report on Evaluation of Mass Spectrometric and Radiochemical Analyses of Yankee Core I Spent Fuel, Including Isotopics of Elements Thorium through Curium.* WCAP-6086.

33. Nodvik, R. J. (1970). *Saxton Core II Fuel Performance Evaluation Part II: Evaluation of Mass Spectrometric and Radiochemical Analyses of Irradiated Saxton Plutonium Fuel.* WCAP-3385-56.

34. Okumura, K. et al. (2000). Validation of a Continuous-Energy Monte Carlo Burn-up Code MVP-BURN and Its Application to Analysis of Post Irradiation Experiment. *Journal of Nuclear Science and Technology, 37*, 2.

35. Ouisloumen, M. (2015). Coupled Neutron-Photon Two-Dimensional Whole Core Depletion Calculation Using PARAGON With Ultra-Fine Energy Mesh Methodology. *Joint International Conference on Mathematics and Computation (M&C), Supercomputing in Nuclear Applications (SNA) and the Monte Carlo (MC) Method.* Nashville, Tennessee.

36. Ouisloumen, M. (2017). PARAGON2 Depletion Validation Using SERPENT2 Monte Carlo Code. *M&C 2017 - International Conference on Mathematics & Computational Methods Applied to Nuclear Science & Engineering.* Jeju, South Korea.

37. Ouisloumen, M. (2017). Validation of PARAGON2 Ultra-Fine-Energy-Mesh Method Against Deterministic Continuous Energy Calculation. *M&C 2017 - International Conference on Mathematics & Computational Methods Applied to Nuclear Science & Engineering.* Jeju, South Korea.

[   ][a,c]

39. Ouisloumen, M. et al. (2001). PARAGON: The New Westinghouse Lattice Code. *Proc. ANS Int. Meeting on Mathematical Methods for Nuclear Applications.* Salt Lake City, Utah, USA.

40. Ouisloumen, M. et al. (1996). The Two-Dimensional Collision Probability Calculation in Westinghouse Lattice Code: Methodology and Benchmarking. *Proc. Int. Conf. On The Physics Of Reactors PHYSOR96*, *1, A366.* Mito, Japan.

41. Ouisloumen, M. et al. (2004). *Qualification of the Two-Dimensional Transport Code PARAGON.* WCAP-16045-P-A (Proprietary), WCAP-16045-A (Non-Proprietary).

42. Ouisloumen, M. et al. (2014). Analysis of Tungsten Gray Rods Critical Experiments Using PARAGON With Ultra-Fine Energy Mesh Methodology. *PHYSOR 2014 - The Role of Reactor Physics Toward a Sustainable Future.* Kyoto, Japan.

43. Ouisloumen, M., & Sanchez, R. (1991). A Model for Neutron Scattering Off Heavy Isotopes That Accounts for Thermal Agitation Effects. *Nuclear Science and Engineering, 107*, p. 189.

44. Ouisloumen, M., Lam, H. Q., & Huria, H. C. (2016). Predictions of PWR Cores Using PARAGON2 Based on Ultra-Fine Energy Mesh Cross-sections Library. *PHYSOR 2016 - Unifying Theory and Experiments in the 21st Century.* Sun Valley, Idaho, USA.

45. Ouisloumen, M., Ougouag, A. M., & Ghrayeb, S. Z. (2015). Anisotropic Elastic Resonance Scattering Model for the Neutron Transport Equation. *Nuclear Science & Engineering, 179*, pp. 59-84. Retrieved from http://dx.doi.org/10.13182/NSE13-99

46. Owen, D. (March 1963). *Factors for One-Side Tolerance Limits and for Variables Sampling Plans.* SCR-607.

47. Persson, R., Blomsjo, E., & Edenius, M. (1972). High Temperature Critical Experiments with H2O Moderated Fuel Assemblies in KRITZ. *NUCLEX 72.*

48. Santamarina, A. (2009). *The JEFF-3.1.1 Nuclear Data Library.* JEFF Report 22, NEA No. 6807.

49. Sasahara, A. (1996). *Post Irradiation Examination and the Validity of Computational Analysis for High Burnup UO2 and MOX Spent Fuels.* CRIEPI, Rep. T95012, Komae Research Laboratory.

50. Smalley, W. R. (1971). *Saxton II - Fuel Performance Evaluation Part I: Materials.* WCAP-3385-56 Part I.

51. Smith, G. G., Hardy, J., Klein, D., & Mitchell, J. A. (1961). Experimental Studies of U Resonance Neutron Capture in UO2 Fuel Rods. *Nuclear Science and Engineering, 9*, 421-429.

52. Snoj, L. et al. (2009). *KRITZ-2:19 Experiment on Regular H2O/Fuel Pin Lattices with Mixed Oxide Fuel at Temperature 21.1°C and 235.9°C.* International Handbook of Evaluated Reactor Physics Benchmark Experiments, NEA/NSC/DOC(2006)1, Organization for Economic Co-operation and Development/Nuclear Energy Agency.

53. Snoj, L., Kodeli, I., & Remec, I. (2014). Evaluation of the KRITZ-2 Criticality and Reaction Rate Benchmark Experiments. *Nuclear Science and Engineering*(178), 496-508.

54. Strawbridge, L. E., & Barry, R. F. (1965). Criticality Calculations for Uniform Water-Moderated Lattices. *Nuclear Science and Engineering, 23*, 58-73.

55. Thomsen, K. L. (1995). *Nuclear Science Engineering, 119*, p. 167.

56. Trkov, A., Herman, M., & Brown, D. A. (2011). *ENDF-6 Formats, Manual Data Formats and Procedures for the Evaluated Nuclear Data Files ENDF/B-VI and ENDF/B-VII.* BNL-90365-2009 Rev. 2. National Nuclear Data Center, Brookhaven National Laboratory.

57. Umano, T. et al. (2009). Critical Experiments Simulating the Operating Conditions of PWRs in the Toshiba NCA Facility. *ICAPP-2009.* Tokyo, Japan.

58. X-5 Monte Carlo Team. (2003). *MCNP - A General Monte Carlo N-Particle Transport Code, Version 5, LA-UR-03-1987.*

APPENDIX A   SUMMARY OF PLANT A

The following section contains the numerical benchmarking results for Plant A. HZP startup physics statistics, HFP depletion statistics, and radial power distributions (where applicable) are contained herein and listed below:

1. <u>HZP Startup Physics</u>

    a. ARO ITC – Table A-1

    b. ARO Critical Boron Concentration – Table A-2

    c. Total Rod Worths – Table A-3

    d. Individual Control Rod Bank Worths – Table A-4 through Table A-8

2. <u>HFP Depletion</u>

    a. ARO Critical Boron Concentration Statistics – Table A-9

Table A-1: HZP ITC – Plant A

a,b,c

Table A-2: HZP ARO Critical Boron Concentration – Plant A

a,b,c

Table A-3: HZP Total Rod Worths – Plant A

a,b,c

Table A-4: HZP Individual Control Rod Bank Worths – Plant A Cycle 2

a,b,c

Table A-5: HZP Individual Control Rod Bank Worths – Plant A Cycle 15

a,b,c

Table A-6: HZP Individual Control Rod Bank Worths – Plant A Cycle 17

a,b,c

Table A-7: HZP Individual Control Rod Bank Worths – Plant A Cycle 18

a,b,c

Table A-8: HZP Individual Control Rod Bank Worths – Plant A Cycle 19

a,b,c

Table A-9: HFP Critical Boron Concentration vs. Burnup – Plant A

a,b,c

Page Left Intentionally Blank

APPENDIX B   SUMMARY OF PLANT B

The following section contains the numerical benchmarking results for Plant B. HZP startup physics statistics, HFP depletion statistics, and radial power distributions (where applicable) are contained herein and listed below:
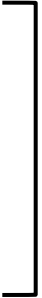
1. <u>HZP Startup Physics</u>

    a. ARO ITC – Table B-1

    b. ARO Critical Boron Concentration – Table B-2

    c. Total Rod Worths – Table B-3

    d. Individual Control Rod Bank Worths – Table B-4 through Table B-6

2. <u>HFP Depletion</u>

    a. ARO Critical Boron Concentration Statistics – Table B-7

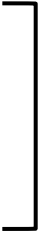**Table B-1: HZP ITC – Plant B**

a,b,c

Table B-2: HZP ARO Critical Boron Concentration – Plant B

a,b,c

Table B-3: HZP Total Rod Worths – Plant B

a,b,c

Table B-4: HZP Individual Control Rod Bank Worths – Plant B Cycle 18

a,b,c

Table B-5: HZP Individual Control Rod Bank Worths – Plant B Cycle 20

a,b,c

Table B-6: HZP Individual Control Rod Bank Worths – Plant B Cycle 21

a,b,c

Table B-7: HFP Critical Boron Concentration vs. Burnup – Plant B

[

]a,b,c

APPENDIX C   SUMMARY OF PLANT C

The following section contains the numerical benchmarking results for Plant C. HZP startup physics statistics, HFP depletion statistics, and radial power distributions (where applicable) are contained herein and listed below:

1. <u>HZP Startup Physics</u>

    a. ARO ITC – Table C-1

    b. ARO Critical Boron Concentration – Table C-2

    c. Total Rod Worths – Table C-3

    d. Individual Control Rod Bank Worths – Table C-4 through Table C-8

2. <u>HFP Depletion</u>

    a. ARO Critical Boron Concentration Statistics – Table C-9

Table C-1: HZP ITC – Plant C

a,b,c

Table C-2: HZP ARO Critical Boron Concentration – Plant C

a,b,c

Table C-3: HZP Total Rod Worths – Plant C

a,b,c

Table C-4: HZP Individual Control Rod Bank Worths – Plant C Cycle 25

a,b,c

Table C-5: HZP Individual Control Rod Bank Worths – Plant C Cycle 26

a,b,c

Table C-6: HZP Individual Control Rod Bank Worths – Plant C Cycle 27

a,b,c

Table C-7: HZP Individual Control Rod Bank Worths – Plant C Cycle 28

a,b,c

Table C-8: HZP Individual Control Rod Bank Worths – Plant C Cycle 29

a,b,c

Table C-9: HFP Critical Boron Concentration vs. Burnup – Plant C

a,b,c

Page Left Intentionally Blank

APPENDIX D   SUMMARY OF PLANT D

The following section contains the numerical benchmarking results for Plant D. HZP startup physics statistics, HFP depletion statistics, and radial power distributions (where applicable) are contained herein and listed below:

1. <u>HZP Startup Physics</u>

   a. ARO ITC – Table D-1

   b. ARO Critical Boron Concentration – Table D-2

   c. Total Rod Worths – Table D-3

2. <u>HFP Depletion</u>

   a. ARO Critical Boron Concentration Statistics – Table D-4

   b. Radial Power Distributions – Table D-5 through Table D-8

   c. Axial Power Distributions – Table D-9 through Table D-12

Table D-1: HZP ITC – Plant D

a,b,c

Table D-2: HZP ARO Critical Boron Concentration – Plant D

a,b,c

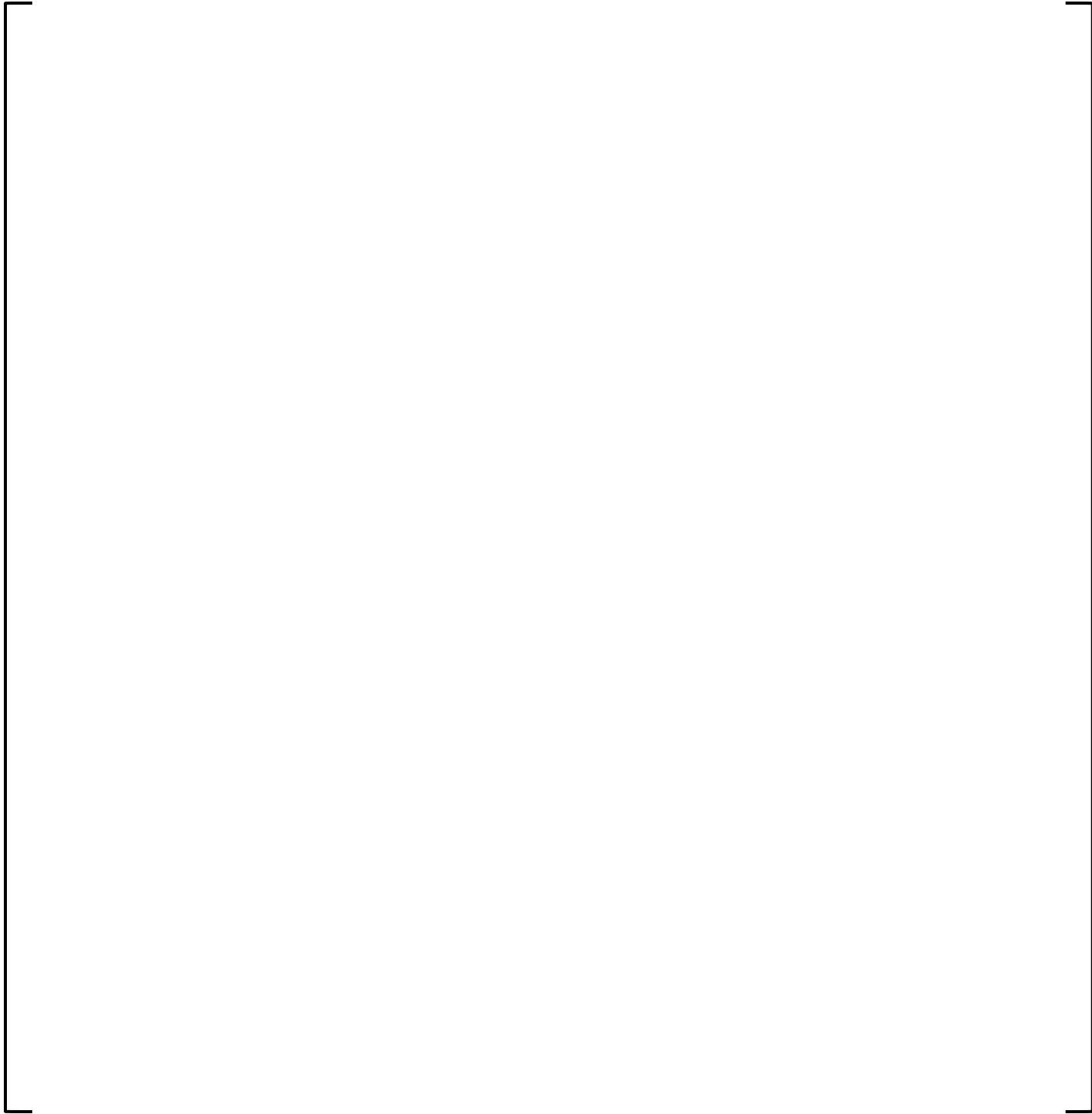**Table D-3: HZP Total Rod Worths – Plant D**

a,b,c

Table D-4: HFP Critical Boron Concentration vs. Burnup – Plant D

a,b,c

Table D-5: Assembly Average Radial Power Distribution – Plant D Cycle 28 BOC
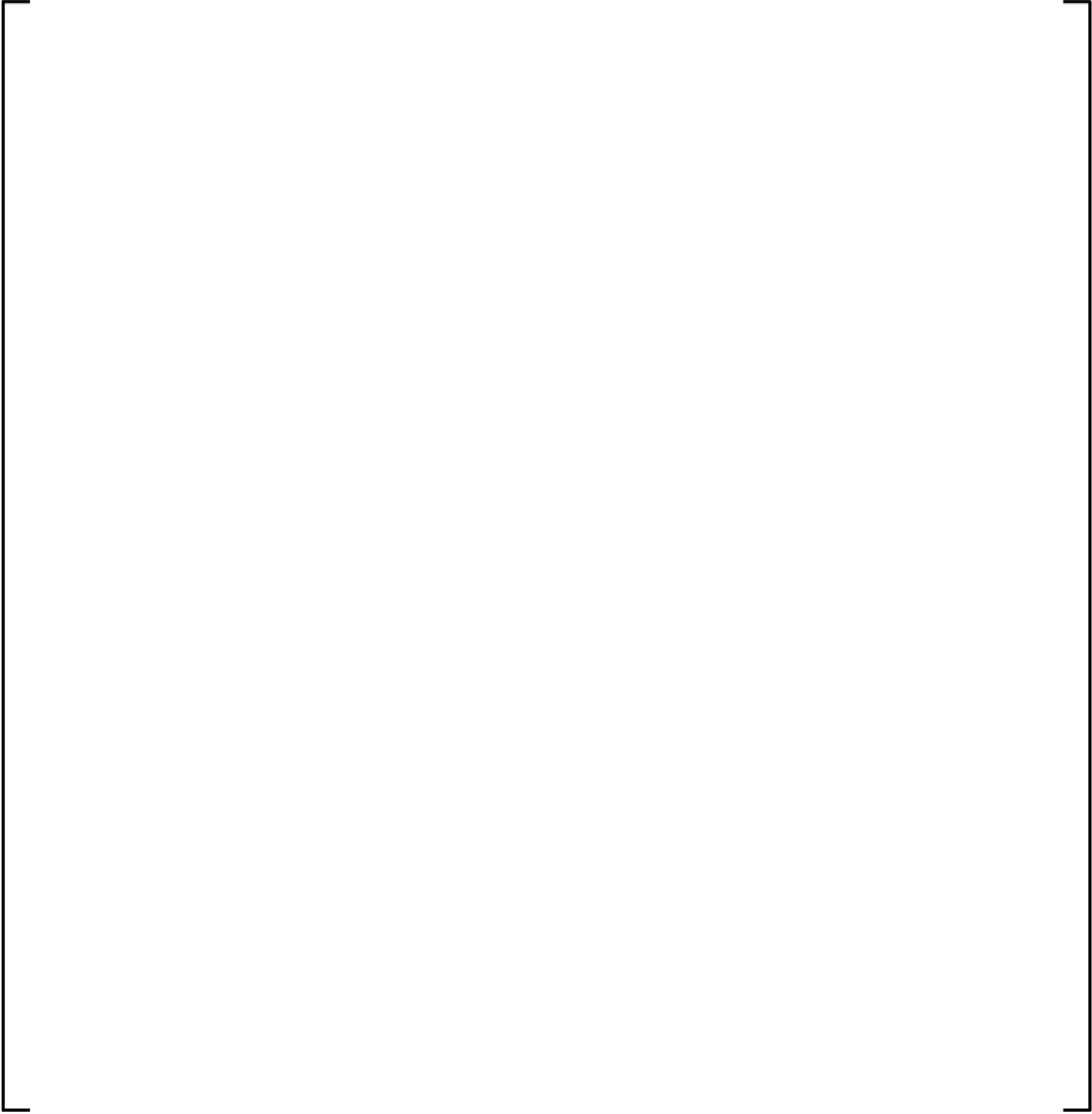
a,b,c

Table D-6: Assembly Average Radial Power Distribution – Plant D Cycle 28 MOC1
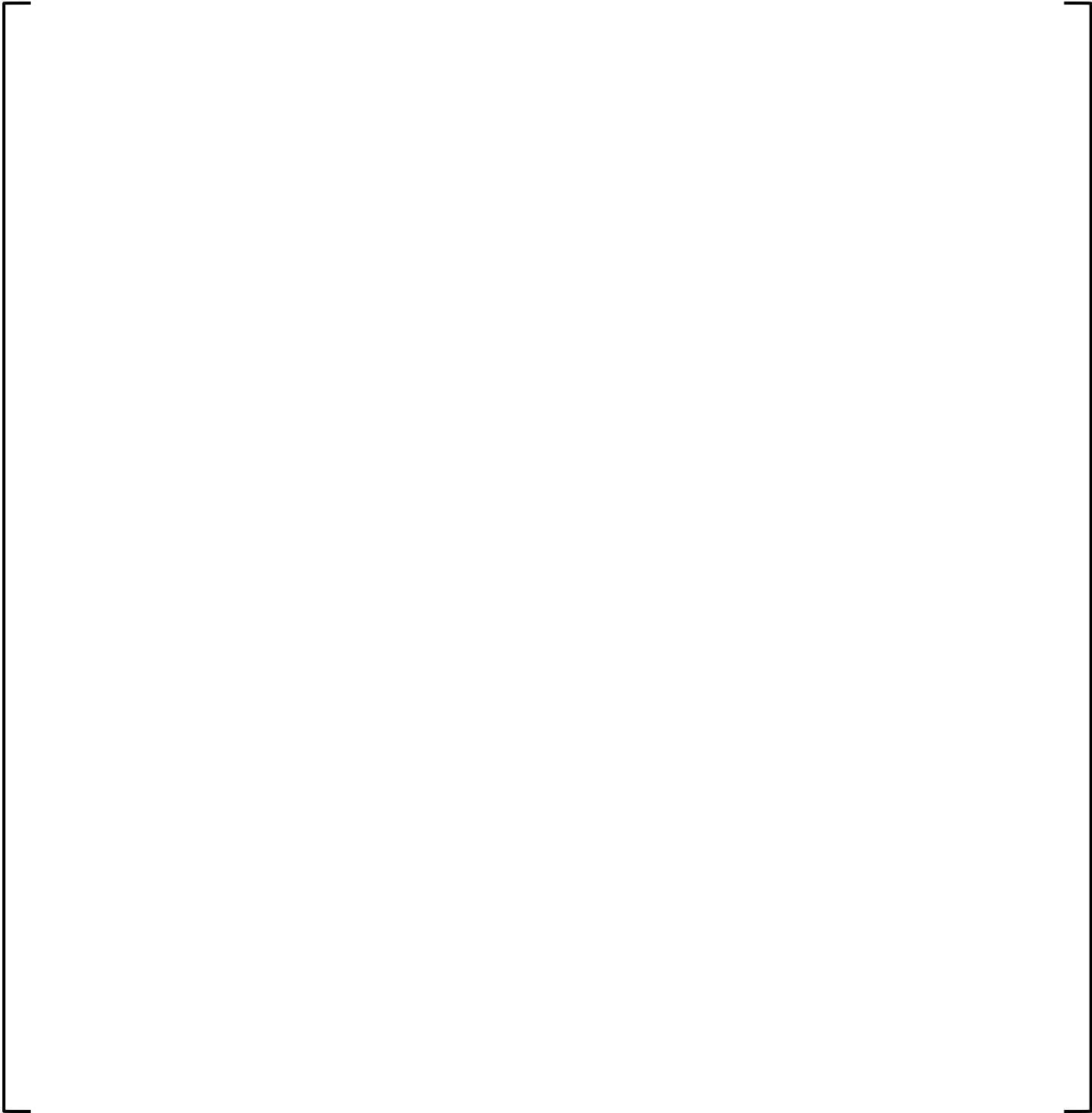
a,b,c

Table D-7: Assembly Average Radial Power Distribution – Plant D Cycle 28 MOC2

a,b,c

Table D-8: Assembly Average Radial Power Distribution – Plant D Cycle 28 EOC

a,b,c

Table D-9: Core Axial Power Distribution – Plant D Cycle 28 BOC

a,b,c

Table D-10: Core Axial Power Distribution – Plant D Cycle 28 MOC1

a,b,c

Table D-11: Core Axial Power Distribution – Plant D Cycle 28 MOC2

a,b,c

Table D-12: Core Axial Power Distribution – Plant D Cycle 28 EOC

a,b,c

Page Left Intentionally Blank

APPENDIX E   SUMMARY OF PLANT E

The following section contains the numerical benchmarking results for Plant E. HZP startup physics statistics, HFP depletion statistics, and radial power distributions (where applicable) are contained herein and listed below:

1. <u>HZP Startup Physics</u>

   a. ARO ITC – Table E-1

   b. ARO Critical Boron Concentration – Table E-2

   c. Total Rod Worths – Table E-3

   d. Individual Control Rod Bank Worths – Table E-4 through Table E-8

2. <u>HFP Depletion</u>

   a. ARO Critical Boron Concentration Statistics – Table E-9

Table E-1: HZP ITC – Plant E

[   ]a,b,c

Table E-2: HZP ARO Critical Boron Concentration – Plant E

[   ]a,b,c

Table E-3: HZP Total Rod Worths – Plant E

[   ]a,b,c

Table E-4: HZP Individual Control Rod Bank Worths – Plant E Cycle 36

a,b,c

Table E-5: HZP Individual Control Rod Bank Worths – Plant E Cycle 37

a,b,c

Table E-6: HZP Individual Control Rod Bank Worths – Plant E Cycle 38

a,b,c

Table E-7: HZP Individual Control Rod Bank Worths – Plant E Cycle 39

a,b,c

Table E-8: HZP Individual Control Rod Bank Worths – Plant E Cycle 40

a,b,c

Table E-9: HFP Critical Boron Concentration vs. Burnup – Plant E

a,b,c

Page Left Intentionally Blank

APPENDIX F   SUMMARY OF PLANT F

The following section contains the numerical benchmarking results for Plant F. HZP startup physics statistics, HFP depletion statistics, and radial power distributions (where applicable) are contained herein and listed below:

1. <u>HZP Startup Physics</u>

    a. ARO ITC – Table F-1

    b. ARO Critical Boron Concentration – Table F-2

    c. Total Rod Worths – Table F-3

    d. Individual Control Rod Worths – Table F-4 through Table F-9

2. <u>HFP Depletion</u>

    a. ARO Critical Boron Concentration Statistics – Table F-10

    b. Radial Power Distributions – Table F-11 through Table F-14

    c. Axial Power Distributions – Table F-15 through Table F-18

Table F-1: HZP ITC – Plant F

a,b,c

Table F-2: HZP ARO Critical Boron Concentration – Plant F

a,b,c

Table F-3: HZP Total Rod Worths – Plant F

a,b,c

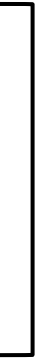**Table F-4: HZP Individual Control Rod Bank Worths – Plant F Cycle 25**
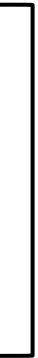
a,b,c

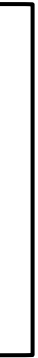**Table F-5: HZP Individual Control Rod Bank Worths – Plant F Cycle 26**
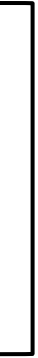
a,b,c

Table F-6: HZP Individual Control Rod Bank Worths – Plant F Cycle 27

a,b,c

Table F-7: HZP Individual Control Rod Bank Worths – Plant F Cycle 28

a,b,c

Table F-8: HZP Individual Control Rod Bank Worths – Plant F Cycle 29

a,b,c

Table F-9: HZP Individual Control Rod Bank Worths – Plant F Cycle 30
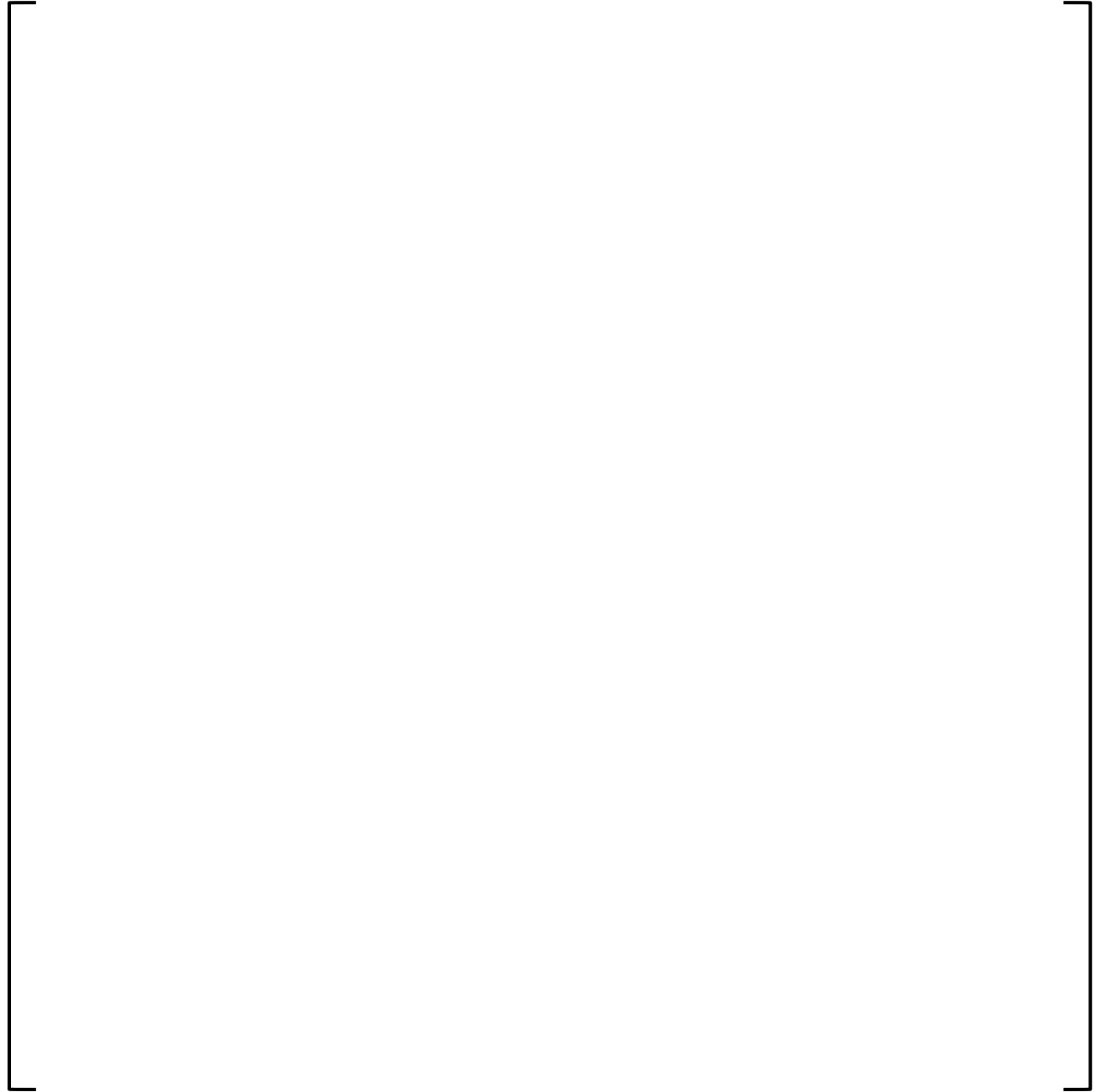
a,b,c

Table F-10: HFP Critical Boron Concentration vs. Burnup – Plant F
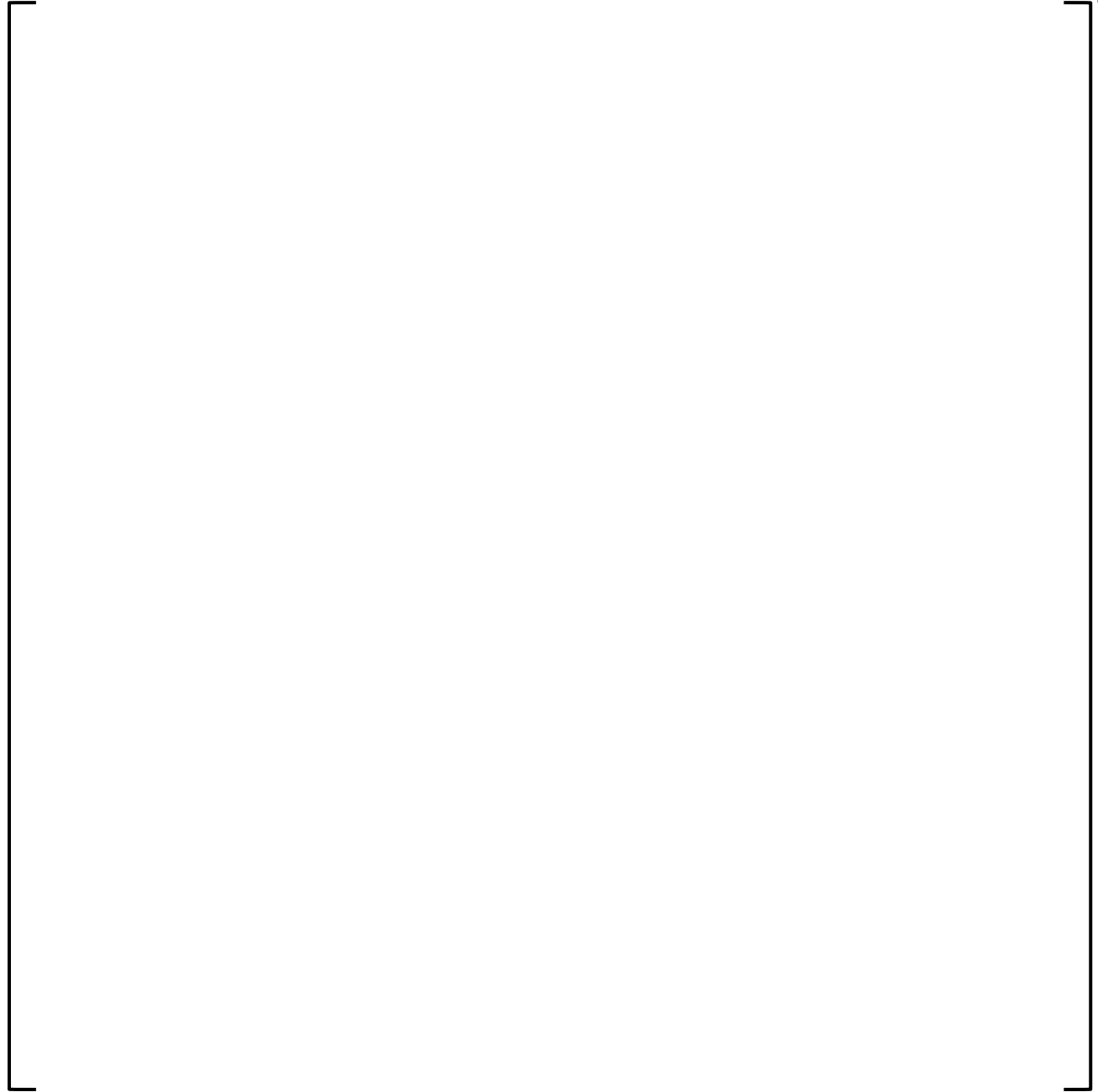
a,b,c

Table F-11: Assembly Average Radial Power Distribution – Plant F Cycle 30 BOC
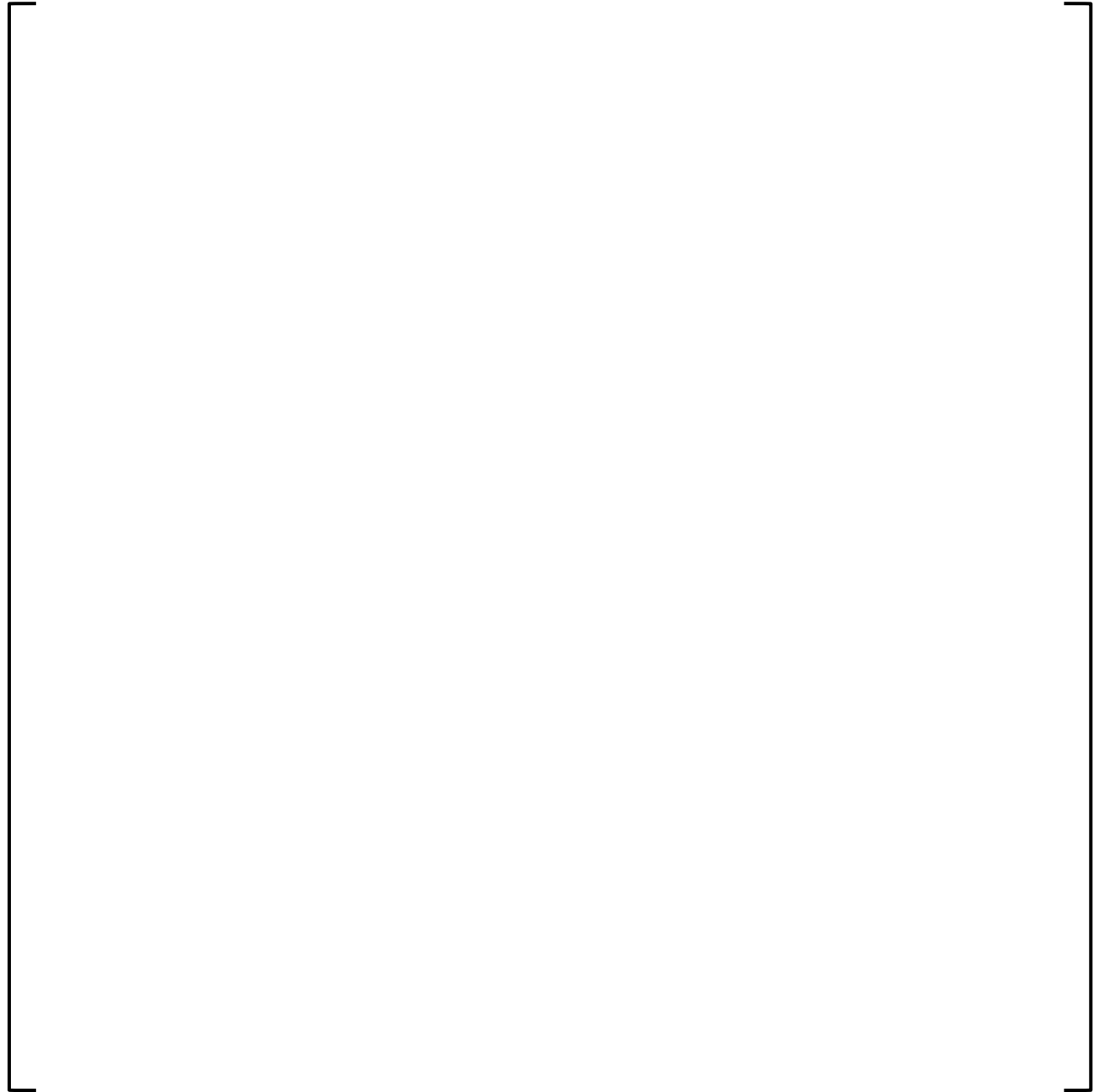
a,b,c

Table F-12: Assembly Average Radial Power Distribution – Plant F Cycle 30 MOC1
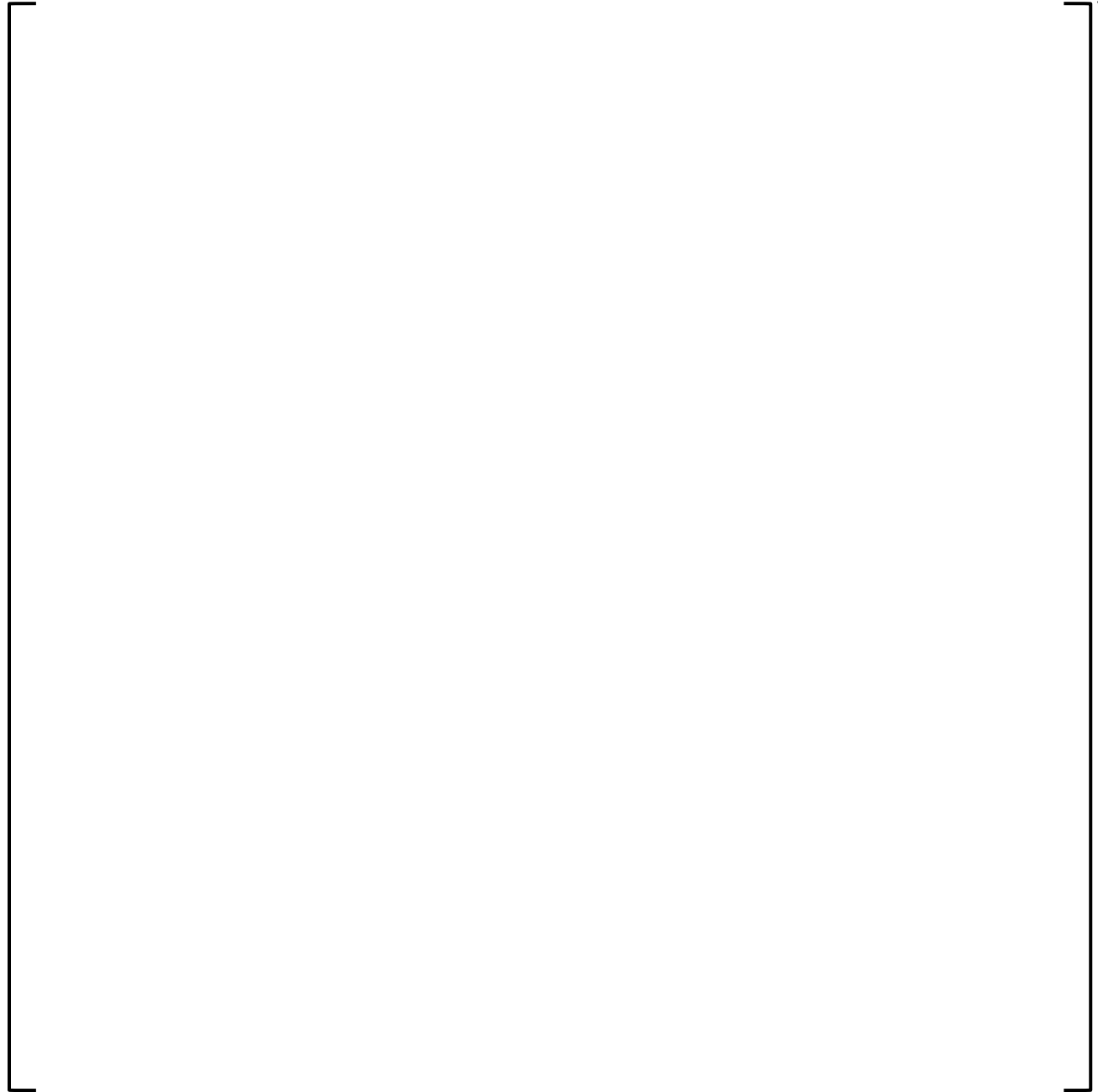
a,b,c

Table F-13: Assembly Average Radial Power Distribution – Plant F Cycle 30 MOC2

a,b,c

Table F-14: Assembly Average Radial Power Distribution – Plant F Cycle 30 EOC

a,b,c

Table F-15: Core Axial Power Distribution – Plant F Cycle 30 BOC

a,b,c

Table F-16: Core Axial Power Distribution – Plant F Cycle 30 MOC1

a,b,c

Table F-17: Core Axial Power Distribution – Plant F Cycle 30 MOC2

a,b,c

Table F-18: Core Axial Power Distribution – Plant F Cycle 30 EOC

a,b,c

Page Left Intentionally Blank

APPENDIX G   SUMMARY OF PLANT G

The following section contains the numerical benchmarking results for Plant G. HZP startup physics statistics, HFP depletion statistics, and radial power distributions (where applicable) are contained herein and listed below:

1. <u>HZP Startup Physics</u>

    a. ARO ITC – Table G-1

    b. ARO Critical Boron Concentration – Table G-2

    c. Total Rod Worths – Table G-3

    d. Individual Rod Worths – Table G-4 through Table G-10

2. <u>HFP Depletion</u>

    a. ARO Critical Boron Concentration Statistics – Table G-11

Table G-1: HZP ITC – Plant G

[

]a,b,c

Table G-2: HZP ARO Critical Boron Concentration – Plant G

[

]a,b,c

Table G-3: HZP Total Rod Worths – Plant G

[

]a,b,c

Table G-4: HZP Individual Control Rod Bank Worths – Plant G Cycle 1

a,b,c

Table G-5: HZP Individual Control Rod Bank Worths – Plant G Cycle 2

a,b,c

Table G-6: HZP Individual Control Rod Bank Worths – Plant G Cycle 3

a,b,c

Table G-7: HZP Individual Control Rod Bank Worths – Plant G Cycle 12

a,b,c

Table G-8: HZP Individual Control Rod Bank Worths – Plant G Cycle 13

a,b,c

Table G-9: HZP Individual Control Rod Bank Worths – Plant G Cycle 14

a,b,c

Table G-10: HZP Individual Control Rod Bank Worths – Plant G Cycle 15

a,b,c

Table G-11: HFP Critical Boron Concentration vs. Burnup – Plant G

a,b,c

APPENDIX H   SUMMARY OF PLANT H

The following section contains the numerical benchmarking results for Plant H. HZP startup physics statistics, HFP depletion statistics, and radial power distributions (where applicable) are contained herein and listed below:

1. <u>HZP Startup Physics</u>

    a. ARO ITC – Table H-1

    b. ARO Critical Boron Concentration – Table H-2

    c. Total Rod Worths – Table H-3

    d. Individual Rod Worths – Table H-4 through Table H-6

2. <u>HFP Depletion</u>

    a. ARO Critical Boron Concentration Statistics – Table H-7

    b. Radial Power Distributions – Table H-8 through Table H-11

    c. Axial Power Distributions – Table H-12 through Table H-15

Table H-1: HZP ITC – Plant H

a,b,c

Table H-2: HZP ARO Critical Boron Concentration – Plant H
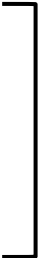
a,b,c

Table H-3: HZP Total Rod Worths – Plant H

a,b,c

Table H-4: HZP Individual Control Rod Bank Worths – Plant H Cycle 21

a,b,c

Table H-5: HZP Individual Control Rod Bank Worths – Plant H Cycle 22

a,b,c

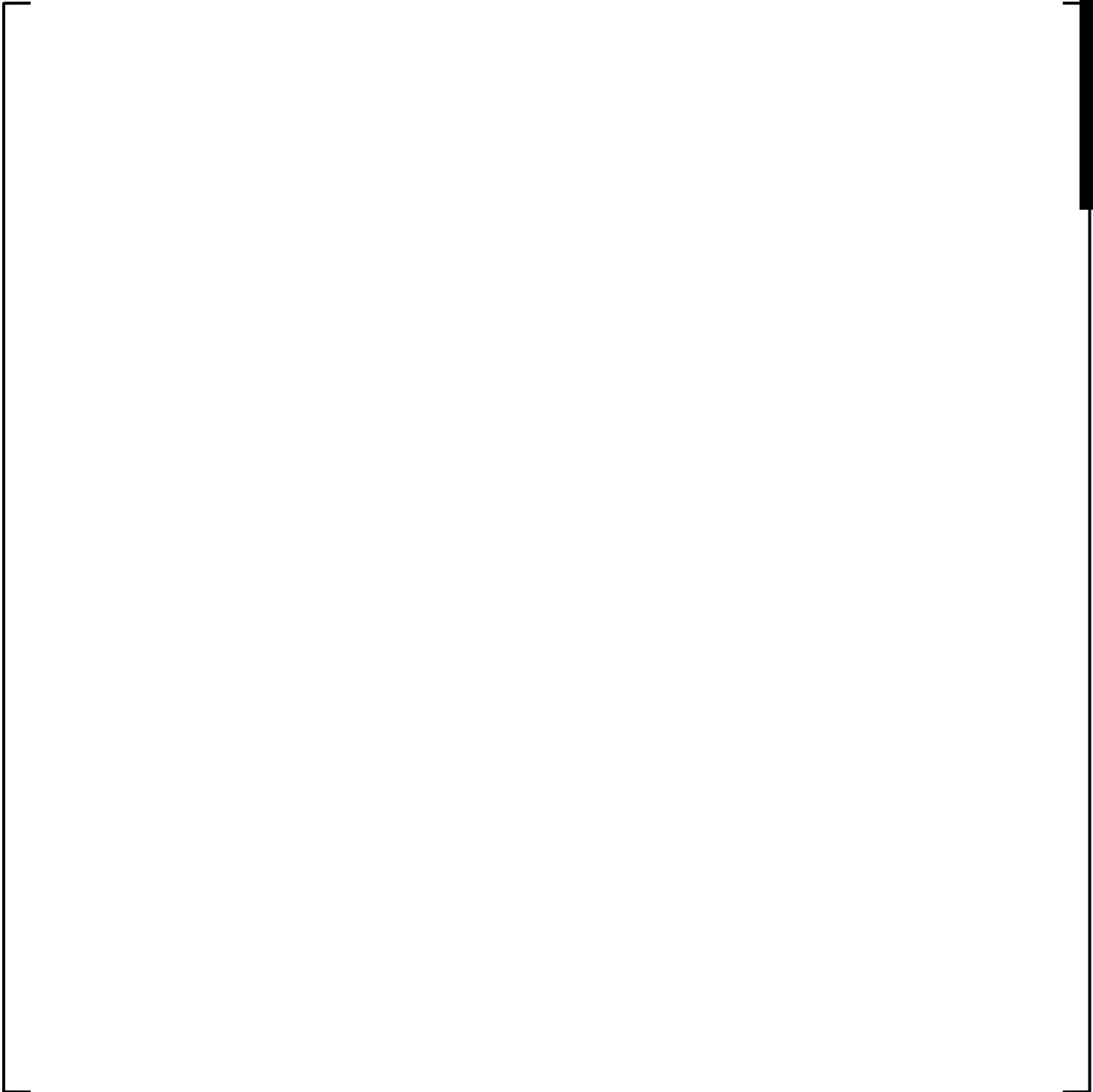**Table H-6: HZP Individual Control Rod Bank Worths – Plant H Cycle 23**

a,b,c

Table H-7: HFP Critical Boron Concentration vs. Burnup – Plant H

a,b,c

Table H-8: Assembly Average Radial Power Distribution – Plant H Cycle 22 BOC

Table H-9: Assembly Average Radial Power Distribution – Plant H Cycle 22 MOC1
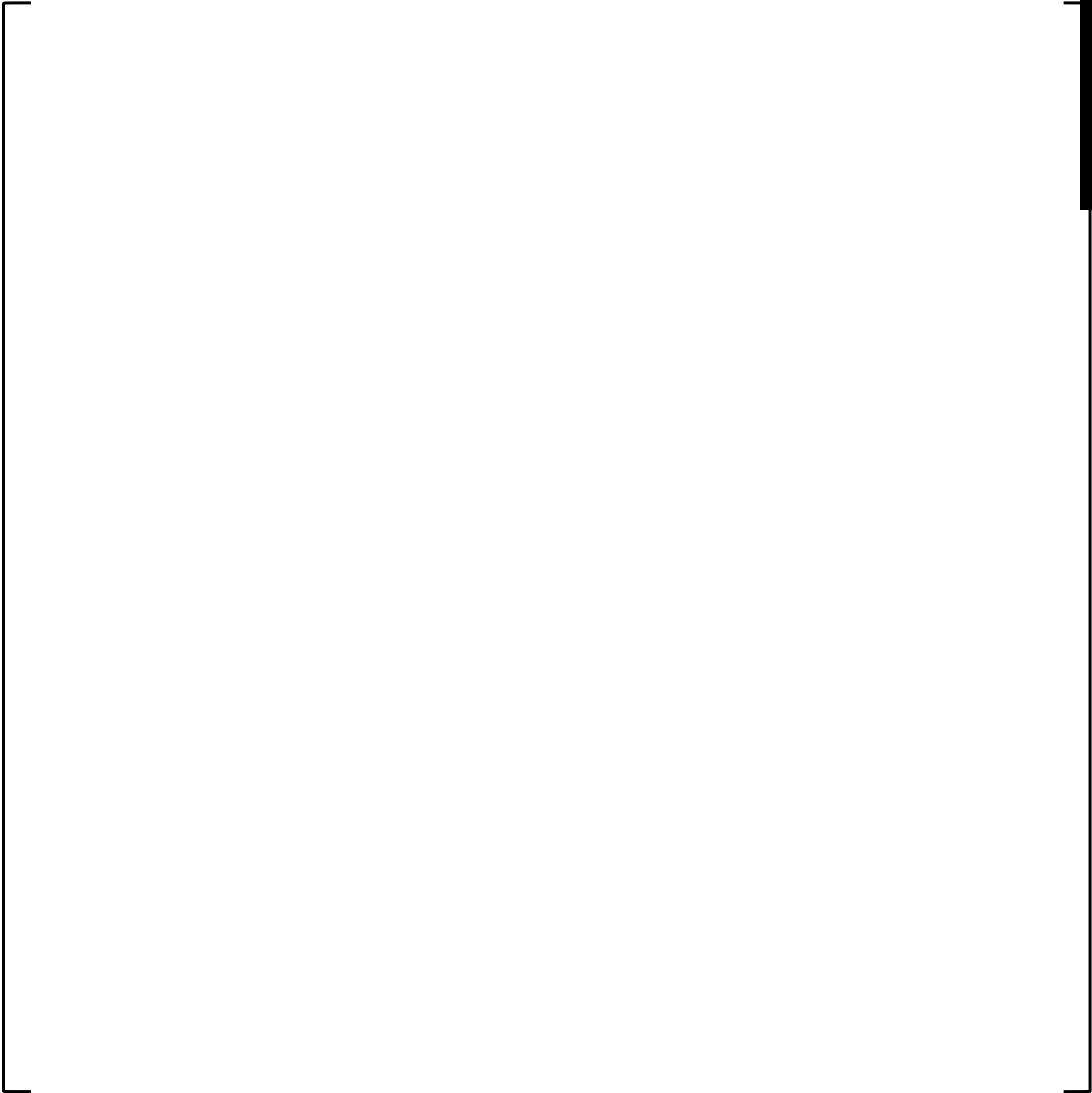
Table H-10: Assembly Average Radial Power Distribution – Plant H Cycle 22 MOC2
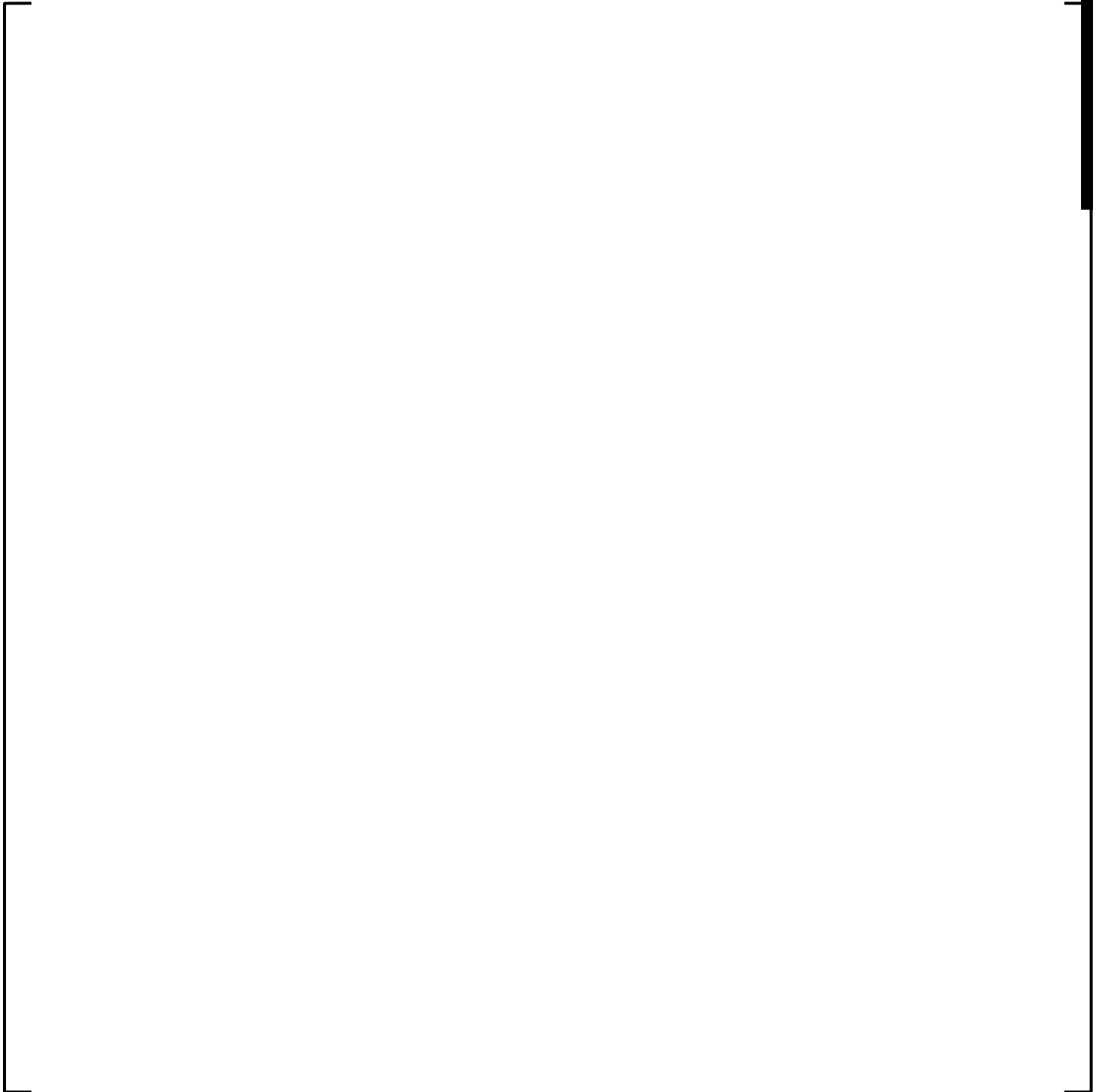
Table H-11: Assembly Average Radial Power Distribution – Plant H Cycle 22 EOC
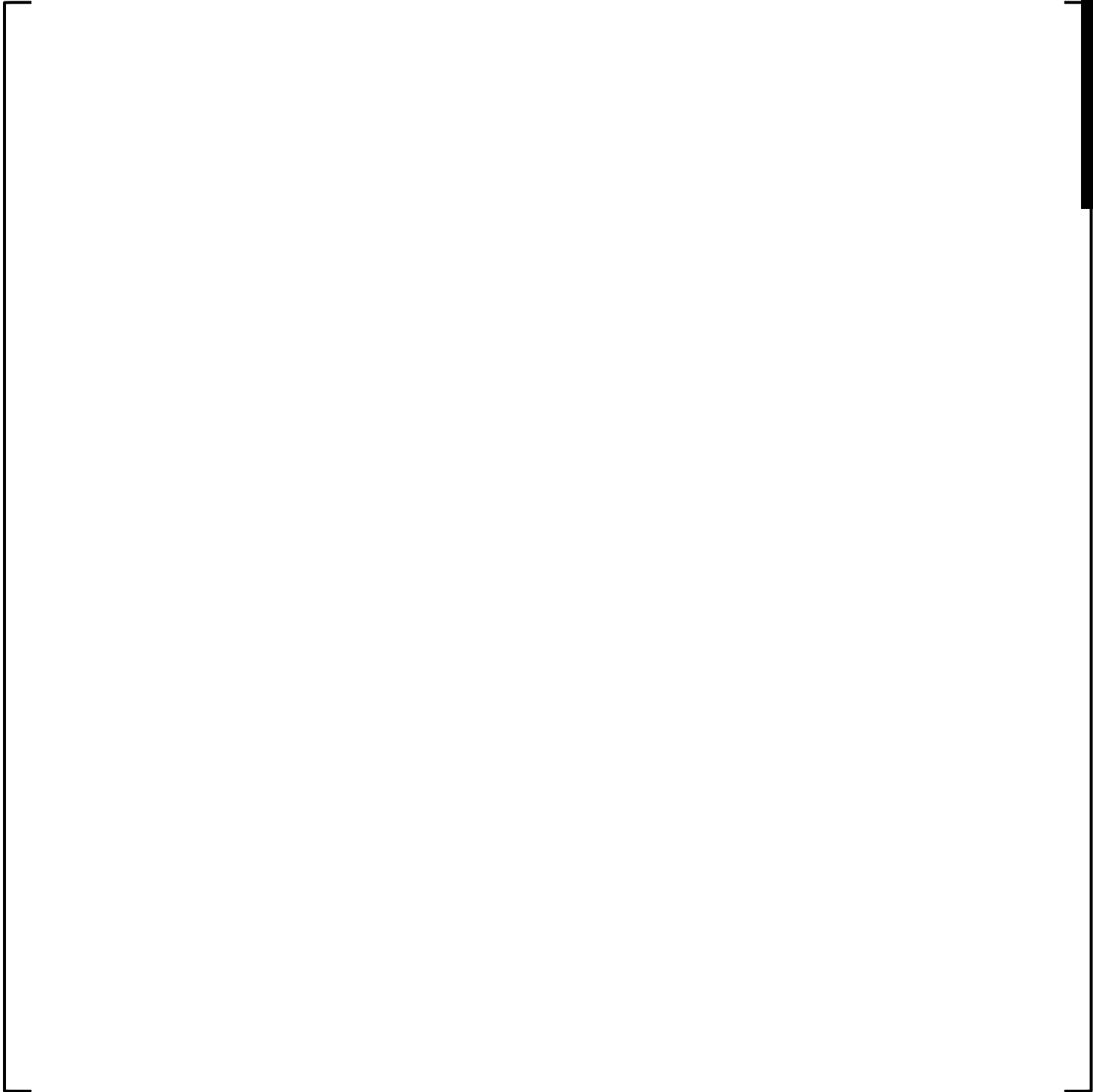
Table H-12: Core Axial Power Distribution – Plant H Cycle 22 BOC

a,b,c

Table H-13: Core Axial Power Distribution – Plant H Cycle 22 MOC1

a,b,c

Table H-14: Core Axial Power Distribution – Plant H Cycle 22 MOC2

a,b,c

Table H-15: Core Axial Power Distribution – Plant H Cycle 22 EOC

a,b,c

APPENDIX I   SUMMARY OF PLANT I

The following section contains the numerical benchmarking results for Plant I. HZP startup physics statistics, HFP depletion statistics, and radial power distributions (where applicable) are contained herein and listed below:

1. <u>HZP Startup Physics</u>

    a. ARO ITC – Table I-1

    b. ARO Critical Boron Concentrations – Table I-2

2. <u>HFP Depletion</u>

    a. ARO Critical Boron Concentration Statistics – Table I-3

Table I-1: HZP ITC – Plant I

a,b,c

Table I-2: HZP ARO Critical Boron Concentration – Plant I

a,b,c

Table I-3: HFP Critical Boron Concentration vs. Burnup – Plant I

a,b,c

Page Left Intentionally Blank

APPENDIX J   SUMMARY OF PLANT J

The following section contains the numerical benchmarking results for Plant J. HZP startup physics statistics, HFP depletion statistics, and radial power distributions (where applicable) are contained herein and listed below:

1. HZP Startup Physics

    a. ARO ITC – Table J-1

    b. ARO Critical Boron Concentration – Table J-2

    c. ARO CE Specific DPC – Table J-3

2. HFP Depletion

    a. Critical Boron Concentration Statistics – Table J-4

Table J-1: HZP ITC – Plant J

a,b,c

Table J-2: HZP ARO Critical Boron Concentration

a,b,c

Table J-3: HZP ARO CE Specific DPC – Plant J

a,b,c

Table J-4: HFP Critical Boron Concentration vs. Burnup – Plant J

a,b,c

Page Left Intentionally Blank

APPENDIX K   SUMMARY OF PLANT K

The following section contains the numerical benchmarking results for Plant K. HZP startup physics statistics, HFP depletion statistics, and radial power distributions (where applicable) are contained herein and listed below:

1. <u>HZP Startup Physics</u>

    a.   ARO ITC – Table K-1

    b.   ARO Critical Boron Concentration – Table K-2

Table K-1: HZP ITC – Plant K

a,b,c

Table K-2: HZP ARO Critical Boron Concentration – Plant K

a,b,c

APPENDIX L   SUMMARY OF PLANT L

The following section contains the numerical benchmarking results for Plant L. HZP startup physics statistics, HFP depletion statistics, and radial power distributions (where applicable) are contained herein and listed below:

1. <u>HZP Startup Physics</u>

    a. ARO ITC – Table L-1

    b. ARO Critical Boron Concentration – Table L-2

    c. Total Rod Worths – Table L-3

    d. Individual Rod Worths – Table L-4 through Table L-6

2. <u>HFP Depletion</u>

    a. ARO Critical Boron Concentration Statistics – Table L-7

Table L-1: HZP ITC – Plant L

[   ] a,b,c

Table L-2: HZP ARO Critical Boron Concentration – Plant L

[   ] a,b,c

Table L-3: HZP Total Rod Worths – Plant L

[   ] a,b,c

Table L-4: HZP Individual Control Rod Bank Worths – Plant L Cycle 22

a,b,c

Table L-5: HZP Individual Control Rod Bank Worths – Plant L Cycle 23

a,b,c

Table L-6: HZP Individual Control Rod Bank Worths – Plant L Cycle 24

a,b,c

Table L-7: HFP Critical Boron Concentration vs. Burnup – Plant L

[

]a,b,c

APPENDIX M   SUMMARY OF PLANT M

The following section contains the numerical benchmarking results for Plant M. HZP startup physics statistics, HFP depletion statistics, and radial power distributions (where applicable) are contained herein and listed below:

1. HZP Startup Physics

   a. ARO ITC – Table M-1

   b. ARO Critical Boron Concentration – Table M-2

   c. ARO CE Specific DPC - Table M-3

   d. Total Rod Worths – Table M-4

   e. Individual Rod Worths – Table M-5 through Table M-6

2. HFP Depletion

   a. ARO Critical Boron Concentration Statistics – Table M-7

Table M-1: HZP ITC – Plant M

a,b,c

Table M-2: HZP ARO Critical Boron Concentration – Plant M

a,b,c

Table M-3: HZP ARO CE Specific DPC – Plant M

a,b,c

Table M-4: HZP Total Rod Worths – Plant M

a,b,c

Table M-5: HZP Individual Control Rod Bank Worths – Plant M Cycle 13

a,b,c

Table M-6: HZP Individual Control Rod Bank Worths – Plant M Cycle 14

a,b,c

Table M-7: HFP Critical Boron Concentration vs. Burnup – Plant M

a,b,c

APPENDIX N   SUMMARY OF PLANT N

The following section contains the numerical benchmarking results for Plant N. HZP startup physics statistics, HFP depletion statistics, and radial power distributions (where applicable) are contained herein and listed below:

1. <u>HZP Startup Physics</u>

    a. ARO ITC – Table N-1

    b. ARO Critical Boron Concentration – Table N-2

    c. ARO CE Specific DPC – Table N-3

    d. Total Rod Worths – Table N-4

    e. Individual Rod Worths – Table N-5

2. <u>HFP Depletion</u>

    a. ARO Critical Boron Concentration Statistics – Table N-6

Table N-1: HZP ITC – Plant N

a,b,c

Table N-2: HZP ARO Critical Boron Concentration – Plant N

a,b,c

Table N-3: HZP ARO CE Specific DPC – Plant N

a,b,c

Table N-4: HZP Total Rod Worths – Plant N

a,b,c

Table N-5: HZP Individual Control Rod Bank Worths – Plant N Cycle 1

a,b,c

Table N-6: HFP Critical Boron Concentration vs. Burnup – Plant N

a,b,c